Peptide-functionalized Biomaterials for Hemostasis and Cancer Imaging

Leslie Wan-Gee Chan

A dissertation

submitted in partial fulfillment of the

requirements for the degree of

Doctor of Philosophy

University of Washington

2015

Reading Committee:

Suzie Hwang Pun, Chair

Patrick Stayton

Nathan James White

Program Authorized to Offer Degree:

Bioengineering

University of Washington

Abstract

Peptide-functionalized Biomaterials for Hemostasis and Cancer Imaging

Leslie Wan-Gee Chan

Chair of the Supervisory Committee:
Professor Suzie Hwang Pun
Department of Bioengineering

Molecular recognition drives all biological processes and can be leveraged to engineer a broad range of biomaterials for detection and treatment of altered states in the body. Part I of this dissertation focuses on the use of peptide-fluorophore conjugates to bind and label cell surface targets that are upregulated in dysplastic (pre-cancerous) esophageal tissue for endoscopic imaging. Initially, fluorescent nanoparticles functionalized with anti-epidermal growth factor receptor (EGFR) antibodies were synthesized and evaluated for their ability to label dysplasia in human biopsies. However, EGFR was found to be a non-ideal molecular target due to high expression in non-dysplastic tissues. Subsequently, phage display was used to identify peptides that would bind to molecular targets specific to dysplastic cells. A family of peptides was found and is believed to bind with low affinity to glycan targets on dysplastic cells. Part II focuses on development of peptide-functionalized polymers for intravenous administration to fortify blood clots and resolve bleeding after traumatic injury. Polymer hemostats (PolySTATs) with multivalent display of fibrin-binding peptides were engineered to strengthen blood clots by cross-linking fibrin. PolySTAT integration in fibrin networks *in vitro* resulted in stiffer clots that were more resistant to enzymatic breakdown. These results translated *in vivo*, where PolySTAT injection into animal injury models reduced blood loss and improved survival rate. Further characterization of PolySTAT demonstrates similar functional outputs to current clinical hemostatic agents (e.g. recombinant factor VIIa and tranexamic acid) and its potential use in resolving bleeding in congenital bleeding disorders such as hemophilia A.

TABLE OF CONTENTS

Page

LIST OF FIGURES

Figure Number Page

Part I

Part II

ACKNOWLEDGEMENTS

I would like to thank Suzie for her mentorship these past 5 years. She has given me numerous opportunities to grow as an independent researcher and has been such a positive role model, both professionally and personally. I would also like to thank our collaborators acknowledged below, whose expertise was integral to the completion of the work discussed here. An especial thanks to Xu Wang, who took the opportunity to make each animal study into an anatomy and physiology lesson, Greg Martin at the UW Keck Microscopy Facility, who taught me the art of confocal imaging, and Hua Wei, who taught me RAFT polymerization. Last (but certainly not least), thank you to my support system: my parents, my sister, my housemate and writing buddy (Jon Cheng), my boardgaming and karaoke buddies (Joe Phan, Austin Day, and Thomas Long), and my fellow labmates and commiserators of failed experiments (Julie Shi, Maryelise Cieslewicz, and Christine Wang).

Special thanks to our collaborators:

Dr. William M. Grady
Dr. Joo Ha Hwang
Pablo D. Iglesia
Esther B. Lim
Dr. Lih Y. Lin
Meghan Lyle
Dr. Carol H. Miao
Dr. Lilo D. Pozzo
Dr. Melissa P. Upton
Dr. Yak-Nam Wang
Dr. Xu Wang
Dr. Nathan J. White

DEDICATION

This is dedicated to all my past teachers, who, very early on, laid the foundation that enabled me to pursue a graduate education. For my mom and very first teacher, Ruby, who bravely took it upon herself to teach a blank slate the alphabet. For my dad, Hunter, who came to my rescue during my first and subsequent encounters with physics and who always emphasized the importance of a good education. For my middle school science teacher, Mr. David Pauli, who believed that I could excel in science. For my high school biology teachers, Dr. Kim Nichols and Dr. Susan Kramer, who decided to forgo more glamorous careers at the CDC and in medicine for teaching. For my organic chemistry I professor at Georgia Tech, who showed me the beautiful logic behind pushing electrons. I owe my love of learning to these individuals who were able to make sense of things that would have otherwise seemed very abstract.

PART I

MOLECULAR IMAGING OF HIGH GRADE DYSPLASIA IN THE ESOPHAGUS

EXECUTIVE SUMMARY

High-grade dysplasia (HGD) is a validated predictive marker for esophageal adenocarcinoma (EAC). However, dysplastic epithelium is difficult to visualize using conventional white light endoscopy due to its flat architecture and multifocal distribution and is therefore frequently missed during biopsy procedures. Molecular imaging of biochemical alterations characteristic to HGD is a promising approach to improving the sensitivity and specificity of endoscopic imaging. Recent work has identified potential HGD targeting ligands including a peptide isolated using *in vitro* phage display and wheat germ agglutinin (WGA), a lectin that binds to normal tissues around dysplastic lesions. In this work, the following specific aims are proposed to identify novel HGD targeting ligands with proposed methods to optimize their binding affinity:

Specific Aims

Specific Aim 1. Evaluate epidermal growth factor receptor (EGFR) as a potential molecular target for imaging HGD. Concurrently, synthesize EGFR-targeting fluorescent nanoparticles for labeling EGFR *ex vivo* in biopsy specimen. EGFR-targeting fluorescent nanoparticles were synthesized and specifically stained EGFR+ cell lines over EGFR- cell lines [Chapter 2]. Furthermore, nanoparticle staining of EGFR in human esophageal tissues coincided well with standard immunohistochemistry staining for EGFR. However, EGFR was shown to be expressed to a significant degree in non-dysplastic BE tissues and was not optimal for specific labeling of HGD. This prompted the search for novel HGD binders.

Aim 1 Chapters.

Antibody-targeted fluorescent nanoparticles for imaging epidermal growth factor receptor (EGFR) *in vitro* and in *ex vivo* human esophageal specimen. [Chapter 2]

Publications.

Chan, L. W., Wang, Y. N., Lin, L. Y., Upton, M. P., Hwang, J. H., & Pun, S. H. (2013). Synthesis and Characterization of Anti-EGFR Fluorescent Nanoparticles for Optical Molecular Imaging. *Bioconjug Chem, 24*(2), 167-175. doi: 10.1021/bc300355y

Specific Aim 2. Identify and characterize novel targeting ligands preferentially binding dysplastic over non-dysplastic Barrett's esophagus (BE). *In vitro* phage display was completed to identify peptide targeting ligands [Chapter 3]. A subtractive whole cell approach was used to eliminate peptides binding normal esophageal keratinocytes and non-dysplastic BE, and subsequent selection against dysplastic cell lines was completed to select for peptides binding dysplasia. A family of peptides and a lone peptide sequence were isolated. Phage expressing these peptides bind specifically to dysplastic cell lines. More specifically, homology of these peptide sequences to sugar-processing enzymes suggests they bind glycan targets. The peptide showing the greatest frequency in isolated phage, B22, was synthesized and fluorescently labeled for binding studies. Kd curves show B22 bind to dysplastic cells with very low affinity.

Aim 2 Chapters.

Identification of novel peptides for endoscopic imaging of highgrade dysplasia in Barrett's esophagus. [Chapter 3]

Chapter 1

HIGH-GRADE DYSPLASIA IN THE ESOPHAGUS: ETIOLOGY AND METHODS OF IMAGING AND DETECTION

1.1 Introduction

The 2 main types of cancers in the esophagus are esophageal adenocarcinoma (EAC) and squamous cell carcinoma (SCC). Currently, SCC is most prevalent in Africa and East Asia and is associated with poor diet, smoking, and low socioeconomic status. Before the 1960s, SCC made up approximately 90% cases of esophageal cancer in the U.S. and within the past 40 years EAC has significantly increased to 80% of esophageal cancer cases thus becoming the cancer with the fastest growing incidence rate in the U.S. and other developed western nations.[3] EAC is most commonly found in white Caucasian males above the age of 60.

EAC occurs in the distal esophagus at the gastroesophageal junction. It is believed that EAC is the endpoint to a series of changes to normal tissue known as the metaplasia-dysplasia-adenocarcinoma sequence.[4] Metaplasia is a condition in which one tissue type is replaced by another. Metaplasia of the esophagus is called Barrett's esophagus (BE) and is evidenced by the normally flat squamous architecture of esophageal lining becoming more like columnar intestinal epithelium (**Figure 1.1**). Gastroesophageal reflux disease (GERD) is attributed to BE. Over time, BE can progress to BE with low-grade dysplasia (LGD) or high-grade dysplasia (HGD) of which the latter has been shown to be an effective predictive marker for patients at high risk for developing esophageal adenocarcinoma [5,6]. Approximately 59% of patients with BE with HGD progress to EAC within 5 years of diagnosis. [5,7-9] Furthermore, studies indicate up to 50% of patients undergoing esophagectomies due to HGD diagnosis have coexisting cancer that was not

detected endoscopically.[10,11] Therefore, HGD detection is necessary to identify patients who require preventative measures such as more frequent endoscopic surveillance, esophageal mucosal resectioning, ablative therapies, or esophagectomies.

Chapter 1 gives an overview of the etiology of EAC with subsequent analysis of current and emerging methods for imaging and detecting HGD to provide contextual background for the proposed work of this thesis.

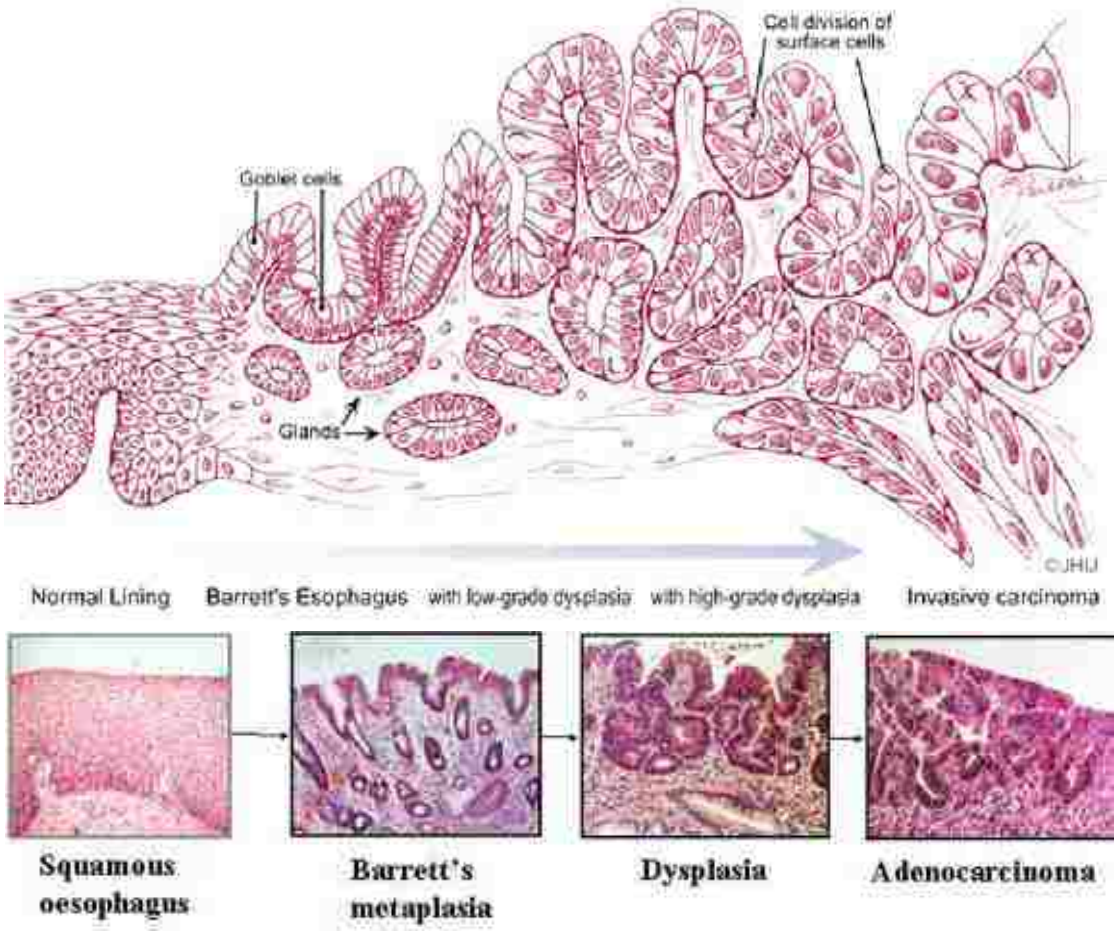

Figure 1.1 Histological progression of the metaplasia-dysplasia-adenocarcinoma sequence. Adapted from [11,12].

1.2 Molecular progression of the metaplasia-dysplasia-adenocarcinoma sequence

Current hypotheses concerning the progression of the metaplasia-dysplasia-adenocarcinoma sequence involves the process of epithelium regeneration after damage from esophageal reflux and persistent esophagitis. Esophagitis is chronic inflammation in the esophagus and is attributed to failure of local defenses such as mucus, buffering ability of alkaline saliva, and peristaltic clearance to counteract the refluxed acid. Prolonged reflux results in damage to the superficial compartment of the epithelium. It is hypothesized that an early adaptive response to continual cell loss is an increase height and length of the proliferative zone due to local stimulation of epidermal growth factor (EGF). Increased zone length causes folding of the basal epithelium into papillae (**Figure 1.2**). Damage and folding causes stem cells in the basal epithelium to become exposed to refluxed or ingested mutagens. In response to acid reflux, stem cells differentiate into intestinal-type cells thus resulting in Barrett's esophagus. Cells in Barrett's tissue have cytological abnormalities such as aneuploidy and gene amplification. Clonal expansion of cells with changes in

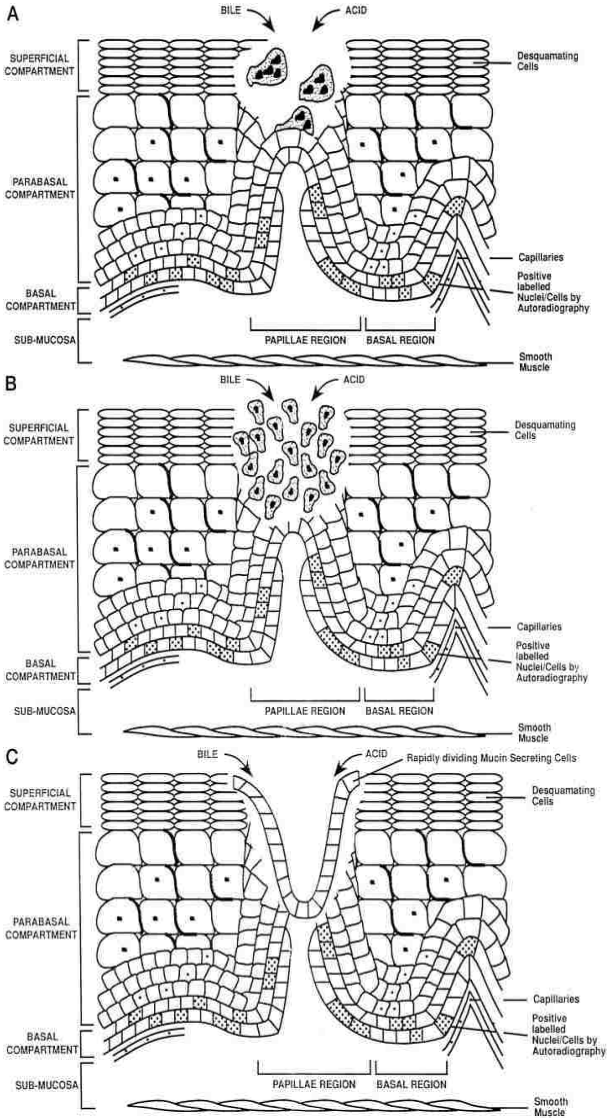

Figure 1.2 Schematic representation of (A) damage to the differentiated cells in the superficial and parabasal compartments (B) damage to the deeper basal compartment housing squamous epithelial stem cell and (C) generation of clones with a mucin-secreting lineage resistant to acid/bile. Adapted from [5].

growth factor and receptor expression and p53 mutations leads to the development of esophageal adenocarcinoma.[4]

1.2.1 Environmental factors

Predisposition to EAC is most likely multifactorial. However, the sharp rise in the incidence of EAC suggests that environmental factors play a large role in susceptibility to EAC. It is difficult to pinpoint specific environmental factors. However, the increased risk of EAC associated with GERD and BE indicates that factors contributing to the latter two conditions are relevant epidemiologically. Esophageal reflux has become one of the most common conditions in Western nations and up to 10% of cases will progress to BE.[4] Factors contributing to persistent esophagitis include dietary components, obesity, non-steroidal anti-inflammatory drugs, nitrosamines, and eradication of *H. pylori*.[4,12,13] Factors that are under debate include alcohol consumption and smoking.

1.2.2 Genetic factors

It is unlikely that genetic factors alone have influenced the dramatic and abrupt 350% increase in incidence of EAC in the past 3 decades.[14,15] However, a recent study showed that up to 13% of EAC cases may have a genetic predisposition to EAC due to germline mutations in the *MSR1, ASCC1, CTHRC1* genes affecting macrophage function and inflammatory pathways.[14] In addition, single nucleotide polymorphisms (SNPs) in genes encoding for matrix metalloproteinases, insulin-like-growth factor (IGF), epidermal growth factor (EGF), and vascular endothelial growth factor (VEGF) are other possible are also possibly associated with increased risk for EAC.[16-19]

1.2.3 Contribution of microbiome in the distal esophagus

Bacteria-host interactions can be classified as mutualism, commensalism, or parasitism. Recently, there have been a number of studies looking at the microbiome in the esophagus under normal and diseased states due to growing interest in the role of bacteria in the pathogenesis of esophageal adenocarcinoma. Chronic inflammation has been linked to the development of cancer, and pathogenic bacteria have been shown to induce epithelial cell secretion of pro-inflammatory cytokines.[20] In addition, some bacteria have the ability to reduce nitrates to nitrite, which under acidic conditions can result in the production of carcinogens and mutagens such as N-nitroso compounds and nitrous oxide.[21] The link between *H. pylori* infection and significantly increased risk of gastric cancer[22,23] sets precedence for causal relationships between specific bacterial species and oncogenic inflammation. This has in some part prompted investigations on the connection between bacteria in the esophagus and pathologies such as esophagitis, Barrett's esophagus, and esophageal adenocarcinoma.

Relative to the microbiome in the mouth, stomach, and intestine, bacterial populations in the esophagus have been studied minutely. In 1998 and 2002, two studies using culture-based methods to identify bacterial species in esophageal luminal washes were published.[24,25] These studies showed very little bacterial diversity and suggested the esophagus housed very few species of bacteria. However, the lack of captured bacterial diversity can be attributed to culture conditions that are not amenable to all bacterial species and the inability of luminal washes to dissociate bacteria intimately associated with the epithelium.

Figure 1.3 Gram-Twort stained normal esophageal tissue showing Gram-negative bacillus tightly associated with squamous epithelial cells.[2]

Subsequent studies utilizing broad-range 16S rDNA PCR, a method for sequencing ribosomal DNA from bacteria, to identify bacterial species in biopsy specimen demonstrated much greater diversity than previously

observed. In 2004, Pei et al. published sequencing results from biopsies of four human adults in the *Proceedings of the National Academy of Sciences.* Their studies showed that the normal distal esophagus microbiome consists of a complex but conserved set of bacterial species representing at least six phyla *Firmicutes, Bacteroides, Actinobacteria, Proteobacteria, Fusobacteria, and TM7*, 41 genus-level taxonomic units, and 96 species-level operational taxonomic units (SLOTU).[2] In addition, stained sections of esophageal tissues showed bacteria in tight association with the surface of epithelial cells (**Figure 1.3**). Pei et al. attributed this tight association to their ability to demonstrate a diverse microbiome using esophageal tissues and the existence of residential bacteria in the distal esophagus.

In a follow-up paper published in 2005, the same group attempted to study differences in bacteria in reflux esophagitis and Barrett's esophagus but did not show any conclusive differences between bacteria biota in normal tissue and tissue from GERD-related conditions.[26] The authors attributed this to low sample size. A study from the previous year, using gram stain scores showed a weak correlation between increasing bacterial scores and the severity of GERD (from esophagitis to BE to BE with increasing degrees of dysplasia).[27] In 2007, a more extensive study was completed by a third party identifying bacteria in not only tissue but tissue aspirates from patients with BE using culturing methods, 16S rDNA PCR, and fluorescence *in situ* hybridization to visualize bacterial colonies in tissue sections. Tissues and aspirates from seven patients with and without BE were analyzed. BE tissues had approximately 2-fold greater number of represented genera and species compared to control tissues. Greater species diversity was also observed in aspirate samples from BE patients. In addition, high levels of pathogenic nitrate-reducing *Campylobacter* species were found in 4 of 7 BE patients with none found in control patients. *In situ* hybridization studies showed microcolonization of bacteria on the epithelium. These authors proposed the possibility that microcolonies of nitrate-reducing bacteria such

as *Campylobacter* would produce nitrite-derivatives which in high local concentrations result in a greater degree of tissue damage in BE patients.

Perhaps one of the most convincing studies to date is from Yang et al. with a focus on the separation of esophageal bacteria into Type I and Type II classifications using clustering analysis, UniFrac significance tests, and double principal coordinate analysis.[1] Bacteria were identified in 34 biopsy specimen (12 normal, 12 esophagitis, 10 BE). Clustering analysis revealed two distinct clusters. 11 of 12 normal specimen fell into cluster 1 (Type I microbiome), and 13 of 22 pathologic specimen fell into cluster 2 (Type II microbiome). Further analysis was completed using UniFrac, a statistical method testing the hypothesis that the phylogenetic diversity of a single environment is greater than the phylogenetic diversity of randomly distributed sequences from various environments. UniFrac tests indicated that intracommunity diversity of Type I and Type II microbiome was significantly less ($p<0.001$) than that of the two microbiomes combined, meaning that the clustering of bacteria into two separate types is not due to random chance.

Furthermore, principle component analysis (PCA) was completed by establishing a first principle coordinate (PC1) which separated normal samples from pathologic samples to the highest degree. PC1 was shown to significantly correlate with decreasing abundance of *Streptococcus* ($r = -0.99$, $P = 4.5 \times 10^{-15}$), a spherical gram-positive bacteria belonging to the phyla *Firmicutes*. A 95% normal reference range (NRR) calculated using the relative abundance of *Streptococcus* was able to successfully identify the 9 normal cases that originally clustered to define the Type I microbiome and the 13 pathologic cases that originally clustered to define the Type II microbiome. Type I samples had an average of 78.8% *Streptococcus* (range, 60.5-97.0%), and Type II had an average of 30.0% *Streptococcus* (range, 8.0-46.5%). Further analysis also showed a strong correlation between PC1 and the relative abundance of anaerobic/microaerophilic bacteria ($r = 0.98$, $P = 2.3$

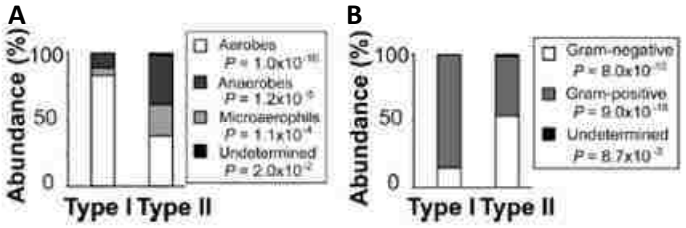

Figure 1.4 Relative abundance of bacteria groups as defined by (A) oxygen requirement and (B) chemical makeup of cell walls in Type I and Type II microbiomes.[1]

x 10^{-14}), between PC1 and the relative abundance of gram-negative bacteria (r = 0.97, P = 5.8 x 10^{-14}), between the relative abundance of *Streptococcus* and anaerobic/microaerophilic bacteria (r = -0.98, P = 3.1 x 10^{-14}), and between the relative abundance of *Streptococcus* and gram-negative bacteria (r = -0.96, P = 1.8 x 10^{-13}). These results suggest a strong inverse relationship between *Streptococcus* and anaerobic/microaerophiles/gram-negative bacteria (**Figure 1.4**). As observed in previous studies, the disease-associated microbiome was significantly more diverse than the non-diseased microbiome. Genera representing greater than 1% abundance in Type II samples include *Veillonella, Prevotella, Haemophilus, Neisseria, Rothia, Granulicatella*, *Campylobacter*, *Porphyromonas*, *Fusobacterium*, and *Actinomyces*. The recurrence of *Campylobacter* in pathologic samples in this study as well as in the 2007 study by MacFarlane et al. is noteworthy.

The global changes in microbiome observed in the last paper have many implications but does not necessarily confirm a *causal relationship* between bacteria and the pathogenesis of esophageal adenocarcinoma. The shift to more anaerobes/microaerophiles/gram-negative bacteria could be a *result* of the change in the environment of the distal esophagus from chronic inflammation. From the opposite standpoint, the increased presence of gram-negative bacteria in the inflammation-associated Type II microbiome (i.e. esophagitis and BE) is interesting because the outer cell walls of these bacteria contain lipopolysaccharide (LPS). LPS is an endotoxin that promotes the secretion of proinflammatory cytokines in monocytes and epithelial cells

through activation of toll-like receptor 4 (TLR 4) and the NF-κB pathway.[28] Thus, this is a proposed mechanism through which the Type II microbiome might be responsible for chronic inflammation.[28] Another proposed mechanism is LPS relaxation of the lower esophageal sphincter, which would prolong inflammation through increased gastric reflux. LPS-dose dependent relaxation of the lower esophageal sphincter has been demonstrated before in mouse studies. Finally, LPS has been shown to delay the emptying of gastric contents thereby increasing intragastric pressures which contributes to gastric reflux.

There has not been any conclusive evidence that the microbiome in the distal esophagus is responsible for the pathogenesis of esophageal adenocarcinoma. However, it is quite possible that bacteria contribute to the chronic inflammation that leads to oncogenesis given that they have been implicated in stomach cancer and in oncogenic colitis mouse models.

1.3 Conventional methods of HGD imaging and detection

1.3.1 Imaging methods

Dysplastic tissues have very subtle changes that are not easily visualized using conventional white light endoscopy (WLE). Therefore, more rigorous biopsy procedures such as the four-quadrant biopsy have been used to increase the sensitivity of WLE surveillance. However, even with the most rigorous biopsy procedures, less than 1% of the esophageal mucosa is surveyed, and up to one third of cases with HGD and early cancer are missed.[29,30] Therefore, alternative methods such as chromoendoscopy, narrow band imaging (NBI), confocal laser endomicroscopy (CLE), and autofluorescence imaging (AFI) are currently being used in attempt to facilitate HGD-targeted biopsies.

Chromoendoscopy involves two steps: 1) the removal of mucus by rinsing with water or mucolytics (i.e. N-Acetylcysteine) and 2) the topical application of dyes for visualization of the mucosal surface. The more commonly used

classes of dyes are contrast and absorptive.[29,31] Contrast dyes such as indigo carmine (IC) accumulate in mucosal crevices thus delineating contours in the mucosal topology. Irregular and/or distorted topology has been previously correlated to HGD as opposed to circular, ridged, and villous topology.[32] Differential absorption of absorptive dyes such as methylene blue (MB), Lugol's iodine (LI), and crystal violet in cellular structures can be used to identify certain types of mucosa. MB is the most investigated and controversial absorptive dye. It is readily absorbed by goblet cells which are found in BE but disappear with the progression of dysplasia.[31] Thus, it generates negative contrast for HGD detection. However, there have been many conflicting reports on the sensitivity of MB most likely due to interobserver variability and differences in staining protocol.[31] Main points of contention are that dysplasia and cancer have been found in tissues stained positive with MB[33,34] and that both normal tissue and dysplastic tissues have negative MB staining. LI stains glycogen in squamous epithelial cells brown to distinguish between esophageal squamous epithelium and columnar epithelium of the stomach. BE and epithelium damaged by esophagitis do not stain well and thus LI is able to show the state of tissues at the gastroesophageal junction. Crystal violet is more commonly used in the colon but has been shown to enhance MB staining of BE. However, its staining mechanism is not clear.[31] Reactive dyes are the third class of dyes which are least commonly used. These include Congo red and phenol, dyes that change color depending on pH.

Narrow band imaging (NBI) uses narrow band filters to image blue light at 415 nm and green light at 540 nm. Hemoglobin has peak absorption at both of these wavelengths and thus NBI is able to highlight tissue vasculature. Blue light provides high contrast imaging of superficial capillaries while green light penetrates deeper for high contrast imaging of subepithelial vessels and tissue surfaces (**Figure 1.5a**).[29] NBI has been used to correlate ridged and/or villous and circular topology with BE and irregular

and/or distorted topology with HGD (**Figure 1.5b-d**).[32] Switching from WLE to NBI requires the simple negation of the red wavelength using a filter, and joint WLE-NBI systems are currently available. NBI is promising with a sensitivity and specificity of 96% and 94%, respectively.[35]

Confocal laser endomicroscopy (CLE) permits real-time histological analysis of esophageal tissues and (sub)epithelial vasculatures by intravenous injection and excitation of a fluorescent marker (e.g. fluorescein sodium) at 480 nm with image

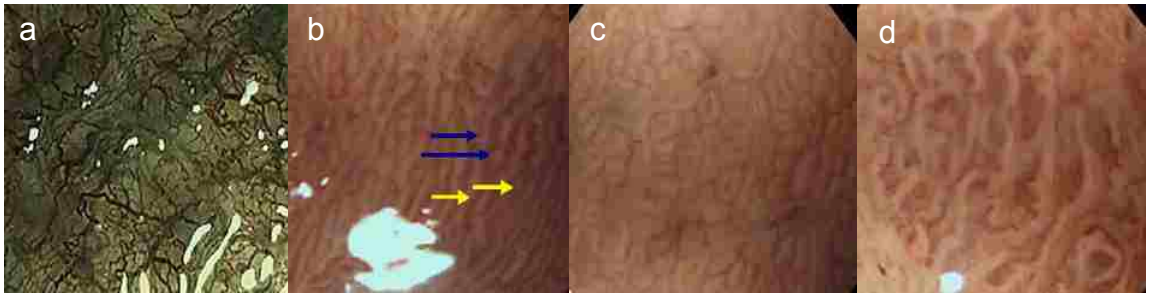

Figure 1.5 Images of the esophageal epithelium produced by narrow-band imaging showing (a) superficial capillaries and subepithelial blood vessels (b) ridge (blue arrows) and villous (yellow arrows) patterns (d) circular pattern and (d) distorted and irregular patterns in HGD. Adapted from [2,3].

acquisition at up to 1000-fold magnification (**Figure 1.6**).[29] Endoscopes with embedded CLE (eCLE) are available as are probe-based CLE (pCLE) in which an endomicroscopy probe is inserted into the working channel of a standard endoscope. Signs of dysplasia include irregular epithelial topology, fusion of glands, focal accumulation of dark cells with light lamina propria, irregular vascular patterns, and disruption of glandular patterns.[29] HGD was detected with a sensitivity and specificity of 92.9% and 98.4%, respectively, using eCLE in a study by Kiesslich et al.[36] Another study demonstrated that use of pCLE or WLE or NBI compared to use of WLE or NBI increased sensitivity by 1.7-fold with a slight decrease in specificity.[37] CLE is thus also a new, promising technique for imaging HGD.

Tissues autofluoresce when exposed to short wavelengths of light due to the presence of endogenous fluorophores such as porphyrin, collagen,

NAD(P)H, and aromatic amino acids. The composition of fluorophores changes in diseased states. Tissues with HGD are characterized by low collagen fluorescence and high NAD(P)H fluorescence equating to relatively lower green fluorescence intensities and higher red fluorescence intensities. Autofluorescence imaging (AFI) uses relative autofluorescence to identify tissue types. A 2006 study showed 91% sensitivity and 43% specificity when using AFI and four-quadrant biopsy to identify HGD. AFI results in a large number of false positives due to loss of autofluorescence in inflamed tissues.[29]

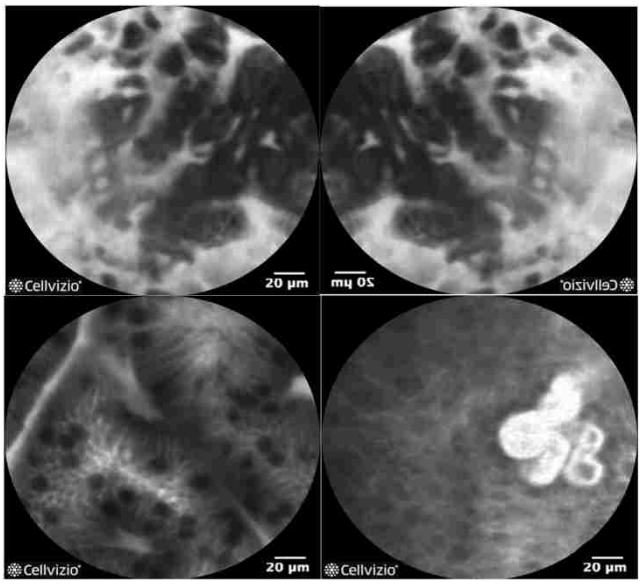

Figure 1.6 pCLE images of normal tissue, BE, HGD, and EAC.[2]

1.3.2 Biopsy methods

In a study looking at 30 esophagectomy specimen, the median surface area of BE, LGD, HGD, and EAC were found to be 32, 13, 1.3, and 1.1 cm^2, respectively, thus demonstrating the focal nature of HGD and EAC.[38] Systemic four-quadrant biopsy, where tissue is collected from four quadrants at 2-cm intervals along the entire length of BE from the end of the esophagus to the squamocolumnar junction, is recommended by the American College and British Society of Gastroenterology.[39] The Seattle protocol reported by Reid et al in 2000 is a more rigorous biopsy method in which tissues are

collected at 1-cm intervals in BE using jumbo forceps and a turn-and-suction technique.[40] Increasing tissue sampling size and size of biopsy specimen is one approach that clinicians have taken to increase the chances of detecting HGD. However, it is still under debate whether there is a clear benefit to this approach.[41]

1.3.3 Pathological analysis of biopsies

After biopsy collection, tissues are sent to pathology where they are sectioned and stained with hematoxylin and eosin (H&E) for histological examination. Based on a number of cytological and architectural features, tissues are graded as 1 of 5 tiers: 1) negative for dysplasia 2) indefinite for dysplasia 3) low-grade dysplasia 4) high-grade dysplasia and 5) carcinoma. Tissues with HGD are characterized by depolarization of nuclei, nuclear atypia, hyperchromatism, lack of surface maturation and architectural complexity, and distortion of glandular architecture.[42,43]

1.4 Emerging Methods for HGD Imaging and Detection

Molecular imaging, the imaging of biochemical alterations at the molecular to cellular level, is a method that is current being developed for HGD detection. Fluorescently-labeled targeting ligands are used in some instances where there is a well-established increased or reduced expression of a cell surface receptor in diseased tissues. However, the lack of validated biomarkers for HGD has resulted in the simultaneous search for suitable targets and corresponding targeting ligands. Recent notable work includes the identification of a 7-residue peptide targeting ligand (SNFYMPL) through *in vitro* phage display[44] as well as the use of wheat germ agglutinin (WGA) to target sialic acid which has progressively reduced expression through the metaplasia-dysplasia-adenocarcinoma sequence[45]. Peptides are a versatile class of targeting ligands as they are small, easy to produce using controlled methods of synthesis, and exhibit rapid binding kinetics. Li et al. isolated

SNF-peptides through phage selection against an esophageal adenocarcinoma cell line and through removal of phage binding a cell line established from non-dysplastic BE. Fluorescently-labeled SNF-peptides bound preferentially to dysplastic tissues *ex vivo*. However, the target to which it binds is unknown. In the latter study, Bird-lieberman et al. demonstrated increased gene expression in four pathways mediating the biosynthesis and degradation of glycans during the progression from BE to EAC using gene set enrichment analysis. Lectin arrays were subsequently used to identify lectins that bound tissue lysates from across the progression sequence. 4 lectins, *Aspergillus oryzae* lectin (AOL), *Helix pomatia* agglutinin (HPA), *Trichosanthes japonica* agglutinin-I (TJA-I) and *Tritiicum vulgare* agglutinin (WGA), were found to bind to normal tissue with progressively less binding in pathologic tissues. Fluorescently-labeled WGA was used as a negative contrast agent *ex vivo* to validate their findings.

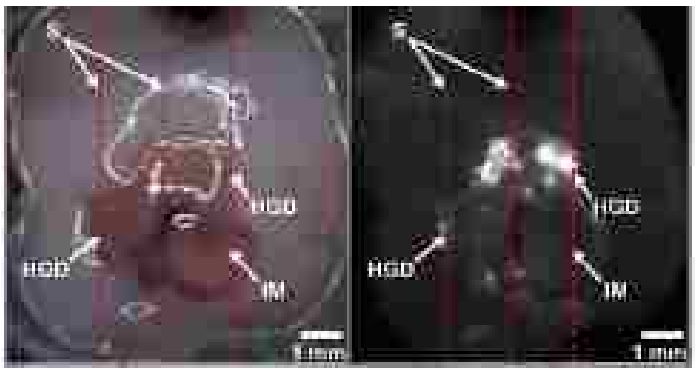

Figure 1.7 Stereomicroscope image of resected esophageal specimen (left) and fluorescence image of specimen labeled with FITC-SNF peptide (right).[44]

1.5 Future Perspectives

Contrast generated using light absorption and reflectance of untreated tissues is the cleanest, least complex method of HGD imaging. In an ideal situation, there would be no need for exogenous contrast agents. However, contrast from tissue alone has proven insufficient for identification of HGD. For comprehensive characterization of the epithelium, chromoendoscopy is a useful tool. Upregulation or downregulation of multiple macromolecules in the extracellular matrix in HGD suggests that molecular imaging using multiple targeted contrast agents may be useful in the identification of

abnormal tissues which should be biopsied for pathological analysis. Higher magnification imaging such as that used for confocal laser endomicroscopy is also helpful for finding subtle changes in cells and tissues. Therefore, a combination of high magnification imaging modality and molecular contrast agents is a promising approach to identifying HGD.

References

1. Yang, L., et al. Inflammation and intestinal metaplasia of the distal esophagus are associated with alterations in the microbiome. Gastroenterology 137, 588-597 (2009).
2. Pei, Z., et al. Bacterial biota in the human distal esophagus. Proc Natl Acad Sci U S A 101, 4250-4255 (2004).
3. Clinic, C. Esophageal Cancer. Vol. 2013.
4. Jankowski, J.A., et al. Molecular evolution of the metaplasia-dysplasia-adenocarcinoma sequence in the esophagus. Am. J. Pathol. 154, 965-973 (1999).
5. Montgomery, E., et al. Dysplasia as a predictive marker for invasive carcinoma in Barrett esophagus: A follow-up study based on 138 cases from a diagnostic variability study. Hum. Pathol. 32, 379-388 (2001).
6. Ong, C.A., Lao-Sirieix, P. & Fitzgerald, R.C. Biomarkers in Barrett's esophagus and esophageal adenocarcinoma: predictors of progression and prognosis. World J Gastroenterol 16, 5669-5681 (2010).
7. Heitmiller, R.F., Redmond, M. & Hamilton, S.R. Barrett's esophagus with high-grade dysplasia. An indication for prophylactic esophagectomy. Annals of surgery 224, 66-71 (1996).
8. Hamilton, S.R. & Smith, R.R. The relationship between columnar epithelial dysplasia and invasive adenocarcinoma arising in Barrett's esophagus. American journal of clinical pathology 87, 301-312 (1987).
9. Reid, B.J., Levine, D.S., Longton, G., Blount, P.L. & Rabinovitch, P.S. Predictors of progression to cancer in Barrett's esophagus: baseline histology and flow cytometry identify low- and high-risk patient subsets. Am J Gastroenterol 95, 1669-1676 (2000).
10. Rice, T.W., Falk, G.W., Achkar, E. & Petras, R.E. Surgical management of high-grade dysplasia in Barrett's esophagus. Am J Gastroenterol 88, 1832-1836 (1993).
11. Edwards, M.J., Gable, D.R., Lentsch, A.B. & Richardson, J.D. The rationale for esophagectomy as the optimal therapy for Barrett's esophagus with high-grade dysplasia. Annals of surgery 223, 585-589; discussion 589-591 (1996).
12. Wong, A. & Fitzgerald, R.C. Epidemiologic risk factors for Barrett's esophagus and associated adenocarcinoma. Clinical gastroenterology

and hepatology : the official clinical practice journal of the American Gastroenterological Association 3, 1-10 (2005).
13. Kuipers, E.J., et al. Atrophic gastritis and Helicobacter pylori infection in patients with reflux esophagitis treated with omeprazole or fundoplication. The New England journal of medicine 334, 1018-1022 (1996).
14. Lagergren, J. & Lagergren, P. Recent developments in esophageal adenocarcinoma. CA: a cancer journal for clinicians (2013).
15. Orloff, M., et al. Germline mutations in MSR1, ASCC1, and CTHRC1 in patients with Barrett esophagus and esophageal adenocarcinoma. JAMA : the journal of the American Medical Association 306, 410-419 (2011).
16. Zhai, R., et al. Genetic polymorphisms of VEGF, interactions with cigarette smoking exposure and esophageal adenocarcinoma risk. Carcinogenesis 29, 2330-2334 (2008).
17. Menke, V., et al. Functional single-nucleotide polymorphism of epidermal growth factor is associated with the development of Barrett's esophagus and esophageal adenocarcinoma. Journal of human genetics 57, 26-32 (2012).
18. Cheung, W.Y., et al. Single nucleotide polymorphisms in the matrix metalloproteinase gene family and the frequency and duration of gastroesophageal reflux disease influence the risk of esophageal adenocarcinoma. International journal of cancer. Journal international du cancer 131, 2478-2486 (2012).
19. McElholm, A.R., et al. A population-based study of IGF axis polymorphisms and the esophageal inflammation, metaplasia, adenocarcinoma sequence. Gastroenterology 139, 204-212 e203 (2010).
20. Jung, H.C., et al. A distinct array of proinflammatory cytokines is expressed in human colon epithelial cells in response to bacterial invasion. The Journal of clinical investigation 95, 55-65 (1995).
21. Suzuki, H., Iijima, K., Scobie, G., Fyfe, V. & McColl, K.E. Nitrate and nitrosative chemistry within Barrett's oesophagus during acid reflux. Gut 54, 1527-1535 (2005).
22. Parsonnet, J., et al. Helicobacter pylori infection and the risk of gastric carcinoma. The New England journal of medicine 325, 1127-1131 (1991).
23. Polk, D.B. & Peek, R.M., Jr. Helicobacter pylori: gastric cancer and beyond. Nature reviews. Cancer 10, 403-414 (2010).
24. Gagliardi, D., et al. Microbial flora of the normal esophagus. Diseases of the esophagus : official journal of the International Society for Diseases of the Esophagus / I.S.D.E 11, 248-250 (1998).
25. Pajecki, D., et al. Megaesophagus microbiota: a qualitative and quantitative analysis. Journal of gastrointestinal surgery : official

journal of the Society for Surgery of the Alimentary Tract 6, 723-729 (2002).
26. Pei, Z., et al. Bacterial biota in reflux esophagitis and Barrett's esophagus. World J Gastroenterol 11, 7277-7283 (2005).
27. Osias, G.L., et al. Esophageal bacteria and Barrett's esophagus: a preliminary report. Dig Dis Sci 49, 228-236 (2004).
28. Yang, L., Francois, F. & Pei, Z. Molecular pathways: pathogenesis and clinical implications of microbiome alteration in esophagitis and Barrett esophagus. Clin Cancer Res 18, 2138-2144 (2012).
29. Haidry, R. & Lovat, L. Novel Imaginig Techniques in Gastrointestinal Endoscopy in the Upper Gastrointestinal Tract. in Medical Imaging in Clinical Practice (ed. Erondu, O.F.) (2013).
30. Falk, G.W., Rice, T.W., Goldblum, J.R. & Richter, J.E. Jumbo biopsy forceps protocol still misses unsuspected cancer in Barrett's esophagus with high-grade dysplasia. Gastrointestinal endoscopy 49, 170-176 (1999).
31. Singh, R., Mei, S.C. & Sethi, S. Advanced endoscopic imaging in Barrett's oesophagus: a review on current practice. World J Gastroenterol 17, 4271-4276 (2011).
32. Sharma, P., et al. The utility of a novel narrow band imaging endoscopy system in patients with Barrett's esophagus. Gastrointestinal endoscopy 64, 167-175 (2006).
33. Kiesslich, R., Hahn, M., Herrmann, G. & Jung, M. Screening for specialized columnar epithelium with methylene blue: chromoendoscopy in patients with Barrett's esophagus and a normal control group. Gastrointestinal endoscopy 53, 47-52 (2001).
34. Wo, J.M., et al. Comparison of methylene blue-directed biopsies and conventional biopsies in the detection of intestinal metaplasia and dysplasia in Barrett's esophagus: a preliminary study. Gastrointestinal endoscopy 54, 294-301 (2001).
35. Mannath, J., Subramanian, V., Hawkey, C.J. & Ragunath, K. Narrow band imaging for characterization of high grade dysplasia and specialized intestinal metaplasia in Barrett's esophagus: a meta-analysis. Endoscopy 42, 351-359 (2010).
36. Kiesslich, R., et al. In vivo histology of Barrett's esophagus and associated neoplasia by confocal laser endomicroscopy. Clinical gastroenterology and hepatology : the official clinical practice journal of the American Gastroenterological Association 4, 979-987 (2006).
37. Sharma, P., et al. Real-time increased detection of neoplastic tissue in Barrett's esophagus with probe-based confocal laser endomicroscopy: final results of an international multicenter, prospective, randomized, controlled trial. Gastrointestinal endoscopy 74, 465-472 (2011).

38. Cameron, A.J. & Carpenter, H.A. Barrett's esophagus, high-grade dysplasia, and early adenocarcinoma: a pathological study. Am J Gastroenterol 92, 586-591 (1997).
39. Abela, J.E., et al. Systematic four-quadrant biopsy detects Barrett's dysplasia in more patients than nonsystematic biopsy. Am J Gastroenterol 103, 850-855 (2008).
40. Reid, B.J., Blount, P.L., Feng, Z. & Levine, D.S. Optimizing endoscopic biopsy detection of early cancers in Barrett's high-grade dysplasia. Am J Gastroenterol 95, 3089-3096 (2000).
41. Kariv, R., et al. The Seattle protocol does not more reliably predict the detection of cancer at the time of esophagectomy than a less intensive surveillance protocol. Clinical gastroenterology and hepatology : the official clinical practice journal of the American Gastroenterological Association 7, 653-658; quiz 606 (2009).
42. Johns Hopkins University, D.o.P. Grading dysplasia in Barrett's esophagus. (2013).
43. Clinic, C. Endoscopic Surveillance Overview. (2013).
44. Li, M., et al. Affinity peptide for targeted detection of dysplasia in Barrett's esophagus. Gastroenterology 139, 1472-1480 (2010).
45. Bird-Lieberman, E.L., et al. Molecualr imaging using fluorescent lectins permits rapid endoscopic identification of dysplasia in Barrett's esophagus. Nature Medicine 18, 315-321 (2012).

Chapter 2

ANTIBODY-TARGETED FLUORESCENT NANOPARTICLES FOR IMAGING EGFR *IN VITRO* AND IN *EX VIVO* HUMAN ESOPHAGEAL SPECIMEN

Leslie W. Chan, Yak-Nam Wang, Lih Y. Lin, Melissa P. Upton, Joo Ha Hwang, Suzie H. Pun

Abstract

Molecular imaging, the visualization of molecular and cellular markers, is a promising method for detection of dysplasia and early cancer in the esophagus and can potentially be used to identify regions of interest for biopsy or tumor margins for resection. EGFR is a previously-reported cell surface receptor with stepwise increases in expression during the progression from Barrett's metaplasia to adenocarcinoma. In this work, a 200-nm fluorescent nanoparticle contrast agent was synthesized for targeted imaging of EGFR through a series of surface modifications to dye-encapsulated polystyrene particles. Amino-functionalized polystyrene particles were PEGylated using a heterobifunctional PEG linker. Subsequently, thiolated M225 antibodies were conjugated to maleimide functional groups on attached PEGs for EGFR targeting. *In vitro* binding studies using flow cytometry demonstrated specific binding of M225-PEG-NP to EGFR-expressing cells with minimal non-specific binding in $EGFR^-$ cells. Binding was shown to increase proportionally with the number of conjugated M225 antibodies. Adsorbed formulations with unmodified M225 antibodies, M225 + PEG-NP, were synthesized using the same antibody feeds used in M225-PEG-NP synthesis to determine the contribution of adsorbed antibodies to EGFR targeting. Adsorbed antibodies were less efficient at mediated nanoparticle targeting to EGFR than conjugated antibodies. Finally, M225-PEG-NP demonstrated binding to EGFR-expressing regions in human esophageal tissue sections.

This chapter was published in *Bioconjugate Chemistry*, **24**, 167-175.

2.1 Introduction

Esophageal adenocarcinoma (EAC) is an epithelial cancer arising from the columnar glandular epithelium, and it has dramatically increased in

incidence in recent decades.[1] Patients with Barrett's esophagus (BE) have an increased risk of developing EAC.[2] Barrett's esophagus is a metaplastic condition caused by gastroesophageal reflux disease (GERD) in which oxidative stress from chronic exposure to gastric acids leads squamous epithelium in the esophagus to change into columnar epithelium.[3,4] From Barrett's metaplasia, tissue may progress into premalignant dysplastic tissue and, finally, to adenocarcinoma, a phenomenon referred to as the metaplasia-dyplasia-adenocarcinoma sequence.[5,6] High-grade dysplasia (HGD) is a validated predictive marker for adenocarcinoma and approximately 59% of patients with BE with HGD progress to EAC within 5 years of diagnosis.[7-10] Pre-emptive measures such as esophageal mucosal resections, ablative therapies, or esophagectomies may be prescribed when high-grade dysplastic lesions or intramucosal adenocarcinoma are found in Barrett's tissue. Current clinical practice for diagnosis involves endoscopic imaging and four-quadrant biopsy of Barrett's tissue, which is easily visible due to its characteristic salmon pink coloration. However, dysplastic BE is not easily distinguishable from non-dysplastic BE using conventional white light endoscopy and the former can present in small patches and be multifocal. Thus, biopsy samples are prone to sampling error potentially resulting in false negative findings for dysplasia as well as cancer.[11,12] Contrast agents labeling areas with dysplasia in Barrett's esophagus are potentially useful tools to direct biopsy of areas with the greatest probability of dysplasia or cancer.

Imaging of aberrant molecular expression in cells and tissues is a promising method for early detection of dysplasia or cancer since molecular changes occur at earlier time points than visible physical changes.[13] Targeted fluorescent contrast agents have been developed for the purpose of molecular imaging and have recently been shown to be effective in labeling dysplastic and cancerous tissue for endoscopic imaging.[14-17] These contrast agents were synthesized through bioconjugation of proteins or peptides to fluorophores. Li

et al reported the isolation of a peptide against dysplastic mucosa using phage display and further demonstrated preferential binding of the peptide-flourescein isothiocyanate (FITC) conjugate to Barrett's esophagus with dysplasia.[15] More recently, Bird-Lieberman *et al.* demonstrated the use of Alexa Fluor 680-conjugated wheat germ agglutinin (WGA) as a negative contrast agent for sialic acid which has decreased expression in EAC compared to non-dysplastic Barrett's esophagus.[17]

The aforementioned peptide and protein constructs demonstrate the potential of molecular imaging for early detection of dysplasia in the esophagus. However, there is still a need for improvement of the current contrast agents. Peptide ligands have relatively low binding affinity to their targets (typical K_D ~10-100 μM compared to nanomolar affinities for antibodies). In addition, fluorophores directly conjugated to ligands are susceptible to photobleaching when exposed to light and oxygen.[18] In contrast, fluorophore-loaded polystyrene nanoparticles (NP) exhibit high photostability due to partitioning of dyes from the oxygenated environment.[18,19] These fluorescent NP are commercially-available in well-characterized formulations in a range of sizes and colors. In addition, these particles are highly fluorescent (e.g. over 100,000 fluorophore equivalents in a 200-nm particle). Amino- and carboxylic acid-modified NP can be readily functionalized with ligands for molecular recognition. Thus, NP-based formulations of targeted contrast agents have the advantage of better photostability *in vivo* as well as greater equivalent fluorophore signal per binding event with fluorescence intensities much greater than that of tissue autofluorescence. Localization of these NPs on tissue would thus be easily visualized with a fluorescent endoscope.

This work reports the synthesis, characterization, and evaluation of a fluorescent NP-based imaging probe for targeted optical imaging of EGFR as a proof-of-concept for antibody-functionalized nanoparticle contrast agents for endoscopy. EGFR is a transmembrane receptor tyrosine kinase in the ErbB

family of receptors. Ligand binding to the extracellular portion of EGFR induces phosphorylation of intracellular tyrosine kinase domains leading to downstream cell signaling for proliferation, migration, invasion, and inhibition of apoptosis in cancer cells.[20] Thus, its upregulated expression has been commonly cited in the pathogenesis for many epithelial cancers and NP targeted to EGFR have been developed for both drug delivery and molecular imaging applications.[21-27] A majority of these particles were designed and evaluated for systemic delivery while very few have been synthesized with the intention of topical application in the gastrointestinal tract. Recently, EGFR expression was shown to increase in a stepwise manner during the progression from Barrett's metaplasia to low-grade dysplasia to high-grade dysplasia and finally to esophageal adenocarcinoma.[28] Therefore, differential EGFR expression during the metaplasia-dysplasia-adenocarcinoma sequence of the esophagus provides an opportunity to evaluate the potential of antibody-functionalized nanoparticles for optical molecular imaging of the esophagus.

In the present work, a fluorescence-based probe against the EGFR protein was synthesized by conjugation of M225, a murine monoclonal antibody against human EGFR, to fluorescent polystyrene NP via a polyethylene glycol (PEG) linker. Specific binding of these NP-based contrast agents to EGFR-expressing cells was tested *in vitro* in A431 and NCI-H520 cultured cells using flow cytometry. A431 is a commonly used model cell line for evaluation of EGFR targeting due to its high EGFR expression[29], and NCI-H520 has been previously shown to express no EGFR[30]. EGFR-targeted fluorescent NP were then used to label human esophageal tissue *ex vivo* to determine areas of NP localization. The heterogeneous composition and differential EGFR expression of tissues offered a more robust evaluation of EGFR-targeting NP and its potential for *in vivo* translatability.

2.2 Materials and methods

2.2.1 Synthesis and characterization of M225-PEG-NP and M225 + PEG-NP

NP with conjugated mouse anti-human EGFR monoclonal antibody, M225, (M225-PEG-NP) were prepared in the following manner. 200-nm amine-modified red fluorescent (580/605) polystyrene Fluospheres® (Invitrogen, F8763) were sonicated for 30 minutes. The Fluospheres® were then reacted with 5 molar excess of 5000 MW maleimide-PEG-SCM (Laysan Bio Inc) to surface amine groups for 2.5 hours in sodium phosphate buffer (50 mM sodium phosphate, pH 7.5) at a reaction concentration of 5 mg Fluospheres®/ml. PEGylated NP were then pelleted at 10,000 rcf for 15 min. M225 antibody (Emory Vaccine Center) was thiolated using 10 molar excess of Traut's reagent in phosphate buffered saline (50 mM sodium phosphate, 150 mM sodium chloride, pH 8) for 1 hour. Thiolated M225 antibody was purified using a PD-10 desalting column (GE Healthcare Life Sciences, 17-0851-01) pre-adsorbed with bovine serum albumin (1ml, 1% BSA in PBS) and collected fractions were concentrated with an Amicon Ultra-4 centrifugal filter (Millipore) at 4000 rcf for 10 min. Final antibody concentration was measured using a Nanodrop 2000c spectrophotometer. Thiolated M225 antibodies were added to PEGylated NPs at antibody to NP molar ratios of 100, 500, and 900 and reacted overnight under stirring conditions. M225-PEG-NP formulations were then dialyzed against deionized water in 300kDa MWCO Spectra/Por CE dialysis membranes (Spectrum, 131450) for 2 days at 4˚C to remove unreacted M225 and dialyzed for 1 day against 150 mM sodium chloride for buffer exchange.

NP with adsorbed antibodies (M225 + PEG-NP) were prepared using the same PEGylation process outlined in the previous section. Unmodified M225 antibodies were added to PEG-NP at antibody to NP molar ratios of 100, 500, and 900 and adsorbed overnight under stirring conditions. M225 + PEG-NP formulations were then dialyzed against deionized water in 300kDa MWCO Spectra/Por CE dialysis membranes for 2 days at 4˚C to remove unreacted

M225 and dialyzed for 1 day against 150 mM sodium chloride for buffer exchange.

2.2.2 Characterization of M225-PEG-NP and M225 + PEG-NP

NP were sized using dynamic light scattering (DLS; Brookhaven Instruments Zeta PALS analyzer). For antibodyquantification, M225 antibodies were radiolabeled as previously described with slight modification.[31,32] N-succinimidyl [2,3-3H] propionate in DMF (American Radiolabeled Chemicals, ART0135A) was reacted with M225 antibodies at a molar ratio of 1 radiolabel for every 5 antibodiesin pH 8.5 100 mM borate buffer with a final antibody concentration of 1 mg/ml. Radiolabeled antibodies were thiolated, purified using a PD-10 column, and reacted with PEGylated NPs as previously described to synthesize M225-PEG-NP nanoparticles. Unmodified radiolabeled antibodies were adsorbed to PEGylated NPs to yield M225 + PEG-NP. Absorbance at 280 nm and scintillation counting of an aliquot of radiolabeled antibody were used to determine counts per labeled antibody. Tritium radioactivity of radiolabeled antibodies and finished nanoparticles was measured using a Beckman LS 6500 scintillation counter. 100 µl of sample was dissolved in 5mL Ultima Gold scintillation liquid and read on the counter for 10 minutes.

2.2.3 Cell culture

Human A431 (epidermoid carcinoma) cells and NCI-H520 (lung squamous cell carcinoma) cells purchased from ATCC were maintained in DMEM and RPMI 1640 media, respectively. Media was supplemented with 10% fetal bovine serum and 1% antibiotic antimycotic solution. EGFR expression in A431 and NCI-H520 cells was evaluated using flow cytometry to confirm that A431 cells are $EGFR^+$ and NCI-H520 cells are $EGFR^-$. Cells were incubated with 300 µl of 5 µg/ml M225 antibody in FACS buffer (1% bovine serum albumin in PBS) for 15 minutes at 4˚C, washed twice, and incubated in 300

ul of a 1:100 dilution of FITC-conjugated sheep anti-mouse IgG in FACS buffer. Cells were washed twice and then analyzed by flow cytometry (Supporting Information Figure S1).

2.2.4 In vitro binding studies to EGFR$^+$ and EGFR$^-$ cell line

Preferential and specific binding of M225-PEG-NP nanoparticles to EGFR-expressing cells was confirmed using flow cytometry. 2×10^5 A431 (EGFR$^+$) cells and NCI-H520 (EGFR$^-$) cells were incubated with 300 µL of 10 pM M225-PEG-NP formulations for 15 minutes at 37˚C and washed twice using FACS buffer solution. 10 pM nanoparticle concentrations were used because it was determined to be the concentration at which bimodal populations in M225-PEG-NP-treated cells did not exist (data not shown), and at which fluorescence intensities would not saturate the detector for flow cytometry. For competitive conditions, both cell types were pre-blocked with 300 µL of free M225 antibody (13.3 µM in FACS buffer) for 1 hour at room temperature. Following pre-blocking, cells were incubated with 300 µL of 10 pM M225-PEG-NP formulations for 15 minutes at 37˚C and washed twice with FACS buffer. Flow cytometry was then completed using a Miltenyi MACSQuant Analyzer. The extent of binding due to adsorbed antibodies versus chemically conjugated antibodies was determined by comparing binding observed in formulations with unmodified M225 antibody versus formulations with thiolated M225 antibody. To further show specificity of M225-PEG-NP to EGFR, H520 and A431 cells were grown on glass coverslips and treated with PEG-NP or M225-PEG-NP for 30 minutes at room temperature, counterstained with 2 µg/mL DAPI for 10 minutes, mounted onto slides with Fluoromount, and imaged using a Zeiss LSM 510 META confocal microscope.

2.2.5 In vitro cytotoxicity studies

$5x10^5$ H520 and A431 cells were treated with 200 µL unmodified NP, PEG-NP, and M225-PEG-NP (10 pM-76 nM, 0.026-2.0 mg/mL)in phosphate buffered saline (PBS) for 1 hr at 37˚C. Cells were washed twice and incubated with 300 µl of 5 µg/ml DAPI in PBSfor 5 minutes at room temperature. DAPI was used as a viability exclusion dye to stain dead or dying cells as previously described[33] since other available viability exclusion dyes had significant spectral overlap with NPs. Cells were washed twice more, and flow cytometry was completed. H520 and A431 cells treated with DAPI only were used as negative controls for cell death while cells treated with 0.2 mg/ml poly(ethylenimine) (PEI) and DAPI were used as positive controls for cell death. Cells on DAPI versus forward scatter dot plots were gated to determine the percentage of $DAPI^-$ cells which correlate to the percentage of live cells.

2.2.6 Ex vivo M225-PEG-NP labeling of EGFR in human esophageal tissues

Approval from the University of Washington institutional review board (IRB) was obtained to acquire tissue from patients with Barrett's esophagus and EAC. Informed consent was obtained from patients undergoing endoscopy procedures for collection of esophageal biopsy specimen for research purposes. Endoscopic biopsies were fresh frozen in OCT and sectioned into 7 µm-thick sections. Sections were stained with hematoxylin and eosin and classified by a pathologist as normal esophagus squamous (SQ), Barrett's metaplasia (BE), low-grade (LGD), high-grade dysplasia (HGD), and esophageal adenocarcinoma (EAC). In total, 13 biopsy samples (3 SQ, 5 BE, 1 BE and EAC, 3 EAC, and 1 EAC and HGD) from 6 patients were used for histology. Tissue sections were stained for EGFR using M225 antibody and the secondary Alexa Fluor® 488 goat anti-mouse IgG (Invitrogen). Adjacent tissue sections were stained with M225-PEG-NP for 30 minutes at 37˚C and counterstained with DAPI for 10 minutes at room temperature to demonstrate localization of M225-PEG-NP in areas of EGFR expression.

Adjacent tissue sections were incubated with PEG-NP for 30 minutes at 37˚C as negative controls. Sections were then imaged using a Zeiss LSM 510 META confocal microscope.

2.2.7 Statistical analysis

Student t-tests were completed to determine statistical significance of the binding data. P-values less than 0.05 were considered significant.

2.3 Results and Discussion

2.3.1 Synthesis and characterization of M225-PEG-NP and M225 + PEG-NP

Anti-EGFR fluorescent NPs were synthesized by conjugation of the M225 murine antibody to polystyrene particles via a PEG linker. Unmodified polystyrene NPs are prone to flocculation in the presence of proteins and in physiologic salt concentrations.[34] Particles were therefore PEGylated to increase the hydrophilicity of NP surfaces and prevent NP aggregation, to neutralize charge from surface amine groups thereby minimizing nonspecific binding to cells, and to provide a point of attachment for the targeting ligand. Intervening linkers have been previously shown to be more effective for antibody conjugation to nanoparticle surfaces than direct conjugation possibly due to reduced steric hindrance from bulky nanoparticle surfaces.[35] PEG linkers with 5000 Da were selected because this size has been previously demonstrated to provide sufficient steric stabilization to keep nanoparticles disperse in physiologic conditions.[36]

Initially, varying ratios of shorter (2k) monofunctional mPEG-SCM to longer (5k) heterobifunctional maleimide-PEG-SCM (10:0, 7:3, 5:5, 3:7, 0:10) were reacted to amino-functionalized fluorescent polystyrene NPs for more protruded display of M225 antibodies from NP surfaces. The use of bidispersed protective polymers has been reported to provide improved receptor binding by displayed targeting ligands.[37,38] The shorter polymer is proposed to increase accessibility of ligands conjugated to the longer polymer

chain while providing a protective brush layer to the particle surface. However, introduction of shorter 2000 MW mPEG-SCM increased the amount of non-specific cell interaction of NP as assessed by flow cytometry (data not shown). This may be attributed to less effective charge shielding of residual protonated amine groups thus allowing electrostatic interaction between negative cell plasma membranes and positive NP surfaces. Surface-conjugated PEG has been shown to exist in two conformations: the mushroom conformation or brush conformation of which the former has poorer shielding capabilities. In general, larger PEG favor the brush conformation.[39] In light of this, only 5000 MW maleimide-PEG-SCM was used to PEGylate NPs. Following PEGylation, thiolated M225 antibodies were reacted to maleimide groups on NP-attached PEG linkers for targeting to EGFR (**Scheme 1**).

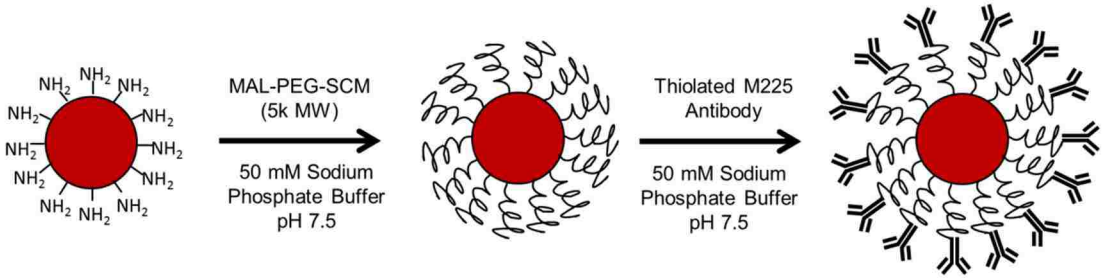

Scheme 1 Synthesis of M225-PEG-NP nanoparticles. Note: not drawn to scale.

The stability of M225-PEG-NP in suspension could be observed macroscopically. Unmodified NP controls sedimented during storage at 4˚C while PEGylated formulations stayed in suspension. Particle size measurements from DLS indicate minor aggregation in nanoparticle formulations in 150 mM sodium chloride solution (**Table 1**). The effective diameter for unmodified and PEGylated nanoparticles were 640 ± 9 and 500 ± 4 nm, respectively. Thus, PEGylation was shown to reduce aggregation. Nanoparticles with conjugated or adsorbed M225 had effective diameters

ranging from 505-586 nm and 523-735 nm, respectively, with diameter increasing proportionally with antibody feed.

The average number of M225 associated per particle was quantified by antibody radiolabeling. Addition of thiolated M225 to PEGylated NP at molar ratios of 100, 500, and 900 yielded M225-PEG-NP with an average of 12, 60, and 89 antibodies per nanoparticle, respectively, corresponding to ~10-12% conjugation efficiency. These efficiencies are comparable to those previously observed in conjugation of M225 antibodies to gold surfaces using dithiol-PEG-hydrazide linkers, which is a highly favorable reaction due to the presence of dense conjugation sites provided by surface Au atoms.[40]

To account for the effect of non-specific antibody adsorption to NP surfaces, PEGylated NP were also incubated with non-thiolated, unreactive M225. These formulations are termed "M225 + PEG-NP." Incubation of unreactive M225 with PEG-NP at molar ratios of 100, 500, and 900 yielded NP with on average 7, 36, and 62 associated antibodies per particle. Thus, antibody loading by non-specific NP adsorption is ~30-40% lower.

Table 1 Properties of M225-PEG-NP and M225 + PEG-NP formulations.

Sample	Molar Feed Ratio of Thiolated Antibody to NP	Molar Feed Ratio of Unmodified Antibody to NP	Number of Conjugated or Absorbed Antibody Per NP	Effective Diameter (nm)	Standard Deviation (nm)	Polydispersity
Unmodified NP	---	---	---	639.5	8.9	0.068
PEG-NP	---	---	---	500.2	3.6	0.137
M225-PEG-NP (100)	100	---	12	505.3	7.1	0.181
M225 + PEG-NP (100)	---	100	7	520.3	4.0	0.217
M225-PEG-NP (500)	500	---	60	537.4	3.9	0.209
M225 + PEG-NP (500)	---	500	36	678.2	11.2	0.274
M225-PEG-NP (900)	900	---	89	585.6	10.3	0.208
M225 + PEG-NP (900)	---	900	62	735.3	20.3	0.289

2.3.2 Specific and M225-dose dependent binding of M225-PEG-NP to EGFR$^+$ cells

The antibody-modified NPs were tested as EGFR-specific probes using $EGFR^+$ A431 epithelial carcinoma cells and $EGFR^-$ H520 lung carcinoma cells. The EGFR expression of these cell lines were confirmed by flow cytometry (Supporting Information Figure 1). Cultured cells were treated with PEG-NP and M225-PEG-NP formulations for 15 min at 37˚C before particle association with cells was determined by flow cytometry. A431 ($EGFR^+$) cells treated with M225-PEG-NP 100, 500, 900 nanoparticles had mean fluorescence intensities (MFI) of 6.8 ± 1.0, 48.0 ± 6.5, and 88.9 ± 8.0, respectively, which were significantly greater ($p < 0.05$) than fluorescence intensities of untreated controls and A431 cells treated with PEGylated NPs (1.7 ± 0.0 and 2.1 ± 0.0, respectively) (**Figure 2.1**). M225-PEG-NP exhibited no significant binding in $EGFR^-$ H520 cells ($p > 0.05$). Thus, conjugation of M225 to the surface of PEGylated NP resulted in efficient labeling of $EGFR^+$ cells. In addition, M225-PEG-NP nanoparticles exhibited antibody dose-dependent binding to EGFR-expressing cells with binding increasing proportionally with number of conjugated antibodies.

To confirm binding specificity of M225-PEG-NP to EGFR, both cell lines were pre-treated with free M225 antibody to block EGFR and subsequently treated with M225-PEG-NP (**Figure 2.1**). Resulting fluorescence intensities (2.2 ± 0.1, 2.8 ± 0.7, 3.1 ± 0.4 for M225-PEG-NP 100, 500, and 900, respectively) were comparable to baseline fluorescence intensities of untreated cells (1.8 ± 0.0) and of A431 cells treated with PEGylated NPs (2.2 ± 0.1). This indicates that the majority of binding observed in A431 cells without M225 pre-treatment was due to specific binding of NP-bound M225 antibodies to EGFR rather than non-specific differences, such as differences in phagocytic activity of the cells. No changes in binding behavior were observed in H520 cells.

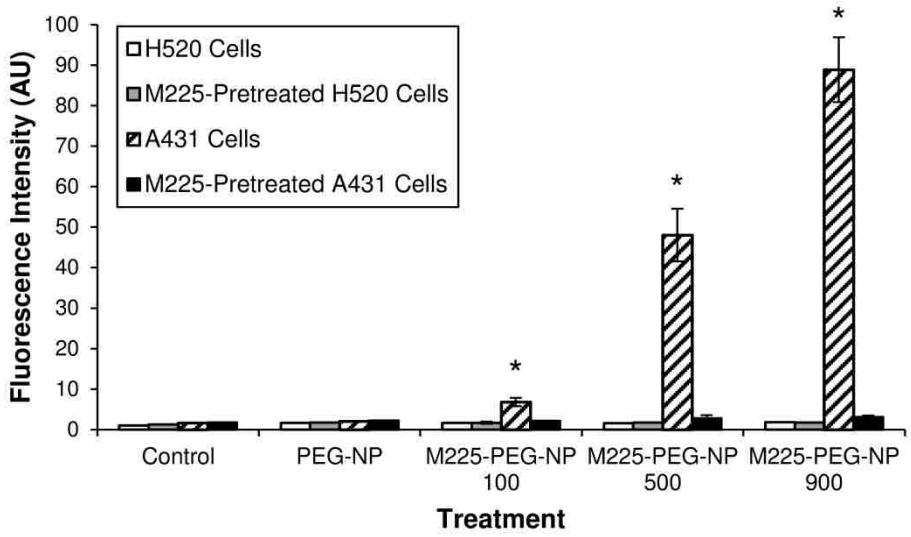

Figure 2.1 Specific and M225 dose-dependent binding of M225-PEG-NP to EGFR+ cells. M225-PEG-NP nanoparticles show significantly greater binding to A431 (EGFR+) cells compared to untreated controls, A431 cells treated with PEGylated beads, and M225-preblocked A431 cells treated with M225-PEG-NP nanoparticles *($p < 0.05$) thus demonstrating binding specificity of nanoparticles for EGFR. Nanoparticle binding to A431 cells was directly proportional to the number of surface-conjugated M225 antibodies. PEGylated beads and M225-PEG-NP nanoparticles showed no significant binding in H520 (EGFR-) cells ($p > 0.05$).

Confocal images of H520 and A431 cells treated with PEG-NP and M225-PEG-NP support binding specificity of M225-PEG-NP to EGFR (**Figure 2.2**). PEG-NP-treated cells demonstrated no background signal, and M225-PEG-NP-treated A431 cells showed significantly greater fluorescence signal compared to H520 cells.

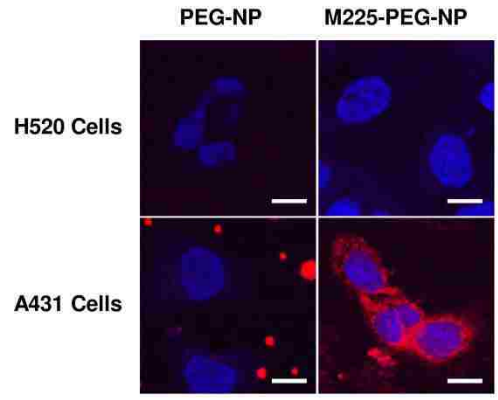

Figure 2.2 Confocal images of *in vitro* staining of H520 ($EGFR^-$) cells and A431 ($EGFR^+$) cells with PEG-NP and M225-PEG-NP and DAPI.

2.3.3 Immunoreactivity of adsorbed versus conjugated M225 antibodies

Passive antibody adsorption to particle surfaces has been frequently used in applications such as immunoassays. However, immunoreactivity of adsorbed antibodies on solid supports is highly dependent on pre-activation of adsorbing surfaces, buffer pH and ionic strength, and temperature as these factors will affect antibody conformation and orientation.[41] In general, physical adsorption of monoclonal antibodies has been shown to reduce or eliminate antigen binding capabilities due to steric hindrance from the surface of the solid support, antibody conformational changes, as well as limited intramolecular flexibility due to multi-site attachment to the support.[41,42] Thus, there is strong motivation to conjugate M225 antibodies to NP surfaces instead of relying on passive adsorption.

To compare the effect of M225 immobilization by conjugation versus adsorption on nanoparticle binding to EGFR-expressing cells, *in vitro* binding studies using flow cytometry were completed using M225-PEG-NP and M225 + PEG-NP each prepared using 100, 500, and 900 M225 per NP. Conjugated nanoparticle formulations showed 3.58, 5.07, and 3.61 fold greater binding than adsorbed nanoparticle formulations (**Figure 2.3a**). Thus, even assuming similar levels of M225 adsorption on M225-PEG-NP as M225 + PEG-NP, this 60-70% of Ab (for M225-PEG-NP 100, $\frac{number\ of\ antibodies\ in\ M225\ +\ PEG-NP\ 100}{number\ of\ antibodies\ in\ M225-PEG-NP\ 100}\ x\ 100 = \frac{7.4}{11.9} x\ 100 = 62\%$) would be responsible for only 8-25% of binding (for M225-PEG-NP 100, $\frac{MFI_{M225\ +\ PEG-NP\ 100} - MFI_{PEG-NP}}{MFI_{M225-PEG-NP\ 100} - MFI_{PEG-NP}}\ x\ 100 = \frac{2.9-2.2}{10.5-2.2} = 8.4\%$) of M225-PEG-NP to EGFR+ cells. Reduced immunoreactivity of adsorbed antibodies could account for this discrepancy as well as masking of antigen-binding domains.[37] When lines are fitted to plots of binding versus number of surface-associated antibodies, the slope for conjugated formulations is approximately 2.6 times greater than the slope for adsorbed formulations indicating that addition of

subsequent antibodies through conjugation results in greater increases in binding activity than addition of subsequent antibodies through adsorption (**Figure 2.3b**). Thus, bioconjugation of antibodies to nanoparticle surfaces was shown to be efficient in terms of antibody loading as well as retained immunoreactivity.

2.3.4 Cytotoxicity of M225-PEG-NP

Clinical contrast agents should not have deleterious effects on normal tissue. Therefore, DAPI was used as a viability exclusion dye to quantify cell viability after treatment of cells with unmodified NP, PEG-NP, and M225-PEG-NP 900. Like propidium iodide (PI), DAPI is a DNA intercalating dye which enters dead or dying cells through compromised cell membranes. H520 and A431 cells were treated with 0.026-2.0 mg/ml unmodified NP, PEG-NP, and M225-PEG-NP 900 for 1 hr at body temperature and stained with DAPI. Unmodified NP demonstrated considerably higher cytotoxicity than PEG-NP and M225-PEG-NP 900 in both cell lines. For example, survival of A431 cells treated with 0.2 mg/mL Np was only 24% but was 62% and 61% for PEG-NP and M225-PEG-NP, respectively (**Figure 2.4**). Reduction of surface charge density through PEGylation has previously been shown to reduce cytotoxicity in amine-terminated poly(amidoamine) dendrimers and may possibly contribute to the reduction of cytotoxicity in this instance.[43,44] Alternatively, particle stabilization by PEG may contribute toward improved biocompatibility of materials. Cytotoxic effects were more pronounced in the A431 cell line compared to the H520 cell line. The IC_{50} values of PEG-NP and M225-PEG-NP in H520 cells was > 2 mg/mL and in A431 cells was ~ 0.25 mg/mL for PEG-NP and ~ 0.8 mg/mL for M225- PEG-NP. These values are ~10 and 40-fold higher than expected concentrations necessary for *in vivo* applications. In addition, the incubation time of 1hr is

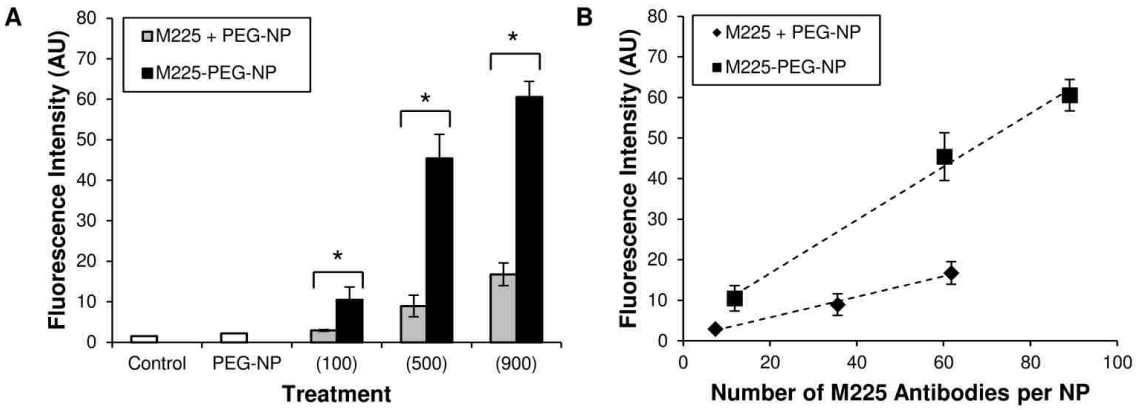

Figure 2.3 Comparison of EGFR-targeting of M225-adsorbed formulations (M225 + PEG-NP) versus M225-conjugated formulations (M225-PEG-NP). (A) *In vitro* binding studies showed significantly greater binding of M225-PEG-NP than M225+PEG-NP to A431 (EGFR+) cells *($p < 0.05$). M225-PEG-NP 100, 500, and 900 demonstrated 3.58, 5.07, and 3.61 fold greater binding than M225 + PEG-NP, respectively. (B) Fitted lines to plots of fluorescence intensity (from *in vitro* binding studies) versus number of antibodies per nanoparticle indicate lower immunoreactivity of antibodies in M225+PEG-NP compared to surface-associated antibodies in M225-PEG-NP. Slopes of the fitted lines for M225+PEG-NP and M225-PEG-NP are 0.254 and 0.657, respectively.

significantly longer than any practical application time in patients undergoing endoscopy and thus toxicities should be less than that observed in this study.

2.3.5 M225-PEG-NP labeling of EGFR in human esophageal tissues

Standard immunohistochemistry was completed on transverse tissue sections from normal esophageal squamous (3 samples from 3 patients), Barrett's metaplasia (6 samples from 3 patients), and adenocarcinoma tissue (5 samples from 3 patients) using free M225 antibody and Alexa Fluor® 488 goat anti-mouse IgG for evaluation of EGFR expression in the different tissue types. Tissues with low-grade and high-grade dysplasia were scarce, illustrating the difficulty in identifying dysplastic lesions using conventional white light endoscopy. Contrary to previous reports on EGFR expression[28,45], we found that Barrett's metaplasia tissue sections exhibited much stronger EGFR staining than adenocarcinoma tissue sections (Figure 5 and Supporting Information Figure S2, second row). As expected, EGFR staining

was weakest in normal esophagus squamous tissue sections. However, it is important to note that the tissue sample size is significantly smaller in this study than in previous studies that report the stepwise increase in EGFR staining during the histological progression from BE to EAC.[28,45]

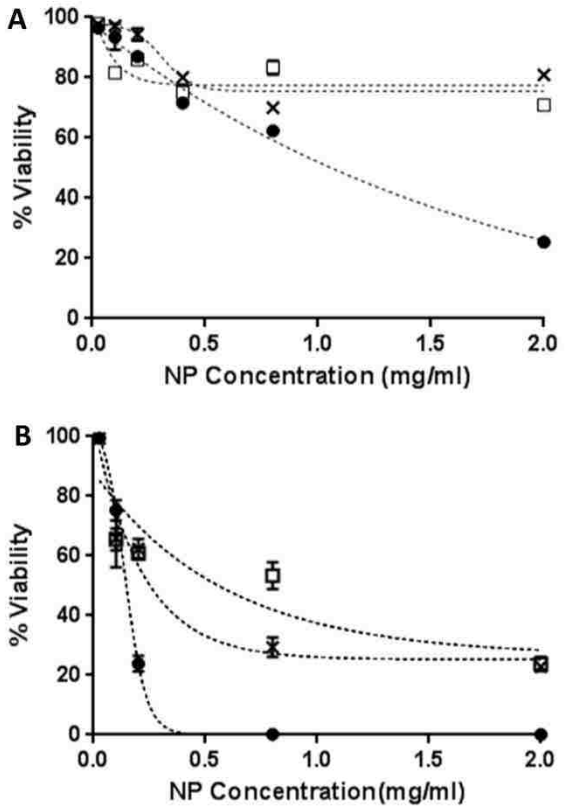

Figure 2.4 Cytotoxicity of unmodified NP (●), PEG-NP (**x**), and M225-PEG-NP (□) in H520 cells (A) and A431 cells (B) determined by flow cytometry using DAPI as a cell viability exclusion dye

Different staining patterns were observed in each type of tissue representing the histological progression from BE to EAC. EGFR stains were diffuse in esophageal adenocarcinoma tissue sections. In contrast, EGFR stains were localized in Barrett's metaplasia to the glands and columnar epithelium. In addition, stronger EGFR staining was seen in basal epithelium adjacent to Barrett's metaplasia and adenocarcinoma compared to basal epithelium from normal squamous epithelium which is consistent with observations made in cervical cancer, another example of epithelial cancer.[46] These observations suggest the potential use of EGFR as a biomarker of risk for metaplastic and neoplastic progression into adjacent tissues. For the purposes of this study, differential EGFR expression patterns in *transverse* esophageal tissue sections provided an opportunity to evaluate the binding of M225-PEG-NP for targeted imaging of EGFR under *ex vivo* conditions.

M225-PEG-NP were applied to tissue sections adjacent to EGFR-stained sections to demonstrate co-localization of EGFR and M225-PEG-NP (**Figure 2.5, second and fourth row**). M225-PEG-NP demonstrated minimal binding in esophagus squamous epithelium and esophageal adenocarcinoma. The greatest amount of binding was observed in Barrett's metaplasia tissue with localization of nanoparticles in areas of concentrated EGFR expression. Slight differences in staining can be attributed to the two stains being on adjacent sections rather than on the same tissue sections. The latter was not possible due to possible artifacts from interaction of NP-bound M225 antibodies and fluorescent secondary antibodies used for IHC. Differences in staining can also be attributed to tissue contour. Nanoparticles are more likely to be physically entrapped by tissues on slides during the staining process especially in the case of *transverse* tissues. Adjacent sections incubated with PEG-NP demonstrated low background fluorescence (**Figure 2.5, third row**). Correlation between tissue pathology and extent of M225-PEG-NP binding will be further investigated *ex vivo* in larger esophageal mucosal resection (EMR) specimen in future studies. *En face* imaging of M225-PEG-NP-labeled EMR specimen will be a more suitable model for the evaluation of molecular imaging of EGFR for the detection of dysplastic Barrett's esophagus.

2.4 Conclusion

In summary, fluorescent nanoparticles for targeted optical imaging of EGFR were synthesized through a series of surface modifications to amino-functionalized dye-filled polystyrene NPs including PEGylation and bioconjugation of M225 antibodies. M225-PEG-NP demonstrated specific binding to EGFR and conjugation of M225 to NP surfaces via a PEG linker was shown to display higher immunoreactivity than direct adsorption of M225 to PEGylated NP surfaces. M225-PEG-NP were shown to bind to human esophageal tissue sections in areas of EGFR expression,

demonstrating the potential of targeted fluorescent nanoparticles for *in vivo* molecular imaging using endoscopy. Contingent on biomarker specificity, such molecular contrast agents could potentially be used for targeted biopsies during endoscopic surveillance of the gastrointestinal tract in addition to delineating tumor margins for endoscopic mucosal resectioning.

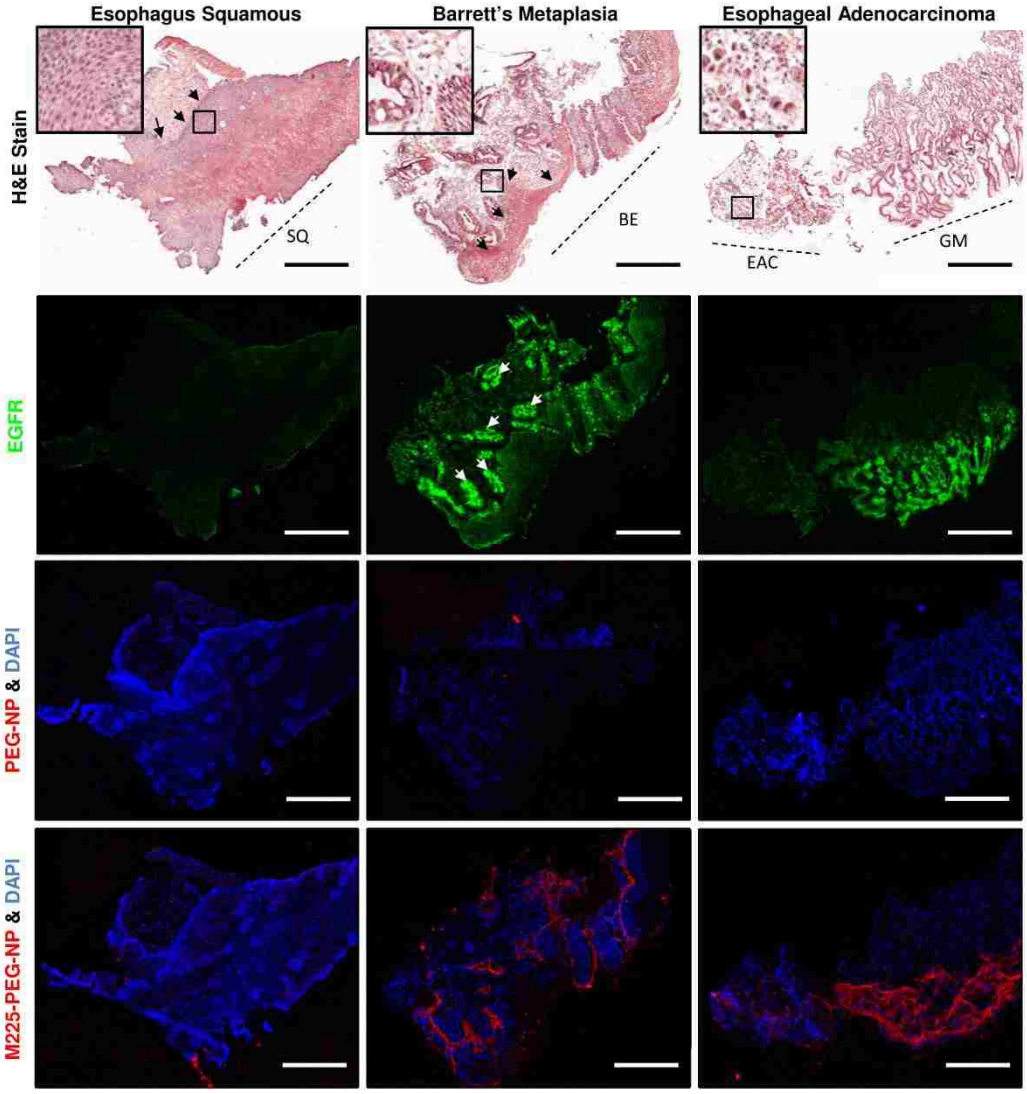

Figure 2.5 *Ex vivo* staining of esophagus squamous (SQ), Barrett's metaplasia (BE), and esophageal adenocarcinoma (EAC) and gastric mucosa (GM) biopsy sections with hematoxylin and eosin (top row), M225 antibody and Alexa Fluor 488 goat anti-mouse IgG (second row), PEG-NP with DAPI counterstain (third row), and M225-PEG-NP 900 with DAPI counterstain (bottom row). Standard immunohistochemistry (middle row) showed high EGFR expression in the glands (white arrows) and basal epithelium (black

arrows) in BE tissue sections. M225-PEG-NP bound to the same corresponding areas in adjacent tissue sections. Scale bar, 500 μm.

2.5 Acknowledgements

This work is supported by NIH EB007636. Confocal microscopy images were acquired at the University of Washington Keck Microscopy Facility.

2.6 Supporting Information

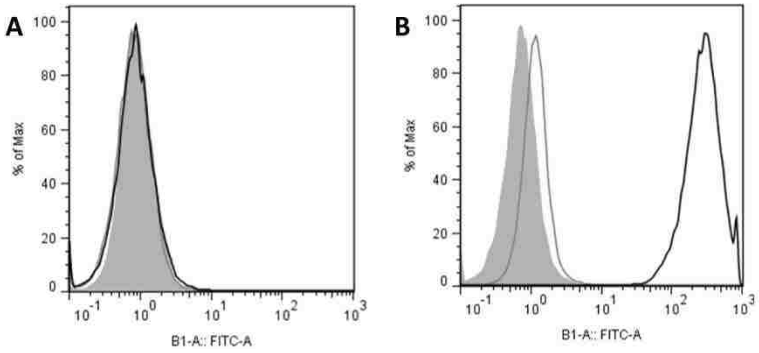

Figure S2.1 Evaluation of EGFR Expression in (A) H520 ($EGFR^-$) and (B) A431 ($EGFR^+$) cell lines using flow cytometry. Baseline fluorescence (shaded gray) in both cell lines were measured. Cells were treated with FITC-conjugated secondary antibody to determine background fluorescence (gray line). Cells were treated with M225 antibody and FITC-conjugated secondary antibody to evaluate homogeneity of EGFR expression (black line). H520 cells were negative for EGFR expression and A431 cells were positive for EGFR expression.

References

1. *Pohl, H. & Welch, H.G. The role of overdiagnosis and reclassification in the marked increase of esophageal adenocarcinoma incidence. Journal of the National Cancer Institute 97, 142-146 (2005).*
2. *Cameron, A.J., Ott, B.J. & Payne, W.S. THE INCIDENCE OF ADENOCARCINOMA IN COLUMNAR-LINED (BARRETTS) ESOPHAGUS. N. Engl. J. Med. 313, 857-859 (1985).*
3. *Wetscher, G.J., et al. Reflux esophagitis in humans is mediated by oxygen-derived free radicals. American journal of surgery 170, 552-556; discussion 556-557 (1995).*
4. *Olyaee, M., et al. Mucosal reactive oxygen species production in oesophagitis and Barrett's oesophagus. Gut 37, 168-173 (1995).*

5. *Hameeteman, W., Tytgat, G.N., Houthoff, H.J. & van den Tweel, J.G. Barrett's esophagus: development of dysplasia and adenocarcinoma. Gastroenterology 96, 1249-1256 (1989).*
6. *Jankowski, J.A., et al. Molecular evolution of the metaplasia-dysplasia-adenocarcinoma sequence in the esophagus. Am. J. Pathol. 154, 965-973 (1999).*
7. *Heitmiller, R.F., Redmond, M. & Hamilton, S.R. Barrett's esophagus with high-grade dysplasia. An indication for prophylactic esophagectomy. Annals of surgery 224, 66-71 (1996).*
8. *Hamilton, S.R. & Smith, R.R. The relationship between columnar epithelial dysplasia and invasive adenocarcinoma arising in Barrett's esophagus. American journal of clinical pathology 87, 301-312 (1987).*
9. *Montgomery, E., et al. Dysplasia as a predictive marker for invasive carcinoma in Barrett esophagus: A follow-up study based on 138 cases from a diagnostic variability study. Hum. Pathol. 32, 379-388 (2001).*
10. *Reid, B.J., Levine, D.S., Longton, G., Blount, P.L. & Rabinovitch, P.S. Predictors of progression to cancer in Barrett's esophagus: baseline histology and flow cytometry identify low- and high-risk patient subsets. Am J Gastroenterol 95, 1669-1676 (2000).*
11. *Kariv, R., et al. The Seattle protocol does not more reliably predict the detection of cancer at the time of esophagectomy than a less intensive surveillance protocol. Clinical gastroenterology and hepatology : the official clinical practice journal of the American Gastroenterological Association 7, 653-658; quiz 606 (2009).*
12. *Goldblum, J.R. Barrett's esophagus and Barrett's-related dysplasia. Modern pathology : an official journal of the United States and Canadian Academy of Pathology, Inc 16, 316-324 (2003).*
13. *Kelloff, G.J., et al. The progress and promise of molecular imaging probes in oncologic drug development. Clin. Cancer Res. 11, 7967-7985 (2005).*
14. *Hsiung, P.L., et al. Detection of colonic dysplasia in vivo using a targeted heptapeptide and confocal microendoscopy. Nat Med 14, 454-458 (2008).*
15. *Li, M., et al. Affinity peptide for targeted detection of dysplasia in Barrett's esophagus. Gastroenterology 139, 1472-1480 (2010).*
16. *Miller, S.J., et al. In vivo fluorescence-based endoscopic detection of colon dysplasia in the mouse using a novel peptide probe. PLoS One 6, e17384 (2011).*
17. *Bird-Lieberman, E.L., et al. Molecualr imaging using fluorescent lectins permits rapid endoscopic identification of dysplasia in Barrett's esophagus. Nature Medicine 18, 315-321 (2012).*
18. *Murcia, M.J. & Naumann, C.A. Biofunctionalization of fluorescent nanoparticles. in Nanotechnologies for the life sciences, Vol. 1 (ed. Kumar, C.) (Wiley-VCH Verlag GmbH, Weinheim, 2005).*

19. *Hahn, M.A., Singh, A.K., Sharma, P., Brown, S.C. & Moudgil, B.M. Nanoparticles as contrast agents for in-vivo bioimaging: current status and future perspectives. Anal Bioanal Chem 399, 3-27 (2011).*
20. *Khan, J.A., et al. Designing nanoconjugates to effectively target pancreatic cancer cells in vitro and in vivo. PLoS One 6, e20347 (2011).*
21. *El-Sayed, I.H., Huang, X. & El-Sayed, M.A. Surface plasmon resonance scattering and absorption of anti-EGFR antibody conjugated gold nanoparticles in cancer diagnostics: applications in oral cancer. Nano letters 5, 829-834 (2005).*
22. *Diagaradjane, P., et al. Imaging epidermal growth factor receptor expression in vivo: Pharmacokinetic and biodistribution characterization of a bioconjugated quantum dot nanoprobe. Clin. Cancer Res. 14, 731-741 (2008).*
23. *Yang, L.L., et al. Single Chain Epidermal Growth Factor Receptor Antibody Conjugated Nanoparticles for in vivo Tumor Targeting and Imaging. Small 5, 235-243 (2009).*
24. *Acharya, S., Dilnawaz, F. & Sahoo, S.K. Targeted epidermal growth factor receptor nanoparticle bioconjugates for breast cancer therapy. Biomaterials 30, 5737-5750 (2009).*
25. *Glazer, E.S. & Curley, S.A. Radiofrequency Field-Induced Thermal Cytotoxicity in Cancer Cells Treated With Fluorescent Nanoparticles. Cancer 116, 3285-3293 (2010).*
26. *Lee, H., Fonge, H., Hoang, B., Reilly, R.M. & Allen, C. The effects of particle size and molecular targeting on the intratumoral and subcellular distribution of polymeric nanoparticles. Molecular pharmaceutics 7, 1195-1208 (2010).*
27. *Yang, J., et al. Fluorescent magnetic nanohybrids as multimodal imaging agents for human epithelial cancer detection. Biomaterials 29, 2548-2555 (2008).*
28. *Cronin, J., et al. Epidermal growth factor receptor (EGFR) is overexpressed in high-grade dysplasia and adenocarcinoma of the esophagus and may represent a biomarker of hisotlogical progression in Barrett's esophagus (BE). Am J Gastroenterol 106, 46-56 (2011).*
29. *Masui, H., Castro, L. & Mendelsohn, J. Consumption of EGF by A431 cells: evidence for receptor recycling. The Journal of cell biology 120, 85-93 (1993).*
30. *Raben, D., et al. The effects of cetuximab alone and in combination with radiation and/or chemotherapy in lung cancer. Clinical cancer research : an official journal of the American Association for Cancer Research 11, 795-805 (2005).*
31. *Kummer, U. Tritium radiolabeling of antibodies to high specific activity with N-succinimidyl [2,3-3H]propionate: use in detecting and analyzing monoclonal antibodies. Methods Enzymol 121, 670-678 (1986).*

32. *Tang, Y.S., Davis, A.-M. & Kitcher, J.P. N-succinimidyl propionate: Characterisation and optimum conditions for use as a tritium labelling reagent for proteins. Journal of Labelled Compounds 20, 277-284 (1983).*
33. *Gordon, K.M., Duckett, L., Daul, B. & Petrie, H.T. A simple method for detecting up to five immunofluorescent parameters together with DNA staining for cell cycle or viability on a benchtop flow cytometer. J Immunol Methods 275, 113-121 (2003).*
34. *Popielarski, S.R., Pun, S.H. & Davis, M.E. A nanoparticle-based model delivery system to guide the rational design of gene delivery to the liver. 1. Synthesis and characterization. Bioconjugate chemistry 16, 1063-1070 (2005).*
35. *Lee, J., et al. Characterization and cancer cell specific binding properties of anti-EGFR antibody conjugated quantum dots. Bioconjugate Chem 21, 940-946 (2010).*
36. *Gref, R., et al. 'Stealth' corona-core nanoparticles surface modified by polyethylene glycol (PEG): influences of the corona (PEG chain length and surface density) and of the core composition on phagocytic uptake and plasma protein adsorption. Colloid Surf. B-Biointerfaces 18, 301-313 (2000).*
37. *Chen, S.F., Liu, L.Y., Zhou, J. & Jiang, S.Y. Controlling antibody orientation on charged self-assembled monolayers. Langmuir 19, 2859-2864 (2003).*
38. *Lin, J.J., et al. The effect of polymer chain length and surface density on the adhesiveness of functionalized polymersomes. Langmuir 20, 5493-5500 (2004).*
39. *Jokerst, J.V., Lobovkina, T., Zare, R.N. & Gambhir, S.S. Nanoparticle PEGylation for imaging and therapy. Nanomedicine (London, England) 6, 715-728 (2011).*
40. *Ma, L.L., et al. Selective targeting of antibody conjugated multifunctional nanoclusters (nanoroses) to epidermal growth factor receptors in cancer cells. Langmuir 27, 7681-7690 (2011).*
41. *van Erp, R., Linders, Y.E., van Sommeren, A.P. & Gribnau, T.C. Characterization of monoclonal antibodies physically adsorbed onto polystyrene latex particles. J Immunol Methods 152, 191-199 (1992).*
42. *Wood, W.G. & Gadow, A. Immobilisation of antibodies and antigens on macro solid phases--a comparison between adsorptive and covalent binding. A critical study of macro solid phases for use in immunoassay systems. Part I. J Clin Chem Clin Biochem 21, 789-797 (1983).*
43. *Wang, W., et al. The decrease of PAMAM dendrimer-induced cytotoxicity by PEGylation via attenuation of oxidative stress. Nanotechnology 20, 105103 (2009).*

44. *Fant, K., et al. Effects of PEGylation and Acetylation of PAMAM Dendrimers on DNA Binding, Cytotoxicity and in Vitro Transfection Efficiency. Molecular pharmaceutics 7, 1734-1746 (2010).*
45. *Li, Y., et al. Cyclooxygenase-2 and epithelial growth factor receptor up-regulation during progression of Barrett's esophagus to adenocarcinoma. World J Gastroenterol 12, 928-934 (2006).*
46. *Boiko, I.V., et al. Epidermal growth factor receptor expression in cervical intraepithelial neoplasia and its modulation during an alpha-difluoromethylornithine chemoprevention trial. Clinical cancer research : an official journal of the American Association for Cancer Research 4, 1383-1391 (1998).*

Chapter 3

IDENTIFICATION OF NOVEL PEPTIDES FOR ENDOSCOPIC IMAGING OF HIGH GRADE DYSPLASIA

Leslie W. Chan, Catherine Nguyen, William M. Grady, Joo Ha Hwang, Suzie H. Pun

Abstract

High grade dysplasia (HGD) is an effective predictive marker for patients at high risk for developing esophageal adenocarcinoma (EAC), but is difficult to visualize using conventional white light endoscopy. Molecular imaging of biochemical alterations characteristic to HGD is an alternative method that has great promise. In the following work, B family peptides and lone peptide sequence D22 were isolated using *in vitro* phage display. When expressed in phage, these peptides demonstrate preferential binding to two different cell-surface targets in dysplastic cell lines. Homology of isolated sequences to domains in glycan-processing enzymes suggests both peptides bind to glycan targets, which is in agreement with previous studies demonstrating increased gene expression of pathways mediating glycan biosynthesis and degradation during progression to EAC. Binding studies show that the B22 peptide binds to dysplastic cells with low affinity suggesting avidity effects are needed to optimize targeted binding to dysplastic tissues.

3.1 Introduction

Esophageal adenocarcinoma (EAC) is the cancer with the fastest growing incidence rate in developed nations.[1] EAC is the endpoint to a sequence of changes in normal tissue known as the metaplasia-dysplasia-adenocarcinoma sequence. Metaplasia in the esophagus, known as Barrett's esophagus (BE), is a condition attributed to gastroesophageal reflux disease (GERD). Chronic tissue inflammation due to repeated exposure to gastric acids causes the normally stratified squamous epithelium to be replaced by columnar epithelium more characteristic of the intestine. Over time, BE can progress to BE with low-grade dysplasia (LGD) or high-grade dysplasia (HGD) of which the latter has been shown to be an effective predictive marker for patients at high risk for developing esophageal adenocarcinoma.[2] Approximately 59% of patients with BE with HGD progress to EAC within 5 years of diagnosis.[3-6] Therefore, detection of high grade dysplasia is integral to identifying patients who should be treated or placed under more stringent surveillance for EAC.

Visualization of HGD using conventional white light endoscopy is difficult due to the flat architecture and multifocal distribution of dysplastic lesions. In addition, the effectiveness of more intensive biopsy methods such as the 4-quadrant biopsy is questionable.[7] Therefore, ongoing efforts are being made to find HGD-targeting ligands for molecular imaging of biochemical alterations characteristic to dysplastic tissues. In a 2012 publication in *Nature Medicine*, Bird-Lieberman et al. reported increased gene expression in four pathways mediating biosynthesis and degradation of glycan structures during the progression from BE to EAC. Therefore, carbohydrate-binding proteins, or lectins, are potentially viable targeting ligands. Using lectin arrays, wheat germ agglutinin (WGA) was found demonstrating high binding in normal esophageal tissue samples and decreased binding in non-dysplastic and dysplastic BE samples. In esophagectomy specimen, fluorescently-labeled WGA was shown to be an effective negative contrast agent for HGD.[8] A limitation of this system is that HGD detection is based on

negative contrast. Lesions may be as small as a millimeter in size, in which case, it would be difficult to discern the lack of staining especially given motion artifacts from breathing and peristalsis. Positive contrast for diseased areas of the esophagus is ideal.

In a preceding study, Li et al. isolated a targeting peptide using *in vitro* phage display, a high throughput screening method employing a library of bacteriophage expressing random peptide sequences. Peptide targeting ligands are advantageous compared to whole proteins because of their small molecular weight, controlled synthesis, and rapid binding kinetics. A subtractive whole cell panning approach was used in which the starting phage library was subjected to multiple cycles of subtraction, selection, and amplification. In brief, phage binding the CP-A human cell line (non-dysplastic Barrett's esophagus) were discarded (subtraction) and unbound phage were subsequently incubated with and eluted from the OE33 human cell line (esophageal adenocarcinoma) (selection). The fluorescently-labeled candidate peptide bound preferentially to OE33 cells and to dysplastic esophageal tissues *ex vivo*. However, the signal to noise ratio (SNR) in dysplastic tissues was less than that in OE33 cells. Though this can be partly attributed to non-specific binding to the extracellular matrix in tissues, it is also likely the panning strategy used was optimal for finding adenocarcinoma-binding peptides rather than for HGD-binding peptides. While EAC occurs downstream of HGD, biomolecular differences between normal epithelium and EAC are not necessarily indicative of differences that would be observed between normal epithelium and HGD and most likely not to the same extent. Therefore, a panning approach with selection against a dysplastic cell line may be necessary to isolate peptides specific to HGD to generate maximum SNR.

Herein, we report the isolation of an HGD-binding family of peptides and a lone HGD-binding peptide sequence using an *in vitro* phage display approach with selection against dysplastic cell lines. Phage libraries were

subjected to an initial selection pan against dysplastic cells with four iterations of the following: subtraction against normal esophageal keratinocytes, subtraction against CP-A cells, and selection against one of three dysplastic cell lines. Subsequent phage binding studies demonstrate preferential binding of isolated phage to the dysplastic cell lines. BLAST results suggest the cell-surface targets of these peptide sequences are glycans.

3.2 Materials and methods

3.2.1 Cell culture

EPC2 cells (human esophageal keratinocytes) were cultured in KSFM media supplemented with 50 µg/mL pituitary bovine extract (BPE), 1 ng/mL epidermal growth factor (EGF), and 1% penicillin streptomycin. CP-A cells (Barrett's esophagus) and CP-B, CP-C, and CP-D cells (high grade dysplasia, ATCC) were cultured in MCDB-153 media with 0.4 µg/mL hydrocortisone, 20 ng/mL recombinant human EGF, 1 nM cholera toxin, 20 mg/L adenine, 140 µg/mL BPE, 0.1% insulin-transferrin-sodium selenite-supplement (Sigma, I1884), 4 mM glutamine, 5% fetal bovine serum, and 1% antibiotics/antimycotics. OE33 cells (esophageal adenocarcinoma) were cultured in RPMI media with 10% FBS and 1% antibiotics/antimycotics.

3.2.2 Phage selection

Peptide sequences with binding specificity for high grade dysplasia were isolated using phage display. Three separate biopannings referred to as the B, C, and D pan were completed in parallel each including a phage selection step against CP-B, CP-C, and CP-D dysplastic cell lines, respectively (**Figure 3.1**). CP-B, CP-C, and CP-D cells were grown to 70-80% confluency and before each pan incubated for two hours in supplement-free RPMI media at 37°C for receptor clearance. Cells were detached using PBS-based enzyme-free cell dissociation buffer (Invitrogen, 13151-014) and resuspended in blocking

buffer (1% BSA in PBS) for 30 minutes at 4°C. 1 x 10^6 cells were incubated with 2E11 plaque forming units (pfu) of phage from Ph.D-12 and Ph.D-C7C libraries (New England Biolabs) for 1 hr at 4°C in 200 µL blocking buffer under agitation. Cells were then washed three times with a 0.1% Tween-20 PBS solution to remove unbound or weakly bound phage. Remaining phage were eluted from cells by incubating the cells in 1 mL glycine HCl solution (pH 2.2) for 8 minutes

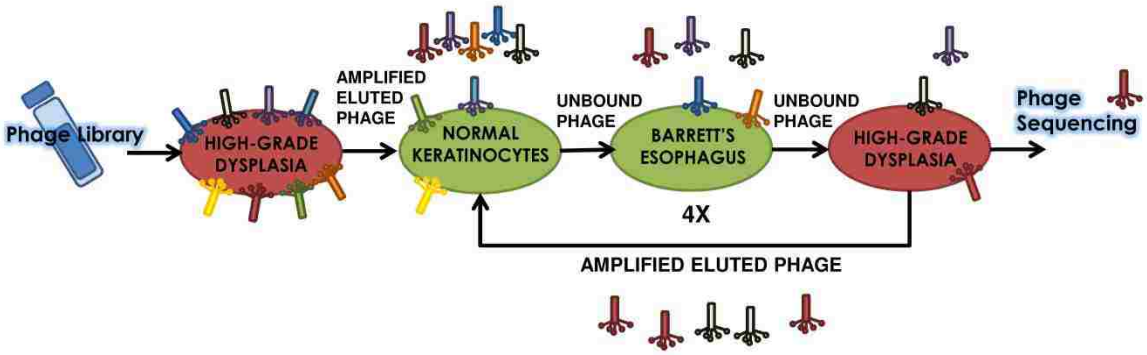

Scheme 3.1 Subtractive whole cell panning strategy for isolation of an HGD-binding peptide.

and subsequently neutralizing the solution with 150 µL 1M Tris buffer (pH 9.1). Cells were spun down at 300 rcf for 5 min and the supernatant collected for subsequent pans.

After this initial selection step, the collected phage were amplified and tittered in preparation for iterative rounds of subtraction and selection pans. 2 x 10^{11} pfu of phage in 200 uL blocking buffer were incubated at room temperature for 30 minutes with 5 x 10^5 EPC2 cells prepared using the same methods of receptor clearance (in KSFM media without supplements), detachment, and blocking as previously described. The cells were spun down at 300 rcf for 5 min and the supernatant containing unbound phage was then incubated at room temperature for 30 minutes with 5 x 10^5 CP-A cells prepared in the same manner as the CP cell lines in the initial selection step. The cells were spun down and the supernatant was then incubated for 1 hr at

4°C with 1 x 10^6 CP-B, CP-C, or CP-D cells prepared as previously described. Cells were washed 3 times with 0.1% Tween 20 in PBS to remove unbound or weakly bound phage, and bound phage were eluted from cells by incubating the cells in 1 mL glycine HCl solution for 8 min at room temperature with subsequent solution neutralization using 150 µL 1M Tris buffer (pH 9.1). Cells were spun down and the supernatant was collected, amplified, and tittered. Three additional iterations of EPC2 subtraction, CP-A subtraction, and CP-B, CP-C, or CP-D selection was completed with minor modifications for increased stringency. 1 x 10^6 EPC2 and CP-A cells were used for subtractive pans for 1 hr. For the wash step, the wash buffer contained 0.3%, 0.5%, and 0.5% Tween 20 in PBS for rounds 2, 3, and 4, respectively.

DNA of phage clones from each of the three separate biopannings were prepared after rounds 3 and 4 using methods described in the New England Biolabs Ph.D. Phage Display Libraries Instruction Manual. 15-µL DNA samples containing 350 µg DNA and 25 pmol primer in DI water were submitted to Genewiz for sequencing.

3.2.3 Phage binding studies

Phage clones of interest were identified after sequencing and their binding to EPC2, CP-A, CP-B, CP-C, and CP-D cells were quantified through bound phage counts to determine if isolated phage bound preferentially to the dysplastic cell lines. Cells were detached using PBS-based enzyme-free dissociation buffer and blocked in blocking buffer for 30 minutes at 4°C. In binding study 1, 2 x 10^{11} pfu of isolated phage were incubated with 8 x 10^5 cells for 1 hr at 4°C. Insertless phage, M13KE, was used as a negative control. In binding study 2, due to limitations on number of cells in culture, 1 x 10^{11} pfu of isolated phage or insertless phage were incubated with 4 x 10^5 cells for 1 hr at 4°C. Cells were then washed three times with 0.2% Tween-20. Bound phage were eluted from cells by incubating the cells in 1 mL glycine HCl solution (pH 2.2) for 8 minutes and subsequently neutralizing the

solution with 150 µL 1M Tris buffer (pH 9.1). Cells were spun down at 300 rcf for 5 minutes and the supernatant was collected and titered.

3.2.4 BLAST Search

The Basic Local Alignment Search Tool (BLAST) was used to identify proteins with significant homology to isolated peptide sequences to determine the corresponding cell surface targets.

3.2.5 Peptide synthesis

The candidate peptides were synthesized on a solid support using standard Fmoc/t-Bu chemistry on an automated PS3 peptide synthesizer. Peptides were synthesized on a cysteine-terminated Wang resin to add a thiol residue at the C-terminus for fluorophore conjugation. A lysine was added after the cysteine for increased peptide solubility followed by the GGGS amino acid sequence which fuses the peptides to the pIII coat protein on M13 bacteriophage. The resulting sequences are the following: B22 (DEWWTPVWNHRNGGGSKC) and scrambled peptide control scB22 (WPNNRWDVEHWTGGGSKC). Peptides were cleaved from the solid support using a cocktail of TFA/DCM/TIPS/EDC (92.5:2.5:2.5:2.5, v/v/v/v). Cleaved peptides were precipitated in cold either, dissolved in methanol, and reprecipitated in cold either. Peptide products were then confirmed using MALDI MS and purified to at least 95% purity using HPLC.

For binding studies, fluorescein-5-maleimide (ThermoScientific, 62245) was conjugated to peptides via the C-terminus cysteine in pH 7.0 phosphate buffered saline at a molar ratio of 5:1 fluorophore to peptide. The reaction solution was desalted using C18 Hypersep SPE columns (ThermoScientific, 60108-701) and purified using HPLC.

3.2.6 Measurement of binding affinity

2 x 10^5 CP-B cells were blocked with 1% BSA in PBS at 4˚C for 30 min. After blocking, cells were incubated with 0.001-1 mM B22-fluorescein at 4˚C for 30 min. Cells were washed three times using chilled blocking buffer and resuspended in 500 µL blocking buffer. Fluorescence intensity from bound peptides was measured using a MACSQuant Analyzer.

3.3 Results

3.3.1 Identification of B family peptides and lone sequences CD47 and D22

Isolated phage were sequenced after the third and fourth round of subtraction and selection (**Table 1**). A total of 9 sequences (6 sequences after the third round and 3 sequences after the fourth round) containing a portion or the entire B motif

$$\mathbf{X_1WX_2PVX_3},$$

where X_1 is a nonpolar and/or aromatic residue (tryptophan, phenylalanine, methionine, tyrosine), X_2 is a polar or charged residue (threonine, serine, asparagine, or glutamic acid), and X_3 is a tryptophan or phenylalanine, were isolated from the B pan. After round 3 of subtraction and selection, 34% (14 out of 41) of sequenced phage expressed peptide sequences with the B motif. An additional round of subtraction-selection resulted in an enrichment of motif B to 83% (25 out of 30) of sequenced phage. After the fourth round of panning, there were two consensus sequences B22 and B30 which occurred in 53% (16 out of 30) and 13% (4 out of 30) of sequenced phage, respectively, and one repeat sequence, B63.

Two other consensus sequences were isolated in the C and D pans. CD47, a sequence appearing in 22% (4 out of 18) of sequenced phage from the C pan appeared one time in sequenced phage from the D pan. This overlap sequence has the same first five residues as one of the B pan sequences, B15.

The final consensus sequence, D22, occurred in 75% (15 out of 20) of sequenced phage in the D pan. This sequence shared no homology with B sequences or CD47.

3.3.2 Phage binding studies

Binding studies were conducted *in vitro* after each round of sequencing. In the first study, binding of phage expressing the B22 consensus sequence and the repeat sequences, B28 and B34, was evaluated. All three sequences demonstrated preferential binding to dysplastic cell lines CP-B and CP-C over the EPC2 and CP-A cell lines. Phage demonstrated 3-5-fold and 2-6-fold greater binding to the CP-B cells than to EPC2 cells and CP-A cells, respectively (**Figure 1**). 22-44-fold and 10-67-fold greater number of phage were bound to CP-C cells than to EPC2 cells and CP-A

Table 1 Peptide sequences of interest isolated after panning cycles 3 and 4

Clone No.	Sequence	Occurrence After Panning Cycle Round 3	Occurrence After Panning Cycle Round 4
B22	DEWWTPVWNHRN	17% (7/41)	53% (16/30)
B28	NLDSAYWSPVWN	4.9% (2/41)	3.3% (1/30)
B30	EMWNPVWVTPQM	2.4% (1/41)	13% (4/30)
B63	IPWPYWEPVWIT	*No occurrence*	6.7% (2/30)
B64	SPQYWSPVWYSN	*No occurrence*	3.3% (1/30)
B66	QQFWTPVFSNRE	*No occurrence*	3.3% (1/30)
B34	TTGPQLFWSPVW	4.9% (2/41)	*No occurrence*
B15	**NDVWY**PVWLNVG	2.4% (1/41)	*No occurrence*
B17	NFQPGFWSPVWA	2.4% (1/41)	*No occurrence*
CD47	**NDVWY**DAEDILR	C: 5.9% (2/34) D: *No occurrence*	C: 22% (4/18) D: 5.0% (1/20)
D22	DYPLHHGKTPRL	5.3% (1/19)	75% (15/20)

cells, respectively (**Figure 3.1**). No preferential binding to the CP-D cells was observed.

Following the fourth round of subtraction-selection, three additional sequences with the B motif appeared as well as consensus sequences, CD47 and D22. A second phage binding study was completed to determine if the presence of the motif contributed to preferential binding of phage to dysplastic cell lines and to evaluate the new consensus sequences (**Figure 3.2**). All sequences with the B motif, including sequences only occurring once, were evaluated. Previously evaluated B22, B28, and B34 were not included. Consistent with B22, B28, and B34 binding, 5 of 6 B sequences showed preferential binding to CP-B and CP-C cells with 2-10-fold greater bound phage counts than CP-A cells and no preferential binding to CP-D cells. The exception, B15, bound CP-A cells to an equal or greater extent compared to dysplastic cells as did CD47. D22 had 4-fold and 2.5-fold greater number of bound phage in CP-C and CP-D cells, respectively, than CP-A cells.

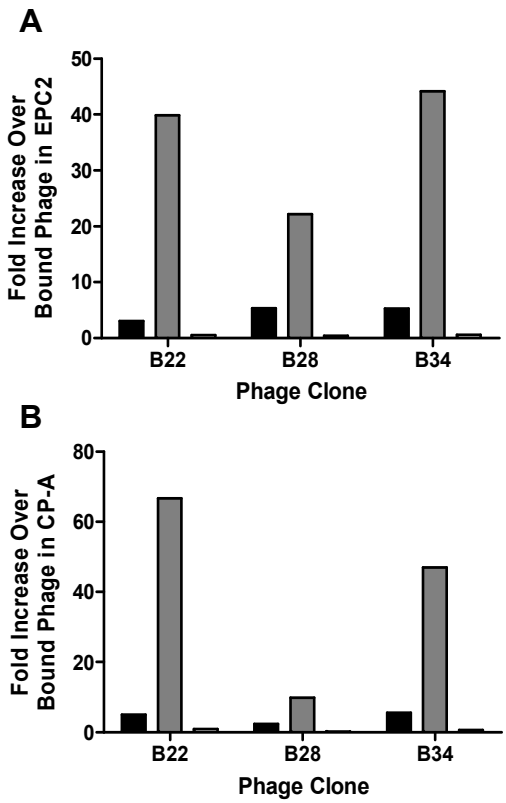

Figure 3.1 Phage binding study I results. Binding of candidate phage to dysplastic cell lines CP-B (black), CP-C (grey), and CP-D (white) was evaluated through phage counts. (A) The ratios of bound phage in dysplastic cell lines to bound phage in EPC2 cells indicate preferential binding of B22, B28, and B34 phage to CP-B and CP-C cells. (B) The ratios of bound phage in dysplastic cell lines to bound phage in CP-A cells indicate preferential binding of B22, B28, and B34 to CP-B and CP-C cells. No preferential binding of candidate phage to CP-D cells was observed.

3.3.3 BLAST results

A BLAST search was completed to find proteins with homology to peptide sequences expressed by phage preferentially binding to dysplastic cells (i.e. B sequences except B15, CD47) to identify the corresponding cell surface targets. BLAST results were narrowed down to proteins containing the B motif in its entirety since phage binding study results suggest the motif is responsible for preferential binding to dysplastic cells (**Supplementary Data Table 1**). Most matches were proteins expressed by bacteria with a healthy representation of bacteria in the phyla Bacteroidetes, Actinobacteria, Proteobacteria, and Firmicutes. Of particular interest was the homology of B22 to IPT/TIG domain protein and ß-glucanase produced by *Bacteroides ovatus* and *Bacteroides sp. D20*, respectively. Both bacterial species have been previously found in the gastrointestinal tract and are associated with inflammatory conditions of the intestine such as inflammatory bowel disease (IBD) and Crohn's disease. Other interesting matches include homology of B63 to bacterial glycoside hydrolase family protein and the lone sequence D22 to bacterial glycogen branching protein and 1,4-alpha-glucan branching protein. More specifically, the first seven residues of D22 (DYPLHHG) is a conserved sequence in the glycogen branching protein and 1,4-alpha-glucan branching protein from two different bacteria. Including the aforementioned ß-glucanase from *Bacteroides sp. D20*, all of these enzymes mediate the breaking down or building up of polysaccharides. Finally, B34 demonstrates homology to *Triticum monococcum* or einkorn wheat, which shares a common genus with *Triticum vulgare,* the same wheat species that produces the lectin used by Bird-Lieberman et al. for negative staining of HGD.

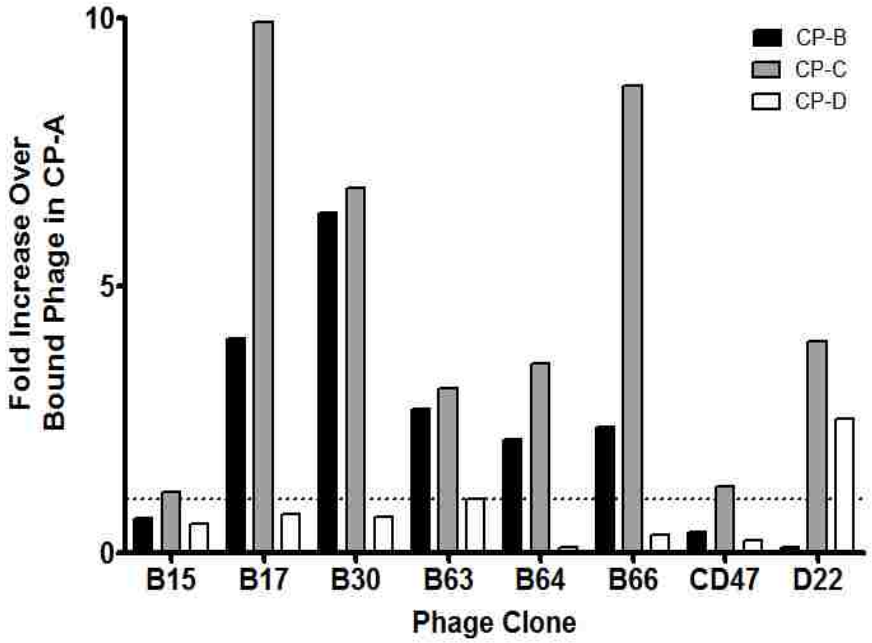

Figure 3.2 Phage binding study II results. Binding of B phage clones (with the exception of previously-evaluated B22, B28, and B34), CD47, and D22 were evaluated in dysplastic cell lines CP-B, CP-C, and CP-D and non-dysplastic Barrett's esophagus cell line CP-A. The ratio of bound phage in dysplastic cell lines to bound phage in CP-A cells demonstrates preferential binding of B phage (with the exception of B15) to CP-B and CP-C cells and D22 phage to CP-C and CP-D cells. CD47 showed no preferential binding to any dysplastic cell line.

3.3.4 Binding affinity of B22

The dysplastic cell line, CP-B, was incubated with a range of B22-fluorescein concentrations to quantify binding affinity. However, even at 1 mM concentration, the Kd curve did not reach binding saturation (**Fig. 3.3**).

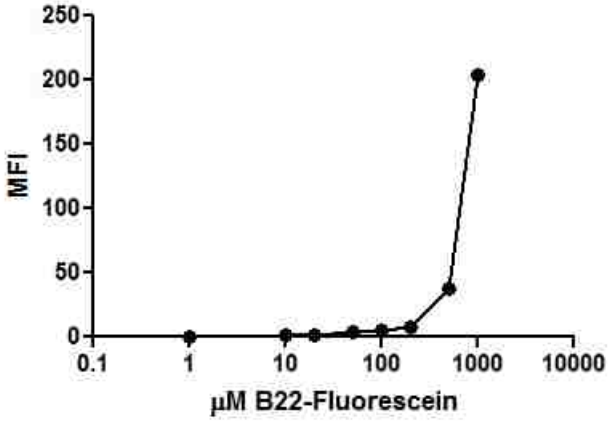

Figure 3.3 Kd curve for B22-fluorescein. CP-B cells were incubated with 0.001-1 mM B22-fluorescein. However, no binding saturation was observed.

3.4 Discussion

In vitro phage display was used to isolate HGD-binding peptides. Since biochemical alterations in EAC are not necessarily observed in HGD to the same extent, selection against dysplastic cell lines (versus EAC cell lines) was used to find peptides that would bind cell surface targets with the greatest alterations during the progression from BE to BE with HGD. Subtractive pans against normal esophageal keratinocytes (cells making up the majority of the epithelium) and cells from non-dypslastic BE were completed to increase specificity for dysplasia. Three independent pans B, C, and D were completed in parallel each with a selection step against dysplastic cell lines CP-B, CP-C, and CP-D, respectively. These hTERT-immortalized cell lines were derived from biopsy specimen from three different patients[10] and, thus, represent a sampling size of three to account for likely heterogeneity among patients.

Of the phage that were isolated, phage expressing B family peptides and the lone sequence D22 were shown to preferentially bind to two of the three dysplastic cell lines. Evaluation of phage binding across multiple dysplastic cell lines allowed for validation of cell surface targets. Surprisingly, peptides isolated in the B pan bound to CP-C cells to a greater extent than to CP-B cells. Regardless, specific binding in two of the three cell lines demonstrates

relevance of the B motif target to a subset of patients with HGD. 5 of 9 B sequences appeared only once out of the total number of sequenced phage. However, presence of the B motif seems to be a strong prerequisite for preferential binding to CP-B and CP-C cells irrespective of motif location in the whole peptide sequence. The exception, B15, showed similar or less binding in dysplastic cells compared to binding in CP-A cells, very much like CD47. B15 and CD47 share the same first 5 residues, NDVWY, and it is likely this sequence binds to CP-A cells negating any preferential binding that the B motif in B15 would have conferred. In contrast to B phage, D22 bound preferentially to CP-C and CP-D cells with no preferential binding in CP-B cells. These differences indicate B family peptides and D22 bind to two different targets. Similarly, binding of D22 to two cell lines demonstrates relevance of the D22 target as a possible biomarker for a subset of patients with HGD.

The ability to target two biomarkers presents the possibility of a two-colored system for HGD imaging in which B22 peptides are fluorescently labeled with one color fluorophore and D22 peptides are fluorescently labeled with a second color fluorophore. The benefits of such a system include the following: 1) the heterogeneous nature of cancer across patients may result in the upregulation of a fraction of possible biomarkers, in which case, imaging of multiple biomarkers would increase the chances of HGD detection (i.e. increased sensitivity) and 2) areas staining positive for two biomarkers provide stronger motivation for biopsy than areas staining positive for one biomarker (i.e. increased specificity resulting in the need for fewer damaging biopsies).

Homology of B family peptides and D22 peptide to domains of polysaccharide-processing enzymes suggests these peptides bind cell-surface glycans. Glycans, present in glycoproteins and glycolipids, represent a highly probable class of targets and is consistent with studies from Bird-Lieberman showing increased gene expression of pathways regulating the biosynthesis

and degradation of glycans during the metaplasia-dysplasia-adenocarcinoma sequence.[8] A Kd curve generated for the B22 peptide did not reach binding saturation within the 0.001-1 mM concentration range, suggesting that B22 binds with low affinity to the dysplastic cell line, CP-B. Proteins that bind carbohydrates (i.e. lectins) generally have binding affinities from 1-10 μM for complex glycans. However, lectins binding monosaccharides bind with millimolar affinity. Therefore, it is likely that avidity effects contributed to preferential binding of B22 phage to dysplastic cells.

In a broader context, the bacterial origins of homologous sequences could suggest a link between the identified HGD-binding motifs and bacterial colonization in the distal esophagus under diseased states. Lectins represent a class of adhesins, ligands on the surfaces of bacteria which bind to receptors on host surfaces to promote bacterial adhesion and subsequent colonizaton. Adhesin-receptor interactions have been known to contribute to tissue tropism of bacteria [11] Recent studies have shown that under diseased states (i.e. esophagitis, BE), the microbiome in the distal esophagus shifts from a predominantly gram-positive population to one with a greater abundance of anaerobes/microaerophiles/gram-negative bacteria[12] and changes in glycan expression could very well play a role in these changes.

3.5 Conclusions

The peptides isolated for targeting HGD demonstrated preferential binding to dysplastic cell lines when displayed on bacteriophage. However, binding affinity was low for the B22 peptide alone, suggesting that multivalent display is needed to improve binding affinity.

3.6 Acknowledgements

This work is supported by NIH EB007636 and NIH NCI CA138312.

3.7 Supplementary Data

Supplementary Data Table 1. BLAST Results for sequences binding preferentially to dysplastic cell lines.

Phage Clone No.	Phylum	Description	Query vs Subject Sequences
B22	Bacteroidetes	hypothetical protein HMPREF1070_02440 [Bacteroides ovatus CL03T12C18]	Query 2 EWWTP-VWNH 10 Sbjct 237 EWWTPAVWNQ 246
	Bacteroidetes	putative IPT/TIG domain protein [Bacteroides sp. 3_1_23]	Query 2 EWWTP-VWNH 10 Sbjct 237 EWWTPAVWNQ 246
	Bacteroidetes	**beta-glucanase** [Bacteroides sp. D20]	Query 1 DE---WWTPVW 8 Sbjct 189 DEKYRKWWTPVW 200
B28	Firmicutes	octaprenyl-diphosphate synthase [Thermacetogenium phaeum DSM 12270]	Query 4 SAYWSPVWN 12 Sbjct 39 SAYWSPVWD 47
B34	Streptophyta	TmCBF7 [Triticum monococcum]	Query 6 LFWSPVW 12 Sbjct 244 LFWSPVW 250
	Streptophyta	predicted protein [Hordeum vulgare subsp. vulgare]	Query 6 LFWSPVW 12 Sbjct 244 LFWSPVW 250
B63	Proteobacteria	Molybdenum transport system permease protein modB [Marinobacter sp. BSs20148]	Query 5 YWEPVWIT 12 Sbjct 5 YWEPVWLT 12
	Ascomycota	unnamed protein product [Aspergillus oryzae RIB40]	Query 5 YWEPVWIT 12 Sbjct 353 YWEPVWTT 360
	Ascomycota	conserved hypothetical protein [Aspergillus flavus NRRL3357]	Query 5 YWEPVWIT 12 Sbjct 331 YWEPVWTT 338
	Proteobacteria	Rec2-related protein [Vibrio shilonii AK1]	Query 5 YWEPVWI 11 Sbjct 576 YWEPVWV 582
	Bacteroidetes	**Glycoside hydrolase family protein** [Nitritalea halalkaliphila LW7]	Query 5 YWEPVW 10 Sbjct 89 YWEPVW 94
	Ascomycota	unnamed protein product [Aspergillus niger]	Query 5 YWEPVW 10 Sbjct 86 YWEPVW 91
	Ascomycota	conserved hypothetical protein	Query 5 YWEPVW 10

		[Aspergillus fumigatus A1163]	Sbjct 275 YWEPVW 280
	Ascomycota	conserved hypothetical protein	Query 5 YWEPVW 10
		[Aspergillus clavatus NRRL 1]	Sbjct 328 YWEPVW 333
	Ascomycota	hypothetical protein NFIA_089690	Query 5 YWEPVW 10
		[Neosartorya fischeri NRRL 181]	Sbjct 331 YWEPVW 336
	Ascomycota	similar to An02g00660	Query 5 YWEPVW 10
		[Aspergillus kawachii IFO 4308]	Sbjct 360 YWEPVW 365
	Ascomycota	hypothetical protein ANI_1_2176024	Query 5 YWEPVW 10
		[Aspergillus niger CBS 513.88]	Sbjct 360 YWEPVW 365
B64	Proteobacteria	exodeoxyribonuclease V subunit beta	Query 4 YWSPVWY 10
		[Actinobacillus succinogenes 130Z]	Sbjct 862 YWNPVWY 868
	Actinobacteria	Signal transduction histidine kinase	Query 4 YWSPVWYS 11
		[Bifidobacterium animalis subsp. animalis ATCC 25527]	Sbjct 54 YWSPVWCS 61
	Heterokontaphyta	hypothetical protein PITG_02140	Query 4 YWSPVW 9
		[Phytophthora infestans T30-4]	Sbjct 54 YWSPVW 59
	Firmicutes	octaprenyl-diphosphate synthase	Query 4 YWSPVW 9
		[Thermacetogenium phaeum DSM 12270]	Sbjct 41 YWSPVW 46
	Methanomicrobia	YcaO-domain protein	Query 4 YWSPVW 9
		[Methanoplanus limicola DSM 2279]	Sbjct 137 YWSPVW 142
B66	Ascomycota	predicted protein	Query 3 FWTPVFS 9
		[Leptosphaeria maculans JN3]	Sbjct 182 FWTPVFS 188
D22	Actinobacteria	hypothetical protein STRTUCAR8_04552	Query 1 DYPLHHG 7
		[Streptomyces turgidiscabies Car8]	Sbjct 18 DYPLHHG 24
	Actinobacteria	hypothetical protein SBI_06116	Query 1 DYPLHHG 7
		[Streptomyces bingchenggensis BCW-1]	Sbjct 18 DYPLHHG 24
	Actinobacteria	hypothetical protein SRIM_23266	Query 1 DYPLHHG 7
		[Streptomyces rimosus subsp. rimosus ATCC 10970]	Sbjct 14 DYPLHHG 20
	Actinobacteria	hypothetical protein STRIP9103_05913	Query 1 DYPLHHG 7
		[Streptomyces ipomoeae 91-03]	Sbjct 21 DYPLHHG 27
	Actinobacteria	conserved hypothetical protein	Query 1 DYPLHHG 7

	[Streptomyces sviceus ATCC 29083]	Sbjct 25 DYPLHHG 31
Actinobacteria	hypothetical protein H340_08138	Query 1 DYPLHHG 7
	[Streptomyces mobaraensis NBRC 13819 = DSM 40847]	Sbjct 10 DYPLHHG 16
Actinobacteria	conserved hypothetical protein	Query 1 DYPLHHG 7
	[Streptomyces sp. e14]	Sbjct 43 DYPLHHG 49
Actinobacteria	conserved hypothetical protein	Query 1 DYPLHHG 7
	[Streptomyces hygroscopicus ATCC 53653]	Sbjct 32 DYPLHHG 38
Actinobacteria	hypothetical protein SAV_4859	Query 1 DYPLHHG 7
	[Streptomyces avermitilis MA-4680]	Sbjct 29 DYPLHHG 35
Firmicutes	**glycogen branching protein**	Query 1 DYPLHHG 7
	[Oceanobacillus sp. Ndiop]	Sbjct 495 DYPLHHG 501
Proteobacteria	**1,4-alpha-glucan branching protein**	Query 1 DYPLHHG 7
	[Sulfuricurvum kujiense DSM 16994]	Sbjct 508 DYPLHHG 514

References

1. Chen, X. & Yang, C.S. Esophageal adenocarcinoma: a review and perspectives on the mechanism of carcinogenesis and chemoprevention. Carcinogenesis **22**, 1119-1129 (2001).
2. Ong, C.A., Lao-Sirieix, P. & Fitzgerald, R.C. Biomarkers in Barrett's esophagus and esophageal adenocarcinoma: predictors of progression and prognosis. World J Gastroenterol **16**, 5669-5681 (2010).
3. Hamilton, S.R. & Smith, R.R. The relationship between columnar epithelial dysplasia and invasive adenocarcinoma arising in Barrett's esophagus. American journal of clinical pathology **87**, 301-312 (1987).
4. Heitmiller, R.F., Redmond, M. & Hamilton, S.R. Barrett's esophagus with high-grade dysplasia. An indication for prophylactic esophagectomy. Annals of surgery **224**, 66-71 (1996).
5. Montgomery, E., et al. Dysplasia as a predictive marker for invasive carcinoma in Barrett esophagus: A follow-up study based on 138 cases from a diagnostic variability study. Hum. Pathol. **32**, 379-388 (2001).
6. Reid, B.J., Levine, D.S., Longton, G., Blount, P.L. & Rabinovitch, P.S. Predictors of progression to cancer in Barrett's esophagus: baseline histology and flow cytometry identify low- and high-risk patient subsets. Am J Gastroenterol **95**, 1669-1676 (2000).
7. Kariv, R., et al. The Seattle protocol does not more reliably predict the detection of cancer at the time of esophagectomy than a less intensive surveillance protocol. Clinical gastroenterology and hepatology : the official clinical practice journal of the American Gastroenterological Association **7**, 653-658; quiz 606 (2009).
8. Bird-Lieberman, E.L., et al. Molecualr imaging using fluorescent lectins permits rapid endoscopic identification of dysplasia in Barrett's esophagus. Nature Medicine **18**, 315-321 (2012).
9. Li, M., et al. Affinity peptide for targeted detection of dysplasia in Barrett's esophagus. Gastroenterology **139**, 1472-1480 (2010).
10. Palanca-Wessels, M.C., et al. Genetic analysis of long-term Barrett's esophagus epithelial cultures exhibiting cytogenetic and ploidy abnormalities. Gastroenterology **114**, 295-304 (1998).
11. Beachey, E.H. Bacterial adherence: adhesin-receptor interactions mediating the attachment of bacteria to mucosal surface. J Infect Dis **143**, 325-345 (1981).
12. Yang, L., et al. Inflammation and intestinal metaplasia of the distal esophagus are associated with alterations in the microbiome. Gastroenterology **137**, 588-597 (2009).
13. Cummings RD, Etzler ME. Antibodies and Lectins in Glycan Analysis. *Essentials Glycobiol* 2009.

PART II

DEVELOPMENT OF INTRAVENOUSLY-ADMINISTERED POLYMERS FOR MODULATING FIBRIN PROPERTIES AND INDUCING HEMOSTASIS

EXECUTIVE SUMMARY

The formation of a robust clot is integral for the cessation of bleeding, or hemostasis. However, under certain conditions, such as trauma injury, mechanisms for clot formation are absent, insufficient, or defective. Therefore, medical intervention is needed to halt bleeding. In cases of internal bleeding, surgical intervention is supplemented with mass transfusions (MTs) of blood products or recombinant coagulation factors. However, limitations associated with the use of either such as limited efficacy, immunogenicity, insufficient supply, and short shelf-life prevent them from being viable long-term solutions. Therefore, there are ongoing efforts to develop synthetic blood components to be used as intravenous hemostats. Polymer engineering is a promising avenue for the development of synthetic blood components. The ability to synthesize scalable materials with fine-tuned properties for biocompatibility, targeted delivery, and specific function has already enabled the development of the first generation of synthetic platelets which have demonstrated efficacy in inducing hemostasis in *in vivo* injury models. This work focuses on the construction of a FXIII polymer mimic. FXIII is a transglutaminase which crosslinks fibrin to induce the formation of a stable clot. Recent evidence has shown that trauma patients produce clots that are 40% weaker than control clots. Reduced clot strength has been shown to be an independent risk factor for 30-mortality. Furthermore, hyperfibrinolysis is a common phenomenon in trauma patients and contributes to the weakened state of clots. Fibrin matrix formation and subsequent FXIII-induced crosslinking is an important contributor to clot strength. Therefore, a synthetic FXIII polymer mimic is expected to induce stable clot formation through fibrin crosslinking and by delaying fibrinolysis through integration of lysis-resistant polymers into the fibrin network.

Specific Aims

Specific Aim 1. Synthesize and characterize linear polymers with multivalent display of fibrin-binding peptides.

Specific Aim 2. Evaluate effect of fibrin-binding polymers on coagulation *in vitro* in pure fibrin gels, plasma, and whole blood.

Specific Aim 3. Evaluate the hemostatic capability of fibrin-binding polymers *in vivo* in a rat model of femoral artery injury.

Specific aims 1-3 are addressed in Chapter 2. Chapter 3 focuses on the comparison between the resulting polymer hemostats (PolySTATs) and currently-used hemostatic agents. Chapter 4 investigates the use of PolySTAT for resolving bleeding in hemophilia A. Chapter 5 contains ideas for future hemostatic agents.

Published chapters.

Chan LW, White NJ, Pun SH. Synthetic Strategies for Engineering Intravenous Hemostats. *Bioconjug Chem* 2015; Epub ahead of print. [Chapter 1]

Chan LW, Wang X, Wei H, Pozzo LD, White NJ, Pun SH. A Synthetic Fibrin-Crosslinking Polymer for Modulating Clot Properties and Inducing Hemostasis. *Sci Transl Med* 2015; **7**: 277ra29. [Chapter 2]

Chapters 3 and 4 are manuscripts in preparation.

Chapter 1

SYNTHETIC STRATEGIES FOR ENGINEERING INTRAVENOUS HEMOSTATS

Leslie W. Chan, Nathan J. White, Suzie H. Pun

Abstract

While there are currently many well-established topical hemostatic agents for field administration, there are still limited tools to staunch bleeding at less accessible injury sites. Current clinical methods of restoring hemostasis after large volume blood loss include platelet and clotting factor transfusion, which have respective drawbacks of short shelf-life and risk of viral transmission. Therefore, synthetic hemostatic agents that can be delivered intravenously and encourage stable clot formation after localizing to sites of vascular injury are particularly appealing. In the past three decades, platelet substitutes have been prepared using drug delivery vehicles such as liposomes and PLGA nanoparticles that have been modified to mimic platelet properties. Additionally, structural considerations such as particle size, shape, and flexibility have been addressed in a number of reports. Since platelets are the first responders after vascular injury, platelet substitutes represent an important class of intravenous hemostats under development. More recently, materials affecting fibrin formation have been introduced to induce faster or more stable blood clot formation through fibrin crosslinking. Fibrin represents a major structural component in the final blood clot, and a fibrin-based hemostatic mechanism acting downstream of initial platelet plug formation may be a safer alternative to platelets to avoid undesired thrombotic activity. This review explores intravenous hemostats under development and strategies to optimize their clotting activity.

This chapter was published in *Bioconjugate Chemistry* [Epub ahead of print].

1.1 Introduction

A blood clot is a biopolymer-colloid composite that prevents bleeding from damaged vasculature. The colloid component consists of activated platelets bound to subendothelial proteins that are exposed after vascular injury (i.e. collagen, von Willebrand factor) and aggregated to form a platelet plug at the site of injury (Figure 1). The biopolymer component is subsequently formed by the coagulation cascade. Locally-activated thrombin enzyme cleaves circulating fibrinogen to form fibrin monomers. Fibrin monomers then self-polymerize into fibers to form a viscoelastic biopolymer network interspersed through the platelet plug. For small injuries, this composite is sufficient for maintaining *hemostasis*, the prevention of blood loss from damaged blood vessels. However, for more severe bleeding from traumatic injury, surgery, or bleeding disorders, hemostatic agents that augment the natural clotting process or physically seal the wound itself are needed to staunch bleeding. Hemostats for field administration after traumatic injury are particularly important as hemorrhage is responsible for 33-56% of prehospital deaths[1] and 90% of preventable military battlefield casualties[2], and immediate intervention is believed to be key in reducing early hemorrhage-related mortality and morbidity.

There are many well-established clinically-used topical hemostatic agents. These include gel sealants derived from a mixture of biological materials (i.e. human fibrinogen and thrombin, bovine collagen, and human platelets) and absorbent hemostatic dressings manufactured with fibrin, chitin/chitosan, or mineral zeolites used to increase concentration of clotting factors, platelets, and erythrocytes at the site of injury.[3] Topical hemostats are limited to treating visible and accessible injuries. Transfusion of blood products (i.e. fresh frozen plasma, platelets) and recombinant clotting factors is used to restore clotting function in those who are coagulopathic after large volume blood loss and are the only current intravenous hemostats in use.[4] However, biological agents have many limitations such as risk of immunogenicity and

viral transmission, restrictive storage conditions, short shelf-life, and involved manufacturing processes. In contrast, synthetic polymers and polymeric nanoparticles have tunable physical and chemical properties and, in general, have more straightforward manufacturing processes and longer shelf-lives compared to biological products. Therefore, current efforts are underway to develop synthetic hemostats that can be administered systemically for quick resolution of bleeding at inaccessible injury sites.

Blood clot formation is heavily mediated by specific protein-protein interactions. These interactions are responsible for platelet adhesion at injury sites, platelet aggregation, and fibrin polymerization. Strategies for inducing hemostasis have therefore predominantly focused on leveraging these interactions to accelerate and stabilize the assembly of non-covalent bonds between clot components. To do so, artificial platelets and fibrin-modulating polymers and particles have been designed with multivalent display of binding motifs to promote clot aggregation at the injured blood vessel. Furthermore, in the case of synthetic platelet substitutes, the shape and flexibility of particles on which these binding motifs are displayed have proven important in optimizing particle rolling velocities and contact area with the tissue surface, two contributing factors for platelet adhesion.[5] The design of intravenous hemostats with site-specific activity has relied upon knowledge and strategies developed by the systemic drug delivery field. This review discusses the materials and engineering design considerations used in synthetic intravenous hemostats under pre-clinical development.

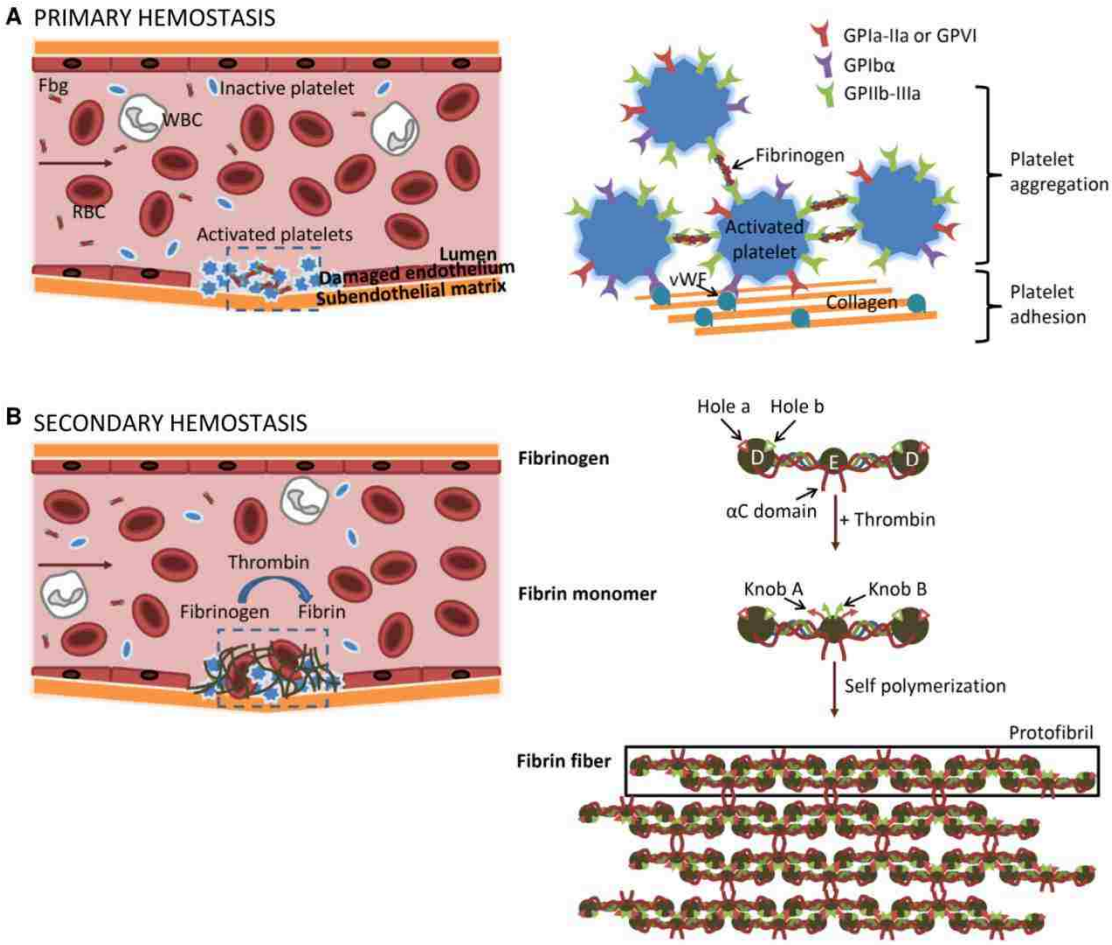

Figure 1.1. Schematic of the clotting process showing initial platelet plug formation during primary hemostasis (A) followed by fibrin formation during secondary hemostasis (B). During primary hemostasis, circulating platelets adhere to the subendothelial matrix through binding of the platelet receptors GPIbα and GPIa-IIa/GPVI to von Willebrand Factor (vWF) and collagen, respectively. Upon platelet activation, GPIIb-IIIa goes through a conformational change which enables it to bind fibrinogen. Platelet aggregation is induced by multiple platelets binding the same fibrinogen molecule. During secondary hemostasis, activated thrombin enzyme cleaves the N-termini of Aα (red) and Bβ (green) polypeptide chains, revealing knob A and knob B peptide domains, respectively. Knobs A and B interact with holes a and b in the D nodules of other fibrin monomers to form half-staggered, double-stranded protofibrils. Non-specific interaction between αC domains causes lateral aggregation of protofibrils to form fibrin fibers.

1.2 Artificial platelets

1.2.1 Primary hemostasis

Platelets are anucleate cell fragments 1-3 μm in diameter formed from the cytoplasm of megakaryocytes.[6,7] During *primary hemostasis*, a platelet plug is formed at the injury site (Figure 1.1A). As the first responders after injury, platelets instigate clot formation by first marginating to the damaged endothelium, binding to proteins in the exposed subendothelial matrix, and finally aggregating after activation. The biconvex discoid shape of platelets facilitates margination towards vessel walls under blood flow.[8] Upon reaching an injured wall, platelets are captured by shear-induced binding of the platelet surface glycoprotein GPIbα to von Willebrand factor (vWF) immobilized on the exposed subendothelial matrix. Reversible tethering by vWF allows platelets to spread and roll along the tissue surface for subsequent shear-independent binding of GPIa-IIa and GPVI to collagen, which stabilizes platelet adhesion.[5,9,10] Platelets are activated by collagen-binding and agonists such as adenosine diphosphate (ADP) and thrombin. During activation, platelets take on a stellate shape and the surface integrin GPIIb-IIIa undergoes a conformational change which enables it to bind to any of three peptide domains in fibrinogen (i.e. RGD motifs: RGDF, RGDS; H12 sequence: HHLGGAKQAGDV).[11–13] In this "sticky" state, platelets are thus able to aggregate by binding the same fibrinogen molecule, which has a total of 6 possible platelet-binding domains due to its symmetrical structure. Additional ADP is secreted by activated platelets for further local platelet activation. The following sections discuss the design and optimization of platelet substitutes. For further reading solely on synthetic platelets, an excellent prior review is available from the Sen Gupta lab.[14]

1.2.2 Fibrinogen and RGD-peptide coated microparticles

There are approximately 80,000 GPIIb-IIIa receptors per platelet[15], and up to 40,000 fibrinogen can reportedly bind to activated platelets[16–18]. The first

platelet substitutes were designed to promote platelet aggregation through surface display of fibrinogen or RGD-containing peptide (Table 1.1).[19–22] In their constructs, Agam et al. covalently coupled fibrinogen to the surface of human platelets[19] and erythrocytes[20] by fixation with formaldehyde and showed enhanced platelet aggregation when incubated with activated platelets *in vitro* as well as restoration of normal bleeding times (i.e. time to clot) when delivered to thrombocytopenic rats (i.e. rats with low platelet counts). Untreated thrombocytopenic rats had bleeding times of 18 ± 1.5 min, whereas thrombocytopenic rats injected with fibrinogen-bearing erythrocytes had bleeding times of 4.5 ± 1.0 min, closer to the 2.5 ± 0.1 min bleeding time observed in non-thrombocytopenic rats.[20] In later work, Levi et al. proposed the use of Synthocytes™, 3.5-4.5 μm-diameter human albumin microcapsules adsorbed with fibrinogen, for treatment of severe thrombocytopenia.[22,23] In contrast to control rabbits with normal ear bleeding times of 1.7 ± 0.4 min, thrombocytopenic rabbit models had prolonged bleeding times of 21.7 ± 4.4 min. Intravenous injection of Synthocytes™ resulted in corrected bleeding times of 5.2 ± 1.7 min. While fibrinogen-functionalized materials bridge activated platelets, aggregate formation is also likely due to thrombin-induced fibrin formation. Fibrin polymerization between surfaces of modified platelets and erythrocytes would entrap platelets resulting in aggregate formation.

To avoid risk of infectious contaminants in purified fibrinogen, Coller et al. opted to functionalize erythrocytes with fibrinogen-mimetic peptides containing an RGD sequence (Ac-CGGRGDF-NH_2) synthesized using solid phase peptide synthesis.[21] This product, called thromboerythrocytes, represents one of the earliest uses of peptides in platelet engineering. Since RGD peptides are three orders of magnitude smaller than fibrinogen molecules, a significantly greater number of ligands were available for binding to GPIIb-IIIa (~0.5-1.5 x 10^6 peptides per erythrocyte) compared to fibrinogen-modified erythrocytes (~58 fibrinogen per erythrocyte)[20].

Table 1. Summary of Intravenous Hemostats and Their Mechanism of Action.

mechanism of action	class of particle or polymer	targeting ligand(s)	references
		Platelet Substitutes	
binds to subendothelial matrix	liposome	rGPIα-IIα	Nishiya et al. (2001)[31]
		rGPIbα	Takeoka et al. (2002)[5]
		vWF binding peptide (VBP): TRYLRIHPQSQVHQI Collagen binding peptide (CBP): $[GPO]_7$[a]	Ravikumar et al. (2012)[37]
binds to platelets	platelet	fixation of fibrinogen on surface using formaldehyde	Agam et al. (1983)[19]
	erythrocyte	fixation of fibrinogen on surface using formaldehyde	Agam et al. (1992)[20]
		conjugation of Ac-CGGRGDF-NH_2 via a heterobifunctional linker (thromboerythrocyte)	Coller et al. (1992)[21]
		surface adsorption of fibrinogen (Synthocytes™)	Levi et al. (1999)[22]
	albumin microparticles	rGPIα-IIα	Teramura et al. (2003)[93]
		surface display of H12 peptide HHLGGAKQAGDV	Okamura et al. (2005)[33–35] Okamura et al. (2005)[32]
	liposome	GSSSGRGDSPA and P-selectin binding peptide DAEWVDVS conjugated to liposomal membrane lipids	Modery et al. (2011)[36]
	PLL-PLGA nanoparticles	PEG arms terminated with GRGDS conjugated to NP surface	Bertram et al. (2009)[41]
binds to subendothelial matrix and platelets	liposome	extraction and incorporation of platelet membrane proteins including GPIbα, GPIIb-IIIα, and GPIV/III into the liposomal membrane (plateletsome)	Rybak et al. (1993)[29]
		surface display of VBP, CBP, and fibrinogen mimetic peptides (i.e. cyclo-CNPRGDY(OEt)RC or GRGDS)	Ravikumar et al. (2012)[38] Modery-Pawlowski et al. (2013)[39]
	PAH-BSA nanoparticles	surface display of VBP, CBP, and fibrinogen mimetic peptides	Anselmo et al. (2014)[45]
binds to and activates platelets	liposome	H12 peptide-coated liposomes encapsulating ADP	Okamura et al. (2009)[40]
		Fibrin Modulators	
cross-links fibrin	ultra-low cross-linked p(NIPAm)-AAc microgels	fibrin-binding sdFvs conjugated to the surface of ~1 μm-diameter microgel particles (platelet-like particles)	Brown et al. (2014)[91]
	poly(HEMA)	fibrin-binding peptides (Ac-Y(DGl)C(HPr)YGLCYIQGK-Am[a,b]) grafted onto a linear poly(HEMA) backbone (PolySTAT)	Chan et al. (2015)[88]

[a]O and HPr = hydroxyproline; DGl = D-glutamic acid; Ac = acetylation; Am = amidation. [b]Cyclized via C3 and C8 residues.

Interaction between surface-bound peptides and GPIIb-IIIa was confirmed after inhibitors of fibrinogen-platelet binding (i.e. free RGD peptide,

monoclonal antibody against GPIIb-IIIa) successfully knocked down platelet aggregation.

While these hemostatic agents were effective at inducing platelet aggregation, translation of these materials into clinical use is limited by possible immunogenic responses against the biologically-derived components as well as difficulties in scale-up. Therefore, more recent iterations of platelet substitutes have focused on surface modification of synthetic particle platforms such as liposomes and polymer-based nanoparticles.

1.2.3 Liposome-based platelet substitutes

Since the beginning of lipid vesicle research in the 1960s, liposomes have remained a key technology in the drug delivery field due to their ability to carry both hydrophobic and hydrophilic cargo, straight-forward surface functionalization through lipid modification, and tunable residence time in circulation.[24] Platelet-like liposomes were initially synthesized to study the function of glycoproteins in the platelet membrane and were done so by reconstituting isolated platelet membrane proteins in liposomal membranes through reverse-phase sonication or evaporation and subsequent extrusion.[25–27] Plateletsomes, liposomes containing at least 15 different platelet membrane proteins including GPIb, GPIIb-IIIa, and GPVI/III, were first evaluated in thrombocytopenic rats and shown to reduce tail bleeding times by 42% after intravenous injection.[28,29] Similar liposome-based platelet substitutes were also synthesized using recombinant glycoproteins, rGPIbα and rGPIIα-IIIα.[30,31] Following this work, platelet substitutes were functionalized with peptide ligands rather than whole proteins due to increased knowledge of peptide binding domains, the relative ease of peptide synthesis, the monodispersity of peptide products, and the controlled manner in which they can be conjugated to surfaces. Common peptide ligands employed include vWF-binding peptide (VBP: TRYLRIHPQSQVHQI) and collagen-binding peptide (CBP: $[GPO]_7$) to mimic platelet adhesion and

fibrinogen-mimetic peptides (H12 peptide and RGD peptides) and peptide binding the P-selectin surface marker for activated platelets (DAEWVDVS) to induce platelet aggregation.[32–39] More recent synthetic platelets have been engineered to induce platelet plug formation through multiple mechanisms. Heteromultivalent liposomes with dual adhesive and platelet-aggregating abilities were synthesized by conjugation of VBP, CBP, and cyclic RGD peptides to DSPE-PEG_{2000}-COOH via their N-terminus by standard carbodiimide chemistry and subsequent incorporation into liposomes at no more than 5 mol %.[38,39] In another example of liposome-based platelets with dual mechanism, Okamura et al. used H12-targeted liposomes to deliver ADP for platelet activation.[40] Mechanistic studies showed that aggregation of dye-loaded H12-liposomes with activated platelets caused release of the dye, which suggested that increased platelet aggregation in the presence of H12-(ADP)-liposome was due to an aggregation-dependent release of the platelet agonist.

1.2.4 Polymeric nanoparticles

In one of the first reported application of synthetic polymer-based platelet substitutes, the Lavik group engineered a hemostatic nanoparticle consisting of a poly(lactic-co-glycolic acid)-poly-L-lysine (PLGA-PLL) block copolymer core (170 nm diameter) conjugated to a corona of PEG arms terminated with RGD peptides.[41,42] Two PEG linkers, PEG 1500 and PEG 4600, were used to display RGD peptides, and the peptides RGD, RGDS, and GRGDS were evaluated to determine if addition of flanking residues would increase platelet aggregation. The combination of PEG 4600 linker with GRGDS peptide led to the greatest aggregation *in vitro*. When administered in a rat model of femoral artery injury at a concentration of 20 mg/mL in a 0.5-mL vehicle solution, 4600-GRGDS nanoparticles also showed the greatest hemostatic effect by halving bleeding time. Additionally, intravenous injections of nanoparticles after a rat liver trauma model reduced blood loss

after injury and significantly increased 1-hr survival to 80% compared to 40% and 47% survival of animals injected with GRGDS-absent nanoparticles and saline controls, respectively.[43]

1.2.5 Design considerations

Particle size, shape, and flexibility. Platelets are biconvex discoids rather than spheres, and it is this discoid form which facilitates platelet margination to vessel walls.[8,44] Studies by Takeoka et al. suggests that after initial attachment to surfaces, deformation of flexible membranes by hemodynamic shear flow increases the contact area between particle and tissue surfaces, providing more opportunity for reversible binding to vWF (Figure 1.2A).[5] vWF tethering of particles slow rolling velocities[5] (Figure 1.2B), and longer contact times at tissue surfaces then allow adhesion-stabilizing collagen-binding to occur. However, platelet-like particles have been predominantly synthesized using spherical particles with minimal optimization of particle membrane flexibility.[38–41] In a recent report, a layer-by-layer (LbL) method was used to synthesize platelet-like nanoparticles (PLNs) that more closely resemble the natural platelet shape (Figure 3A) in order to investigate the effect of particle size, shape, and flexibility on vessel adhesion and hemostasis.[45] Spherical polystyrene (PS) template particles were coated with alternating layers of polycationic poly(allylamine) hydrochloride (PAH) and polyanionic bovine serum albumin (BSA). After crosslinking the coating, the sacrificial PS templates were removed by dissolution, resulting in the collapse of the 4 bilayers into a flexible discoid shape. *In vitro* adhesion studies using microfluidic channels revealed first that adherence was greatest for 200 nm spherical particles compared to 1- and 2-μm spherical particles and second that adherence was greatest for flexible PLNs compared to rigid discs and spheres (PLN > disc > sphere, Figure 1.3B).[45] These results indicate that discoid shape and particle flexibility contribute to particle margination and adhesion. However, the

results of the particle size study conflict with previous studies reported by Charoenphol et al. in which binding efficiency of sialyl Lewis^a (sLe^a)-coated polystyrene spheres in endothelialized microfluidic chambers increased with increasing particle size and wall shear rate for 500 nm-5 μm sized particles (Figure 3C).[46] Computational modeling by Müller et al. also support greater margination of micron-sized particles than nano-sized particles to vessel walls.[47] This discrepancy is likely due to the fact that the former conducted flow assays with particles suspended in saline while the work by Charoenphol et al. and Müller et al. took into consideration red blood cells (RBCs). Particle margination toward the vessel wall is largely dependent on red blood cells, which occupy the center of the blood vessel during hemodynamic flow due to lift force. The area near vessel walls is therefore an RBC-free zone which is available for particles excluded from the vessel center to occupy.[48] Despite conflicting *in vitro* reports on size effects, greater hemostatic effect was observed *in vivo* for smaller-sized PLNs. In mouse tail transections, bleeding stopped more rapidly after intravenous injection of 200-nm peptide-functionalized PLNs than intravenous injections of their micron-sized or rigid counterparts (Figure 1.3D). The reduced efficacy of larger, micron-sized PLNs is likely due to shorter circulation time as larger particles are more easily sequestered by scavenger cells (i.e. macrophages) in the reticuloendothelial (RES) system.[49–51]

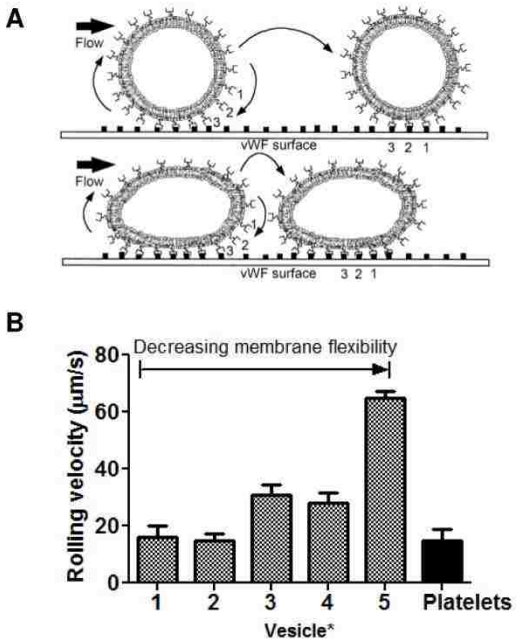

Figure 1.2. Effects of particle rigidity on rolling velocity of particles along an adhesive surface [reproduced with permission from [5]]. (A) Illustration of expected rolling mechanism of rigid vWF-targeted particles (top) versus flexible vWF-targeted particles (bottom) along a vWF-coated surface. (B) Rolling velocities of liposomes with a range of membrane flexibilities. *1, EYL/DPPE = 10/1; 2, POPC/DPPE = 10/1; 3, EYL/cholesterol/DPPE = 5/5/1; 4, POPC/cholesterol/DPPE = 5/5/1; 5, DPPC/cholesterol/DPPE = 5/5/1 (by mol).

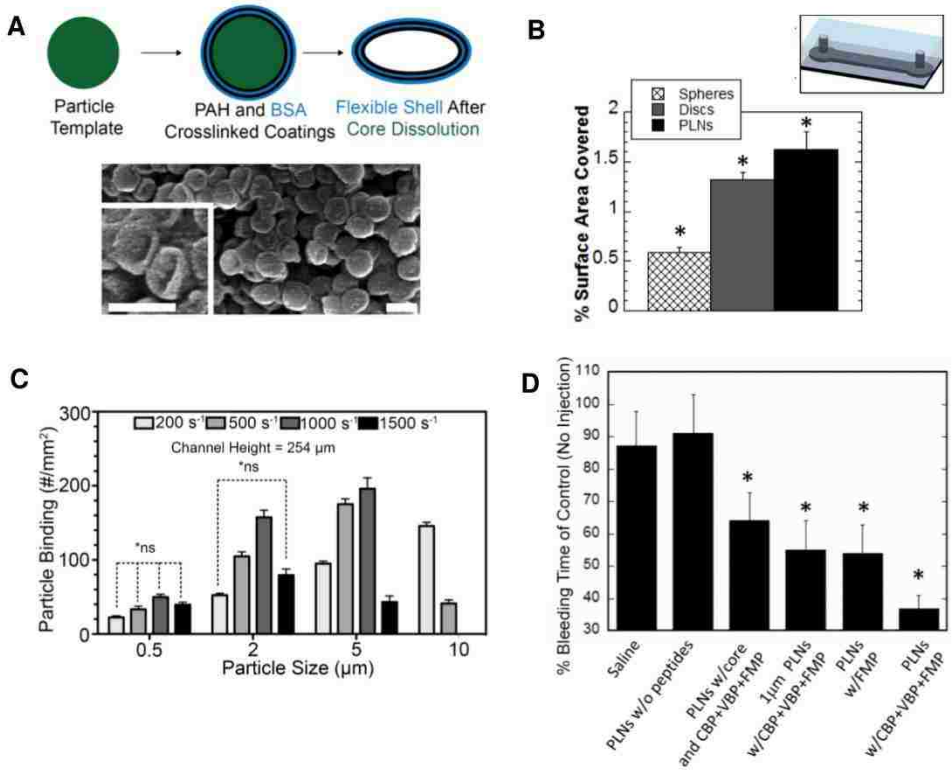

Figure 1.3. Data showing effects of particle size, shape, and flexibility on adhesion to surfaces under flow and *in vivo* hemostatic function. (**A**) Synthesis of platelet-like nanoparticle (PLN) without targeting peptides. SEM imaging confirmed collapse of the flexible PAH-BSA shell after dissolution of the polystyrene core. Scale bar = 200 nm [reproduced with permission from [45]]. (**B**) Quantification of adhesion to anti-OVA antibody-coated microfluidic chambers of OVA-covered spheres, rigid discs, and PLNS at fixed particles size (200 nm). *Denotes statistical difference ($P < 0.05$) from all other groups [reproduced with permission from [45]]. (**C**) Quantification of adhesion to endothelialized microfluidic chambers of sLe^a spherical particles of various sizes under a range of shear rates [reproduced with permission from [46]]. (**D**) Bleeding times after intravenous injection of 15 mg/kg PLN formulations followed by tail transections in Balb/c mice. *Denotes statistical difference ($P < 0.05$) from saline and PLNs without peptides [reproduced with permission from [45]].

Pharmacokinetics and biodistribution are critical to the efficacy of systemically-administered hemostatic materials. After intravenous injection, hemostatic materials should circulate in the blood long enough to accumulate and act at the site of vascular injury and be excreted from the body with reasonable half-lives so as not to cause long-term risk of thrombosis. Patients

sustaining traumatic injury are usually transported within an hour to a Level 1 trauma center.[52] Within that hour of time, exsanguination is responsible for greater than one-third of deaths[1] and is therefore a reasonable time in which intravenous hemostats should be circulating and active. Particle circulation time is dependent on a number of factors including particle size, shape, and flexibility. Nanoparticles can be rapidly removed from circulation by macrophages lining the sinusoids in the liver and in the red pulp of the spleen. This phenomenon is readily observed in biodistribution studies for platelet substitutes such as PLGA-PLL-PEG-RGD nanoparticles where nearly 70% of particles are taken up by macrophages in the liver 5 minutes after injection[41] and also PLNs which demonstrate significant accumulation in the lungs, liver, and spleen 1 hour after injection. Phagocytosis of particles can be inhibited, however, by altering particle shape.[51,53] Uptake is highly dependent on local particle curvature at the point of macrophage attachment, and particles with low curvature surfaces are more difficult to phagocytose than those with high curvature. For example, particles with high aspect ratios (AR), such as worm-like particles (AR>20), only have two points at either end of the worm with high curvature for phagocytosis compared to spherical particles which have equal curvature all around for easy uptake.[53] Therefore, in addition to better margination under flow, elongated particles are more difficult to sequester and therefore have longer circulation times *in vivo*[54,55]. Flexible filamentous micelles have been shown to circulate for longer periods of time compared to rigid, crosslinked micelles of the same geometry.[55] Therefore, membrane flexibility also appears to inhibit macrophage uptake. As previously mentioned, smaller particles are desirable to minimize sequestration by the RES system.[51] Aside from better circulation time, smaller particles can prevent potential cardiopulmonary complications due to unintended blockage in the lungs and vessels.[56,57] Even at submicron size (~200 nm), PLNs and PLGA-PLL-PEG-NP produced

cardiopulmonary complications (evidenced by elevated heart rate and gasping) after intravenous injection of high doses.[41,45]

Ligand specificity. For particle-induced platelet aggregation, it is especially important that targeting ligands be specific to activated platelets to minimize risk of thrombosis. Binding to receptors on circulating quiescent platelets can cause off-target platelet aggregation and possibly even systemic platelet activation. A caveat of using RGD peptides is the lack of specificity to the GPIIb-IIIa integrin.[14] The RGD motif is conserved across many extracellular matrix proteins mediating cell adhesion such as fibrinectin, victronectin, collagen, and laminin[58] and is, therefore, recognized by multiple integrin receptors. Of the 5 platelet integrins, GPIIb-IIIa[11,12], $\alpha_v\beta_3$[59], and $\alpha_5\beta_1$ receptors[60] have RGD-dependent binding mechanisms to their respective ligands, thus, increasing the likelihood of undesired interaction between RGD-functionalized materials and inactive platelets. However, modifications to RGD peptides, such as cyclization to restrict conformational flexibility and optimization of flanking residues, have been shown to increase specificity for certain integrin receptors.[61–63] For example, liposomes functionalized with the cyclic RGD peptide, cyclo-CNPRGDY(OEt)RC, induced significant aggregation when mixed with ADP-activated platelets while inducing minimal aggregation when mixed with quiescent platelets (Figure 1.4A).[38] Addition of flanking residues to RGD peptides have been shown to produce a more active binding conformation and induce greater activated platelet aggregation *in vitro* (GRGDS > RGDS > RGD) without binding and/or activing quiescent platelets (Figure 1.4B).[41] When injected intravenously, PLGA-PLL-PEG-RGD nanoparticles (Figure 1.4C) with flanked RGD peptides reduced bleeding time more so than nanoparticles with non-flanked RGD peptides (Figure 1.4D-E), demonstrating that this increased peptide bioactivity translates to improved hemostatic function *in vivo*.[41] As discussed in the next section, particle specificity for activated platelets can be further

modulated by optimizing the linker length used to couple peptides to particle surfaces.[64]

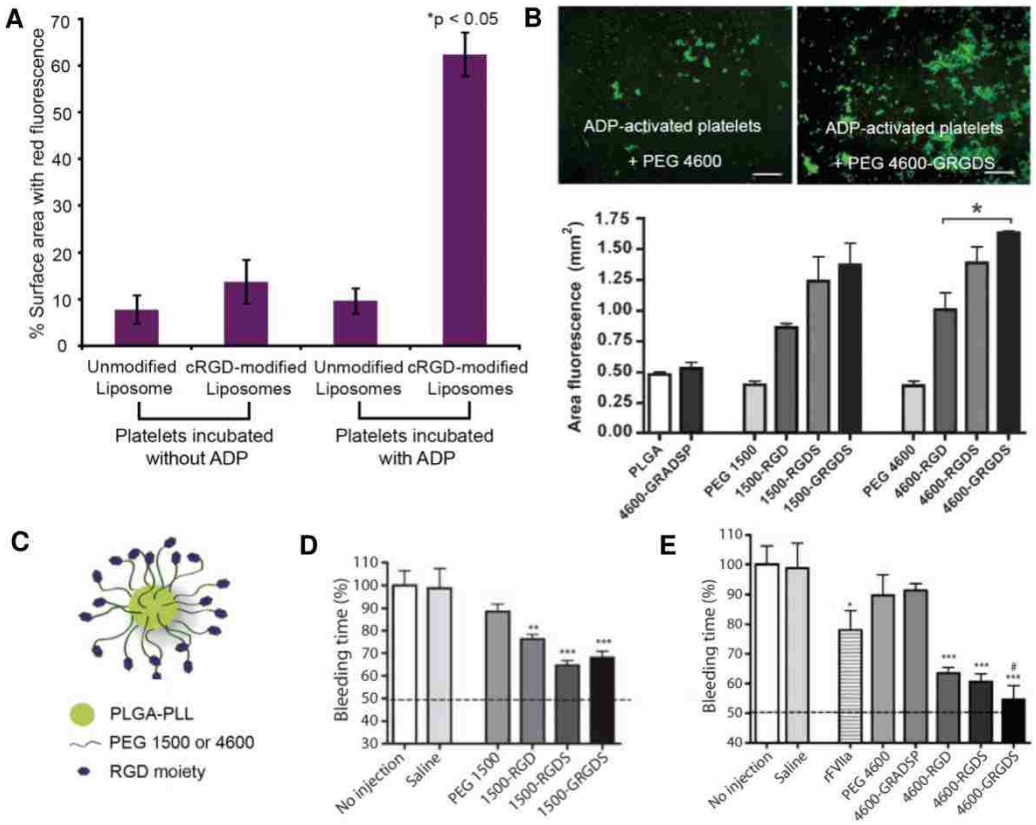

Figure 1.4. Data showing effects of ligand specificity and linker length on platelet aggregation and *in vivo* hemostatic function. Peptide modifications such as cyclization increase binding specificity of RGD moieties for activated platelets and specificity is confirmed in experiments such as that shown in (**A**), where inactive and ADP-activated fluorescently-labeled platelets are incubated with unmodified and cRGD-modified liposomes to confirm significant particle-induced aggregation in active platelets and minimal aggregation with inactive platelets [reproduced with permission from [38]]. (**B**) *In vitro* comparison of platelet aggregation produced by incubation of fluorescently-labeled platelets with RGD versus flanked RGD peptides attached to 1500 or 4600 Da PEG. $*P < 0.05$ for comparison to PEG 4600 alone [reproduced with permission from [41]]. (**C**) Schematic of PLGA-PLL-PEG-RGD nanoparticles [reproduced with permission from [41]]. Bleeding times of rats intravenously injected with 20 mg/mL suspension of PLGA-PLL-PEG-RGD nanoparticles synthesized with (**D**) PEG 1500 and (**E**) PEG 4600 followed by injury to the femoral artery [reproduced with permission from [41]]. (**D**) $*P < 0.01$, $***P < 0.001$ for comparison to PEG 1500. (**E**) $*P < 0.05$, $***P < 0.001$ for comparison to saline and $\#P < 0.05$ for comparison to rFVIIa.

Linker length. Thromboerythrocytes development revealed that interaction between RGD peptide ligands and platelets is highly dependent on linker length [21,64]. The length of the glycine linker or *n* in the peptide $(G)_n$-RGDF was shown to determine the extent of interaction between peptide-functionalized surfaces and platelets.[64] When conjugated with RGD peptides with linker lengths of 1, 3, and 9, polyacrylonitrile beads demonstrated little interaction with platelets, highly selective aggregation with active platelets, and strong interaction with both active and inactive platelets, respectively. A 3-residue linker (CGG) was therefore used in the preparation of the thromboerythrocytes by Coller et al.[21] The positive correlation between linker length and platelet interaction is likely due to closer proximity of RGD to receptors on platelet surfaces, increased conformational flexibility for binding, increased potential for assuming a secondary structure, or a combination of these factors.[64] Consistent with these observations, longer PEG (4600 Da) used in the construction of PLGA-PLL-PEG-RGD nanoparticles produced greater platelet aggregation *in vitro* than shorter PEG (1500 Da) (Figure 4B) and reduced bleeding time to a greater degree in animal models of femoral artery injury (Figure 1.4D-E). For most liposomal formulations, peptides (VBP, CBP, and cyclic RGD) were conjugated to DSPE-PEG_{2000}.[36–38]

Ligand or receptor density. Ligand density has been shown to be an important factor when engineering targeted nanoparticles for application in drug delivery and imaging[65–70] and is, likewise, critical when engineering hemostatic particles mimicking platelet adhesion or platelet aggregation as demonstrated in multiple studies[9,39,71,72]. When flowed through a perfusion chamber, liposomes of varying rGPIbα surface densities (0, 5.27×10^3, 1.00×10^4 molecules per liposome) and fixed rGPIα-IIα density (2×10^3 molecules per liposome) showed rGPIbα density-dependent adhesion of collagen-immobilized surfaces in the presence of soluble vWF.[9] At high shear rates

(1200 and 2400 s^{-1}), surface adhesion by functionalized liposomes increased with increasing rGPIbα. Interestingly, liposomes with the higher rGPIbα density had increasing adhesion with increasing shear whereas liposomes with no rGPIbα or the lower rGPIbα density demonstrated decreasing surface coverage with increasing shear. Similarly, experiments with varying rGPIα-IIα (0, 0.96 x 10^3, 2.17 x 10^3 molecules per liposome) and fixed rGPIbα (1.00 x 10^4 molecules per liposome) showed rGPIα-IIα density-dependent adhesion of collagen surfaces by functionalized liposomes. Liposomes with rGPIbα alone demonstrated transient adherence but no stable adhesion. These studies suggest that higher ligand density for targeting vWF and collagen is ideal for initial particle tethering and subsequent adhesion stabilization, especially under high shear rates.

For PLGA-PLL-PEG nanoparticle optimization, increasing GRGDS peptide content on nanoparticles by 100-fold decreased the required in vitro and in vivo dose for achieving hemostasis by 10-fold and 8-fold, respectively.[43,71] However, dose-dependent adverse effects were observed with the high density GRGDS formulation (GRGDS-NP100) compared to the lower-density formation (GRGDS-NP1). For example, while GRGDS-NP100 at 5 mg/kg doses could produce similar levels of improved 1-hr survival and reduced blood loss in rat liver trauma models as GRGDS-NP1 at 40 mg/kg, increasing the dose of GRGDS-NP100 to 20 mg/kg or 40 mg/kg drastically reduced percentage of animals surviving to 1 hour (Figure 1.5A-B). Adverse effects at high GRGDS-NP100 dosages can be attributed to saturation of GPIIb-IIIa receptors on activated platelets, which would inhibit platelet-platelet interaction, thus, preventing platelet aggregation and inducing anticoagulation (Figure 1.5C). This same phenomena was observed by Coller et al., who reported the loss of thromboerythrocyte aggregation with platelets in wells coated with high concentrations of fibrinogen.[72] These studies are important in highlighting that increased hemostatic potency from high ligand density is offset by safety concerns of bleeding out due to overdosing.

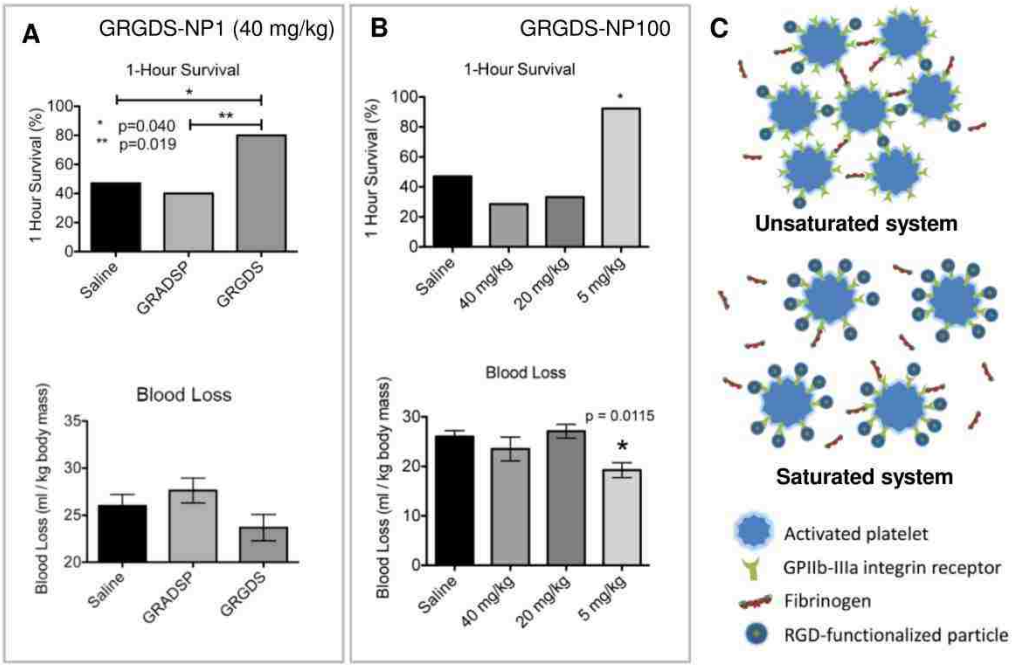

Figure 1.5. Data showing the effects of GRGDS ligand density on *in vivo* hemostatic function. Comparison between 1-hour survival (top) and blood loss (bottom) of lethal liver injury rat models after intravenous injection of (**A**) 40 mg/kg GRGDS-NP1 and (**B**) 5, 20, and 40 mg/kg GRGDS-NP100 demonstrates an 8-fold reduction in effective particle dosage (i.e. increased potency) when ligand density is increased 100-fold [reproduced with permission from [43,71]]. However, adverse effects are observed at 20 and 40 mg/kg GRGDS-NP100 most likely due to saturation of GPIIb-IIIa receptors on platelets which would prevent platelet aggregation (**C**). (**B**) *$P < 0.05$ compared to saline.

Ligand synergism. vWF- and collagen-binding work synergistically for platelet adhesion, and are, therefore, generally coupled on heteromultivalent platelet substitutes (Figure 1.6A).[9,38,39,45] When compared to liposomes with VBP or CBP alone, heteromultivalent liposomes with both peptides had significantly greater adhesion to vWF- and collagen-coated plates at all tested shear rates (5, 30, 55 dynes/cm^2).[39] The optimal ratio of vWF- to collagen-targeting ligand was determined using liposomes with varying ratios of DSPE-PEG-VBP and DSPE-PEG-CBP (80:20, 60:40, 50:50, 40:60, 20:80) at a fixed 5 mol % DSPE-PEG-peptide composition (Figure 1.6B-D).[39] At low shear rate, liposomes with a greater proportion of CBP had the greatest adhesion at 30 min and retention at 45 min (Figure 1.6B) while those with a greater

proportion of VBP had the greatest adhesion and retention at high shear rate (Figure 1.6D). At medium shear rate, near 1:1 ratio of CBP to VBP yielded the greatest adhesion and retention (Figure 1.6C). These studies demonstrate that collagen-binding is the dominant mechanism for adhesion under low shear while vWF-binding is the dominant mechanism under high shear. Furthermore, the ratio of targeting ligands can be optimized to maximize the adhesiveness of particle platforms.

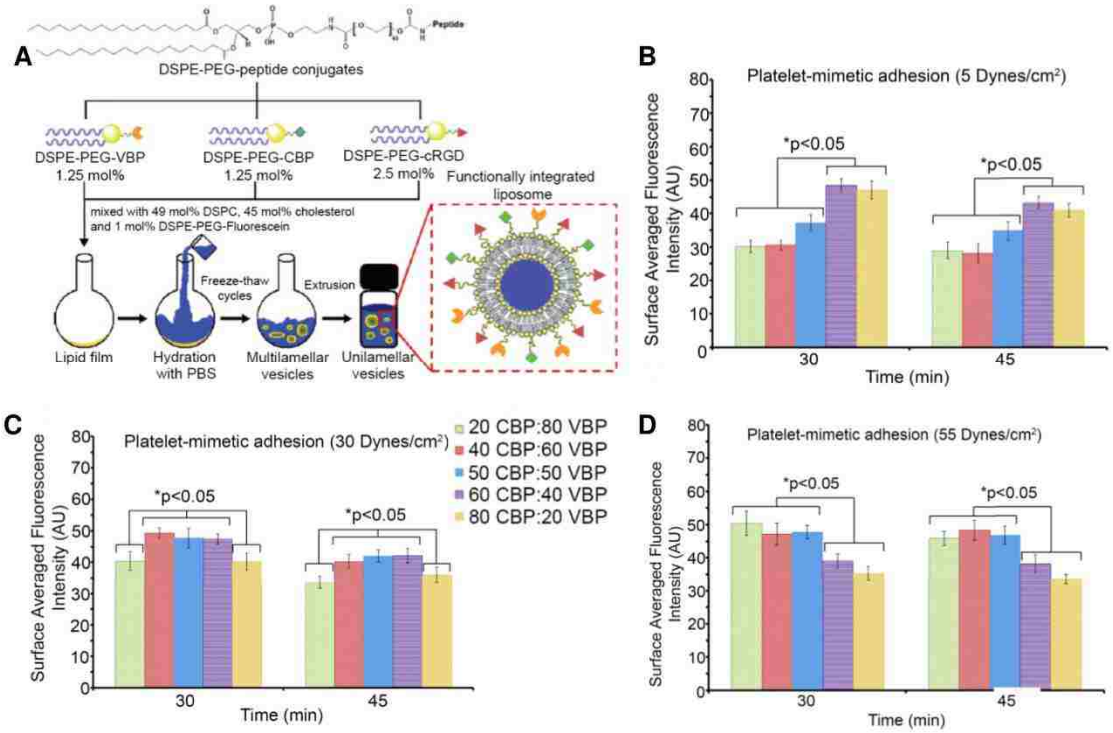

Figure 1.6. Data showing the effects of ligand synergism on platelet adhesion. (A) Synergistic ligands can be incorporated into heteromultivalent liposomes using a mixture of DSPE-PEG-peptide conjugates during liposome synthesis [reproduced with permission from [38]]. Liposomes with fixed 5 mol% DSPE-PEG-peptide was synthesized with varying ratios DSPE-PEG-CBP to DSPE-PEG-VBP to determine the optimal ratio for maximizing liposome adhesion to the subendothelial matrix. Liposomes were flowed through a parallel plate fluidic chamber over glass slides coated with 1:1 ratio of vWF to collagen under a range of shear stresses. Adhesion at (B) 5 dynes/cm^2, (C) 30 dynes/cm^2, and (D) 55 dynes/cm^2 was quantified by measuring fluorescence from fluorescently-labeled liposomes [reproduced with permission from [39]].

1.3 Fibrin cross-linking agents

1.3.1 Secondary hemostasis

During *secondary hemostasis*, the fibrin matrix is formed by the coagulation cascade (Figure 1B). Fibrinogen is the 340 kDa glycoprotein precursor of fibrin and, under normal physiologic conditions, circulates in the blood at an average concentration of 3.0 mg/mL.[73] Fibrinogen is made of three pairs of polypeptide chains– Aα, Bβ, and γ.[74] It has a symmetric elongated structure made up of three nodules, a central E nodule containing the N-termini of all six chains from which the chains extend as two sets of three-chained coiled coils into two distal D nodules containing the C-termini of the Bβ and γ chains (βC and γC). The Aα chains exit the D nodules and travel back to the E nodule where their C-termini (αC) interact with each other and the E nodule. After tissue damage, thrombin is activated locally as a result of the coagulation cascade and cleaves fibrinopeptides A and B (FPA and FPB) from the N-termini of Aα and Bβ chains, respectively, exposing A and B knob peptide domains. Knobs A and B, in what are now fibrin monomers, interact with holes a and b in γC and βC, respectively, resulting in the formation of half-staggered, double-stranded fibrin protofibrils. Non-specific interactions of αC cause protofibrils to aggregate laterally, bundle into fibers, and branch to form a three-dimensional insoluble hydrogel scaffold for platelets, blood cells, and other clot components. The transglutaminase Factor XIIIa (FXIIIa) then stabilizes fibrin by creating intra- and inter-fiber crosslinks through amide bond formation between lysine and glutamic acid residues.

1.3.2 Polymers for modulating formation of the fibrin matrix

Difficulty in clotting, or coagulopathy, can result from the absence, deficiency, or dysfunction of clotting factor(s) which participate in the coagulation cascade ultimately leading to thrombin activation. A shortage of functional clotting factors can be due to genetic defect as in hemophilia, the result of large volume blood loss as in trauma-induced coagulopathy (TIC), or the

result of anticoagulant use (e.g. warfarin). When thrombin activation is inhibited, fibrin formation is impeded. Fibrin matrices that form at low thrombin levels are more porous and made up of loose, thick fibrin fibers as opposed to denser networks of thin fibers.[75–77] The former, in addition to producing mechanically weaker gels for maintaining hemostasis, is also more susceptible to enzymatic degradation (i.e. fibrinolysis).[78] Therefore, affecting fibrin formation using materials that mimic clotting factors is another strategy for inducing strong clot formation for hemostasis.

Early successful attempts at developing a substitute for the thrombin-modified fibrinogen E domain using synthetic polymer constructs were reported by Lorand et al.[79] Using the synthetic peptide mimic of knob A (GPRP)[80], Lorand et al. synthesized a double-headed ligand bis(Gly-Pro-Arg-Pro-amido)polyethylene glycol and showed that it could replace the thrombin-modified E nodule for non-covalent fibrinogen-fibrinogen or D-D crosslinking via interaction with two hole a's in neighboring γ-chains (Figure 1.7A).[79] Presence of free knob A peptide mimic in a mixture of thrombin and fibrinogen inhibits clot formation due to competition with fibrin monomers for hole a.[80] However, as demonstrated by Lorand et al., a bivalent construct terminated with knob A peptides is able to crosslink fibrin. Furthermore, this behavior was biphasic with "productive" crosslink-forming behavior at the lower polymer concentration range and "non-productive" crosslink-absent behavior at the higher polymer concentration range (Figure 1.7B). This biphasic behavior was attributed to inter-polymer competition for available hole a's (two per fibrinogen molecule) making it difficult for the unbound end of a bound polymer to find a second hole a for crosslinking. Additionally, these studies showed that 900 Da PEGs were large enough to span the distance of two hole a's (a minimum of 32 Å)[81], an important engineering design specification for future fibrin-crosslinking constructs. Lorand et al. were the first to demonstrate *in vitro* that fibrin polymerization in the absence of thrombin could be driven by synthetic polymers. However, due to

their ability to crosslink fibrinogen, knob A-terminated polymers should be limited to local administration rather than systemic administration.

In subsequent work, Soon et al. conjugated cysteine-terminated knob A peptide mimics (GPRPAAC) to two-arm and four-arm maleimide-functionalized PEGs (2-20 kDa). The conjugates were evaluated *in vitro* with thrombin and were used to modulate fibrin structure for tissue engineering applications rather than drive thrombin-independent fibrin polymerization.[82] Biphasic behavior was again observed in these studies. At higher molar ratios (1:1 and 10:1) of $GPRP_4$-PEG to fibrinogen, final clot turbidities were significantly reduced which is likely due to inhibited fibrin formation evidenced by prolonged clotting times and the reduction of clottable protein from >90% to 70%. This behavior is, again, likely due to competition between conjugates as well as competition with naturally-occurring knob:hole interactions. At the lower 1:10 molar ratio of $GPRP_4$-PEG to fibrinogen, final clot turbidities were slightly increased indicating larger fiber diameters and higher fiber density (Figure 1.7C). The behavior seen at the 1:10 molar ratio suggests that lower concentrations of polymers might have resulted in the same "productive" behavior observed in the work by Lorand et al. However, further investigation was completed only at the 1:1 molar ratio which continued to show "non-productive" behavior as evidenced by the reduced elastic modulus (i.e. stiffness) of fibrin. Later work from this group reported the use of PEGylated knob peptides as anticoagulants.[83]

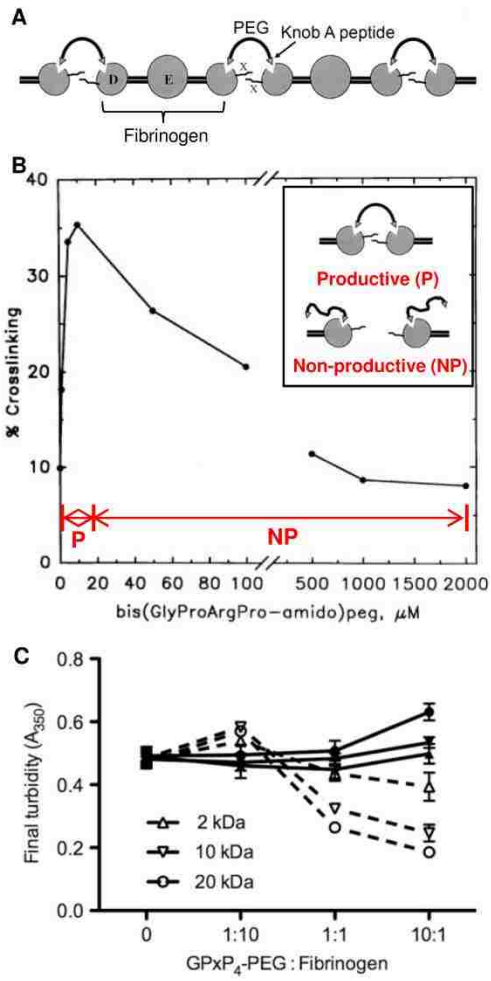

Figure 1.7. Knob A-peptide terminated polymers for fibrin(ogen) crosslinking *in vitro*. (**A**) A bivalent 900 Da PEG terminated on either end with knob A peptide (GPRP), bis(GlyProArgPro-amido)peg, was synthesized to crosslink fibrinogen D nodules in the absence of thrombin. (**B**) Bis(GlyProArgPro-amido)peg demonstrated biphasic behavior where lower "productive" polymer concentrations formed D-D crosslinks and higher "non-productive" polymer concentrations showed less efficient crosslinking due to competition of polymers for the finite number of hole a's. (**A-B**) Adapted with permission from [79]. Copyright © 1998 National Academy of Sciences, U.S.A. (**C**) Biphasic behavior was also observed in turbidity measurements for fibrin formed with 4-arm PEG-knob A conjugates of various molecular weights. Filled in symbols and solid lines represent scrambled conjugate controls and empty symbols and dotted lines represent knob A conjugates [reproduced with permission from [82]].

Due to the accessibility of hole a's in both fibrin and fibrinogen, knob A-terminated polymers can cause thrombosis (off-target clot formation) if

administered systemically and are, therefore, not suitable as intravenous hemostats. However, knob A peptides can be readily substituted with other peptides or proteins that specifically bind fibrin and not fibrinogen to create hemostatic polymers that only induce clotting at sites of injury. Recently, our lab reported the use of fibrin-binding peptides identified via phage display by Kolodziej et al[84–87] to create linear polymer hemostats (PolySTAT) for crosslinking fibrin (Figure 1.8A).[88] PolySTAT is composed primarily of a poly(hydroxyethyl)methacrylate [p(HEMA)] backbone (80%) with pendant cyclic fibrin-binding peptides conjugated to *N*-hydroxysuccinimidyl ester methacrylate (NHSMA) comonomers. Polymers with average molecular weight of 45 kDa and ~ 16 peptides were synthesized by reversible addition-fragmentation chain-transfer (RAFT) polymerization. Confocal images of fluorescently-labeled fibrin formed with fluorescent PolySTAT showed integration of the polymer into fibrin fibers, and SEM images showed altered fibrin networks which were denser and less porous than controls (Figure 1.8B). Elastic moduli of PolySTAT-crosslinked fibrin was increased 2-3 fold, and with the addition of plasmin into the purified system, the PolySTAT-integrated fibrin network showed significantly reduced fibrinolysis compared to scrambled controls. Increased mechanical strength as well as resistance to enzymatic breakdown is particularly important to resolve bleeding in conditions such as TIC, where clot strength is reduced and hyperfibrinolytic activity may be observed.[89,90] Intravenous injection of PolySTAT at a dose of 15 mg/kg in rat models of femoral artery injury and fluid resuscitation resulted in significantly greater survival rates compared to scrambled controls (Figure 1.8C) as well as reduced blood loss (Figure 1.8D) and fluid resuscitation requirements to maintain blood pressure above 60 mm Hg.

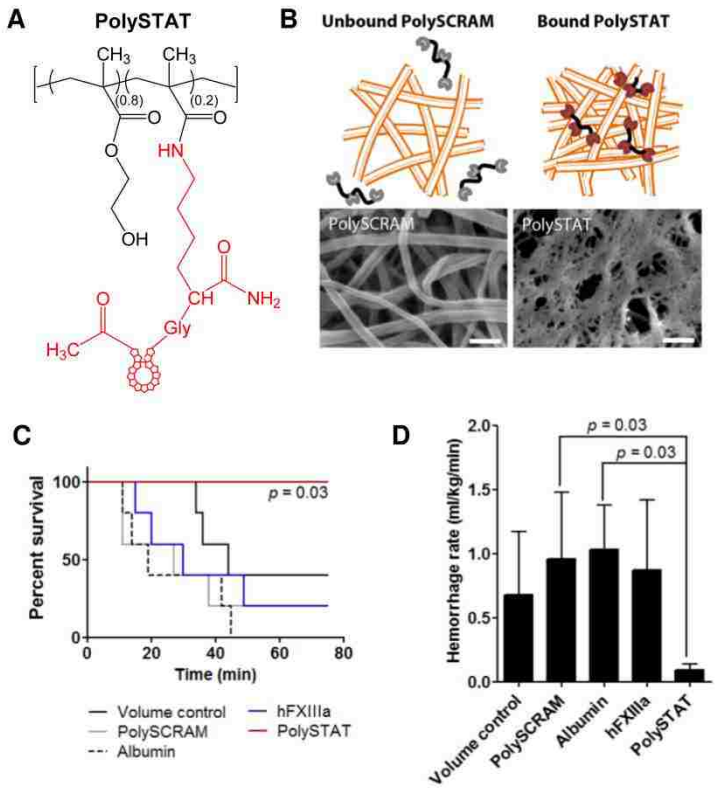

Figure 1.8. *In vitro* characterization of PolySTAT-modified fibrin and *in vivo* evaluation of hemostatic efficacy. (**A**) PolySTAT is a synthetic poly(HEMA) polymer with multivalent display of fibrin-binding peptides (shown in red). (**B**) PolySTAT-modified fibrin has a denser mesh structure compared to control fibrin (SEM scalebar = 10 μm). Intravenous injection of PolySTAT in a rat femoral injury model significantly (**C**) increases survival rate and (**D**) reduces hemorrhage rate [reproduced with permission from [88]].

1.3.3 Fibrin-binding microgel particles

In another recent publication, ultra-low crosslinked (ULC) poly(*N*-isopropylacrylamide-*co*-acrylic acid) (pNIPAm-AAc) microgel particles with surface-conjugated single domain variable fragments (sdFv's) with affinity for fibrin, termed platelet-like particles (PLPs), were reported for their application as intravenous hemostats in injured rat models (Figure 1.9A).[91] PLPs were engineered with low core crosslinking densities (<0.5%) to create particle bodies with high deformability to mimic platelet deformation upon fibrin formation. Despite their given name, PLPs are technically unresponsive until secondary hemostasis and were included in this section

because of their enhancement of fibrin formation rather than initial platelet plug formation. PLPs added to platelet-poor plasma (PPP) promoted fibrin formation in an endothelialized microfluidic device to nearly comparable fibrin levels observed with platelet-rich plasma (PRP) and, similar to PolySTATs, produced denser fibrin networks (Figure 1.9B). Bleeding times were halved in rat models of femoral vein injury. In addition to high deformability, PLPs were likened to platelets because of clot collapse that was observed 24-48 h after clot formation (Figure 1.9C). A caveat, as the authors also noted, is that clot retraction due to actomyosin contraction in native platelets attached to the fibrin matrix occurs significantly more rapidly (within minutes to an hour after clot formation)[92].

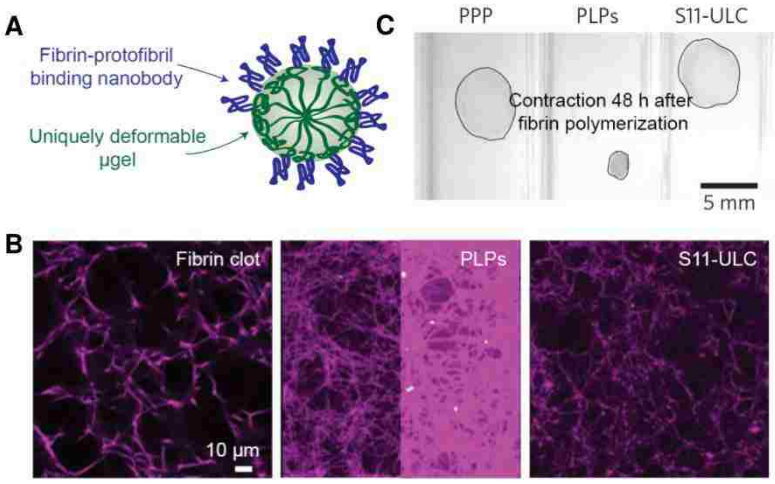

Figure 1.9. *In vitro* characterization of PLP-modified fibrin. (**A**) PLPs have multivalent display of fibrin-binding nanobodies. (**B**) PLP increases the density of the fibrin matrix in comparison to non-binding microgel controls (S11-ULC). (**C**) PLP integration in clots results in contraction 48 hours after fibrin polymerization [reproduced with permission from [91]].

1.4 Conclusions

Current methods of resolving bleeding after traumatic injury include using topical hemostats which are limited to treating accessible wounds and by transfusion of blood products or recombinant clotting factors to restore hemostatic function. Biologically-derived products have many limitations such as short shelf life, involved manufacturing processes, and risk of viral

transmission. Therefore, there has been growing interest in developing synthetic hemostatic agents for systemic administration to resolve bleeding in less accessible injuries (e.g. internal bleeding in the trunk). Numerous platelet substitutes have been developed using nanoparticles commonly used in drug delivery such as liposomes and PLGA nanoparticles and have been evaluated on their ability to mimic platelet margination and adhesion to vessel walls and to induce platelet aggregation. Investigation of these platelet-like constructs have demonstrated the importance of physical parameters (i.e. particle size, shape, and flexibility) in platelet mimicry as well as methodical approaches to combining and displaying binding motifs for optimal hemostatic activity specific to the site of vascular injury. With more recent materials, we have seen emergent properties mimicking platelet contraction and deformation. Dynamic particles capable of mimicking platelet contraction at the necessary timescale could potentially stiffen clots to the same degree as native platelet contraction, and thus induce hemostasis more rapidly. Recent materials have also started engaging fibrin to stabilize clot structure and provide an orthogonal approach to hemostasis. Future work on intravenous hemostats will likely focus on the amalgamation of both optimized physical particle properties and binding motif arrangement into one platelet construct. Furthermore, future hemostatic agents may be engineered to engage both primary and secondary hemostasis mechanisms for a stronger hemostatic response.

1.5 Acknowledgements

This work is supported by NIH NIBIB 1R21EB018637 and the Bioengineering Cardiovascular Training Grant NIH 2T32EB001650-06A2 (LWC).

References

(1) Kauvar, D. S., Lefering, R., and Wade, C. E. (2006) Impact of hemorrhage on trauma outcome: an overview of epidemiology, clinical presentations, and therapeutic considerations. *J Trauma 60*, S3–11.

(2) Eastridge, B. J., Mabry, R. L., Seguin, P., Cantrell, J., Tops, T., Uribe, P., Mallett, O., Zubko, T., Oetjen-Gerdes, L., Rasmussen, T. E., et al. (2012) Death on the battlefield (2001-2011): implications for the future of combat casualty care. *J. Trauma Acute Care Surg. 73*, S431–7.

(3) Achneck, H. E., Sileshi, B., Jamiolkowski, R. M., Albala, D. M., Shapiro, M. L., and Lawson, J. H. (2010) A comprehensive review of topical hemostatic agents: efficacy and recommendations for use. *Ann Surg 251*, 217–228.

(4) Spahn, D. R., Bouillon, B., Cerny, V., Coats, T. J., Duranteau, J., Fernandez-Mondejar, E., Filipescu, D., Hunt, B. J., Komadina, R., Nardi, G. et al. (2013) Management of bleeding and coagulopathy following major trauma: an updated European guideline. *Crit Care 17*, R76.

(5) Takeoka, S., Teramura, Y., Okamura, Y., Tsuchida, E., Handa, M., and Ikeda, Y. (2002) Rolling properties of rGPIbalpha-conjugated phospholipid vesicles with different membrane flexibilities on vWf surface under flow conditions. *Biochem Biophys Res Commun 296*, 765–770.

(6) Pease, D. C. (1956) An electron microscope study of red bone marrow. *Blood 11*, 501–526.

(7) Machlus, K. R., and Italiano Jr., J. E. (2013) The incredible journey: From megakaryocyte development to platelet formation. *J Cell Biol 201*, 785–796.

(8) Gentile, F., Chiappini, C., Fine, D., Bhavane, R. C., Peluccio, M. S., Cheng, M. M. C., Liu, X., Ferrari, M., and Decuzzi, P. (2008) The effect of shape on the margination dynamics of non-neutrally buoyant particles in two-dimensional shear flows. *J. Biomech. 41*, 2312–2318.

(9) Nishiya, T., Kainoh, M., Murata, M., Handa, M., and Ikeda, Y. (2002) Reconstitution of adhesive properties of human platelets in liposomes carrying both recombinant glycoproteins Ia/IIa and Ib alpha under flow conditions: specific synergy of receptor-ligand interactions. *Blood 100*, 136–142.

(10) Chen, H., Locke, D., Liu, Y., Liu, C., and Kahn, M. L. (2002) The platelet receptor GPVI mediates both adhesion and signaling responses to collagen in a receptor density-dependent fashion. *J Biol Chem 277*, 3011–3019.

(11) Pytela, R., Pierschbacher, M. D., Ginsberg, M. H., Plow, E. F., and Ruoslahti, E. (1986) Platelet membrane glycoprotein IIb/IIIa: member of a family of Arg-Gly-Asp--specific adhesion receptors. *Science (80-.). 231*, 1559–1562.

(12) Plow, E. F., and Ginsberg, M. H. (1989) Cellular adhesion: GPIIb-IIIa as a prototypic adhesion receptor. *Prog Hemost Thromb 9*, 117–156.
(13) Salsmann, A., Schaffner-Reckinger, E., Kabile, F., Plancon, S., and Kieffer, N. (2005) A new functional role of the fibrinogen RGD motif as the molecular switch that selectively triggers integrin alphaIIbbeta3-dependent RhoA activation during cell spreading. *J Biol Chem 280*, 33610–33619.
(14) Modery-Pawlowski, C. L., Tian, L. L., Pan, V., McCrae, K. R., Mitragotri, S., and Sen Gupta, A. (2013) Approaches to synthetic platelet analogs. *Biomaterials 34*, 526–541.
(15) Wagner, C. L., Mascelli, M. A., Neblock, D. S., Weisman, H. F., Coller, B. S., and Jordan, R. E. (1996) Analysis of GPIIb/IIIa receptor number by quantification of 7E3 binding to human platelets. *Blood 88*, 907–914.
(16) Bennett, J. S., and Vilaire, G. (1979) Exposure of platelet fibrinogen receptors by ADP and epinephrine. *J Clin Invest 64*, 1393–1401.
(17) Marguerie, G. A., Edgington, T. S., and Plow, E. F. (1980) Interaction of fibrinogen with its platelet receptor as part of a multistep reaction in ADP-induced platelet aggregation. *J Biol Chem 255*, 154–161.
(18) Niiya, K., Hodson, E., Bader, R., Byers-Ward, V., Koziol, J. A., Plow, E. F., and Ruggeri, Z. M. (1987) Increased surface expression of the membrane glycoprotein IIb/IIIa complex induced by platelet activation. Relationship to the binding of fibrinogen and platelet aggregation. *Blood 70*, 475–483.
(19) Agam, G., and Livne, A. (1983) Passive participation of fixed platelets in aggregation facilitated by covalently bound fibrinogen. *Blood 61*, 186–191.
(20) Agam, G., and Livne, A. A. (1992) Erythrocytes with covalently bound fibrinogen as a cellular replacement for the treatment of thrombocytopenia. *Eur J Clin Invest 22*, 105–112.
(21) Coller, B. S., Springer, K. T., Beer, J. H., Mohandas, N., Scudder, L. E., Norton, K. J., and West, S. M. (1992) Thromboerythrocytes. In vitro studies of a potential autologous, semi-artificial alternative to platelet transfusions. *J Clin Invest 89*, 546–555.
(22) Levi, M., Friederich, P. W., Middleton, S., de Groot, P. G., Wu, Y. P., Harris, R., Biemond, B. J., Heijnen, H. F., Levin, J., and ten Cate, J. W. (1999) Fibrinogen-coated albumin microcapsules reduce bleeding in severely thrombocytopenic rabbits. *Nat Med 5*, 107–111.
(23) Davies, A. R., Judge, H. M., May, J. A., Glenn, J. R., and Heptinstall, S. (2002) Interactions of platelets with Synthocytes, a novel platelet substitute. *Platelets 13*, 197–205.
(24) Allen, T. M., and Cullis, P. R. (2013) Liposomal drug delivery systems: from concept to clinical applications. *Adv. Drug Deliv. Rev. 65*, 36–48.

(25) Sie, P., Gillois, M., Boneu, B., Chap, H., Bierme, R., and Douste-Blazy, L. (1980) Reconstitution of liposomes bearing platelet receptors for human von Willebrand factor. *Biochem Biophys Res Commun 97*, 133–138.
(26) Baldassare, J. J., Kahn, R. A., Knipp, M. A., and Newman, P. J. (1985) Reconstruction of platelet proteins into phospholipid vesicles. Functional proteoliposomes. *J Clin Invest 75*, 35–39.
(27) Parise, L. V, and Phillips, D. R. (1985) Platelet membrane glycoprotein IIb-IIIa complex incorporated into phospholipid vesicles. Preparation and morphology. *J Biol Chem 260*, 1750–1756.
(28) Rybak, M. E. (1989) A platelet substitute-the plateletsome to be used in transfusion therapy, pp 1–41. US Army Medical Research and Development Command, Fort Detrick, Frederick, Maryland.
(29) Rybak, M. E., and Renzulli, L. A. (1993) A liposome based platelet substitute, the plateletsome, with hemostatic efficacy. *Biomater Artif Cells Immobil. Biotechnol 21*, 101–118.
(30) Kitaguchi, T., Murata, M., Iijima, K., Kamide, K., Imagawa, T., and Ikeda, Y. (1999) Characterization of liposomes carrying von Willebrand factor-binding domain of platelet glycoprotein Ibalpha: a potential substitute for platelet transfusion. *Biochem Biophys Res Commun 261*, 784–789.
(31) Nishiya, T., Kainoh, M., Murata, M., Handa, M., and Ikeda, Y. (2001) Platelet interactions with liposomes carrying recombinant platelet membrane glycoproteins or fibrinogen: approach to platelet substitutes. *Artif Cells Blood Substit Immob. Biotechnol 29*, 453–464.
(32) Okamura, Y., Maekawa, I., Teramura, Y., Maruyama, H., Handa, M., Ikeda, Y., and Takeoka, S. (2005) Hemostatic effects of phospholipid vesicles carrying fibrinogen gamma chain dodecapeptide in vitro and in vivo. *Bioconjug Chem 16*, 1589–1596.
(33) Okamura, Y., Takeoka, S., Teramura, Y., Maruyama, H., Tsuchida, E., Handa, M., and Ikeda, Y. (2005) Hemostatic effects of fibrinogen gamma-chain dodecapeptide-conjugated polymerized albumin particles in vitro and in vivo. *Transfusion 45*, 1221–1228.
(34) Okamura, Y., Fujie, T., Maruyama, H., Handa, M., Ikeda, Y., and Takeoka, S. (2007) Prolonged hemostatic ability of polyethylene glycol-modified polymerized albumin particles carrying fibrinogen gamma-chain dodecapeptide. *Transfusion 47*, 1254–1262.
(35) Okamura, Y., Fujie, T., Nogawa, M., Maruyama, H., Handa, M., Ikeda, Y., and Takeoka, S. (2008) Haemostatic effects of polymerized albumin particles carrying fibrinogen gamma-chain dodecapeptide as platelet substitutes in severely thrombocytopenic rabbits. *Transfus Med 18*, 158–166.
(36) Modery, C. L., Ravikumar, M., Wong, T. L., Dzuricky, M. J., Durongkaveroj, N., and Sen Gupta, A. (2011) Heteromultivalent

liposomal nanoconstructs for enhanced targeting and shear-stable binding to active platelets for site-selective vascular drug delivery. *Biomaterials 32*, 9504–9514.

(37) Ravikumar, M., Modery, C. L., Wong, T. L., Dzuricky, M., and Sen Gupta, A. P. D. (2012) Mimicking Adhesive Functionalities of Blood Platelets using Ligand-Decorated Liposomes. *Bioconjug Chem 23*, 1266–1275.

(38) Ravikumar, M., Modery, C. L., Wong, T. L., and Gupta, A. S. (2012) Peptide-decorated liposomes promote arrest and aggregation of activated platelets under flow on vascular injury relevant protein surfaces in vitro. *Biomacromolecules 13*, 1495–1502.

(39) Modery-Pawlowski, C. L., Tian, L. L., Ravikumar, M., Wong, T. L., and Sen Gupta, A. (2013) In vitro and in vivo hemostatic capabilities of a functionally integrated platelet-mimetic liposomal nanoconstruct. *Biomaterials 34*, 3031–3041.

(40) Okamura, Y., Takeoka, S., Eto, K., Maekawa, I., Fujie, T., Maruyama, H., Ikeda, Y., and Handa, M. (2009) Development of fibrinogen gamma-chain peptide-coated, adenosine diphosphate-encapsulated liposomes as a synthetic platelet substitute. *J Thromb Haemost 7*, 470–477.

(41) Bertram, J. P., Williams, C. A., Robinson, R., Segal, S. S., Flynn, N. T., and Lavik, E. B. (2009) Intravenous hemostat: nanotechnology to halt bleeding. *Sci Transl Med 1*, 11ra22.

(42) M. L. Hans, A. M. L. (2002) Biodegradable nanoparticles for drug delivery and targeting. *Curr. Opin. Solid State Mater. Sci. 6*, 319.

(43) Shoffstall, A. J., Atkins, K. T., Groynom, R. E., Varley, M. E., Everhart, L. M., Lashof-Sullivan, M. M., Martyn-Dow, B., Butler, R. S., Ustin, J. S., and Lavik, E. B. (2012) Intravenous hemostatic nanoparticles increase survival following blunt trauma injury. *Biomacromolecules 13*, 3850–3857.

(44) Doshi, N., Prabhakarpandian, B., Rea-Ramsey, A., Pant, K., Sundaram, S., and Mitragotri, S. (2010) Flow and adhesion of drug carriers in blood vessels depend on their shape: A study using model synthetic microvascular networks. *J. Control. Release 146*, 196–200.

(45) Anselmo, A. C., Modery-Pawlowski, C. L., Menegatti, S., Kumar, S., Vogus, D. R., Tian, L. L., Chen, M., Squires, T. M., Sen Gupta, A., and Mitragotri, S. (2014) Platelet-like Nanoparticles: Mimicking Shape, Flexibility, and Surface Biology of Platelets To Target Vascular Injuries. *ACS Nano 8*, 11243–53.

(46) Charoenphol, P., Huang, R. B., and Eniola-Adefeso, O. (2010) Potential role of size and hemodynamics in the efficacy of vascular-targeted spherical drug carriers. *Biomaterials 31*, 1392–402.

(47) Muller, K., Fedosov, D. A., and Gompper, G. (2014) Margination of micro- and nano-particles in blood flow and its effect on drug delivery. *Sci Rep 4*, 4871.
(48) Müller, K., Fedosov, D. a, and Gompper, G. (2014) Margination of micro- and nano-particles in blood flow and its effect on drug delivery. *Sci. Rep. 4*, 4871.
(49) Decuzzi, P., Pasqualini, R., Arap, W., and Ferrari, M. (2009) Intravascular delivery of particulate systems: does geometry really matter? *Pharm. Res. 26*, 235–43.
(50) Jones, S. W., Roberts, R. A., Robbins, G. R., Perry, J. L., Kai, M. P., Chen, K., Bo, T., Napier, M. E., Ting, J. P., Desimone, J. M., et al. (2013) Nanoparticle clearance is governed by Th1/Th2 immunity and strain background. *J Clin Invest 123*, 3061–3073.
(51) Champion, J. a, and Mitragotri, S. (2006) Role of target geometry in phagocytosis. *Proc. Natl. Acad. Sci. U. S. A. 103*, 4930–4.
(52) Swaroop, M., Straus, D. C., Agubuzu, O., Esposito, T. J., Schermer, C. R., and Crandall, M. L. (2013) Pre-hospital transport times and survival for Hypotensive patients with penetrating thoracic trauma. *J Emerg Trauma Shock 6*, 16–20.
(53) Champion, J. a, and Mitragotri, S. (2009) Shape induced inhibition of phagocytosis of polymer particles. *Pharm. Res. 26*, 244–9.
(54) Arnida, Janát-Amsbury, M. M., Ray, a, Peterson, C. M., and Ghandehari, H. (2011) Geometry and surface characteristics of gold nanoparticles influence their biodistribution and uptake by macrophages. *Eur. J. Pharm. Biopharm. 77*, 417–23.
(55) Geng, Y., Dalhaimer, P., Cai, S., Tsai, R., Tewari, M., Minko, T., and Discher, D. E. (2007) Shape effects of filaments versus spherical particles in flow and drug delivery. *Nat. Nanotechnol. 2*, 249–255.
(56) Dobrovolskaia, M. A., Aggarwal, P., Hall, J. B., and McNeil, S. E. (2008) Preclinical studies to understand nanoparticle interaction with the immune system and its potential effects on nanoparticle biodistribution. *Mol Pharm 5*, 487–495.
(57) He, C., Hu, Y., Yin, L., Tang, C., and Yin, C. (2010) Effects of particle size and surface charge on cellular uptake and biodistribution of polymeric nanoparticles. *Biomaterials 31*, 3657–66.
(58) Bennett, J. S., Berger, B. W., and Billings, P. C. (2009) The structure and function of platelet integrins. *J Thromb Haemost 7 Suppl 1*, 200–205.
(59) Cheresh, D. A. (1987) Human endothelial cells synthesize and express an Arg-Gly-Asp-directed adhesion receptor involved in attachment to fibrinogen and von Willebrand factor. *Proc Natl Acad Sci U S A 84*, 6471–6475.

(60) Pierschbacher, M. D., and Ruoslahti, E. (1984) Cell attachment activity of fibronectin can be duplicated by small synthetic fragments of the molecule. *Nature 309*, 30–33.
(61) Pierschbacher, M. D., and Ruoslahti, E. (1987) Influence of stereochemistry of the sequence Arg-Gly-Asp-Xaa on binding specificity in cell adhesion. *J Biol Chem 262*, 17294–17298.
(62) Cheng, S., Craig, W. S., Mullen, D., Tschopp, J. F., Dixon, D., and Pierschbacher, M. D. (1994) Design and synthesis of novel cyclic RGD-containing peptides as highly potent and selective integrin alpha IIb beta 3 antagonists. *J Med Chem 37*, 1–8.
(63) Srinivasan, R., Marchant, R. E., and Gupta, A. S. (2009) In vitro and in vivo platelet targeting by cyclic RGD-modified liposomes. *J Biomed Mater Res A 93*, 1004–1015.
(64) Beer, J. H., Springer, K. T., and Coller, B. S. (1992) Immobilized Arg-Gly-Asp (RGD) peptides of varying lengths as structural probes of the platelet glycoprotein IIb/IIIa receptor. *Blood 79*, 117–128.
(65) Gu, F., Zhang, L., Teply, B. a, Mann, N., Wang, A., Radovic-Moreno, A. F., Langer, R., and Farokhzad, O. C. (2008) Precise engineering of targeted nanoparticles by using self-assembled biointegrated block copolymers. *Proc. Natl. Acad. Sci. U. S. A. 105*, 2586–91.
(66) Garg, A., Tisdale, A. W., Haidari, E., and Kokkoli, E. (2009) Targeting colon cancer cells using PEGylated liposomes modified with a fibronectin-mimetic peptide. *Int. J. Pharm. 366*, 201–10.
(67) Gindy, M. E., Ji, S., Hoye, T. R., Panagiotopoulos, A. Z., and Prud'homme, R. K. (2008) Preparation of poly(ethylene glycol) protected nanoparticles with variable bioconjugate ligand density. *Biomacromolecules 9*, 2705–11.
(68) Olivier, V., Meisen, I., Meckelein, B., Hirst, T. R., Peter-Katalinic, J., Schmidt, M. A., and Frey, A. (2003) Influence of targeting ligand flexibility on receptor binding of particulate drug delivery systems. *Bioconjug. Chem. 14*, 1203–8.
(69) Roche, A. M., James, M. F., Bennett-Guerrero, E., and Mythen, M. G. (2006) A head-to-head comparison of the in vitro coagulation effects of saline-based and balanced electrolyte crystalloid and colloid intravenous fluids. *Anesth Analg 102*, 1274–1279.
(70) Elias, D. R., Poloukhtine, A., Popik, V., and Tsourkas, A. (2013) Effect of ligand density, receptor density, and nanoparticle size on cell targeting. *Nanomedicine 9*, 194–201.
(71) Shoffstall, A. J., Everhart, L. M., Varley, M. E., Soehnlen, E. S., Shick, A. M., Ustin, J. S., and Lavik, E. B. (2013) Tuning ligand density on intravenous hemostatic nanoparticles dramatically increases survival following blunt trauma. *Biomacromolecules 14*, 2790–2797.
(72) Coller, B. S., Kutok, J. L., Scudder, L. E., Galanakis, D. K., West, S. M., Rudomen, G. S., and Springer, K. T. (1993) Studies of Activated

GPllb / llla Receptors on the Luminal Surface of Adherent Platelets Paradoxical Loss of Luminal Receptors When Platelets Adhere to High Density Fibrinogen *92*, 2796–2806.
(73) Grannis, G. F. (1970) Plasma fibrinogen: determination, normal values, physiopathologic shifts, and fluctuations. *Clin Chem 16*, 486–494.
(74) Lord, S. T. (2007) Fibrinogen and fibrin: scaffold proteins in hemostasis. *Curr Opin Hematol 14*, 236–241.
(75) Blombäck, B., Carlsson, K., Fatah, K., Hessel, B., and Procyk, R. (1994) Fibrin in human plasma: Gel architectures governed by rate and nature of fibrinogen activation. *Thromb. Res. 75*, 521–538.
(76) Wolberg, A. S. (2007) Thrombin generation and fibrin clot structure. *Blood Rev. 21*, 131–142.
(77) Brummel-Ziedins, K. E., Branda, R. F., Butenas, S., and Mann, K. G. (2009) Discordant fibrin formation in hemophilia. *J. Thromb. Haemost. 7*, 825–832.
(78) Lord, S. T. (2011) Molecular mechanisms affecting fibrin structure and stability. *Arterioscler. Thromb. Vasc. Biol. 31*, 494–499.
(79) Lorand, L., Parameswaran, K. N., and Murthy, S. N. (1998) A double-headed Gly-Pro-Arg-Pro ligand mimics the functions of the E domain of fibrin for promoting the end-to-end crosslinking of gamma chains by factor XIIIa. *Proc Natl Acad Sci U S A 95*, 537–541.
(80) Laudano, A. P., and Doolittle, R. F. (1978) Synthetic peptide derivatives that bind to fibrinogen and prevent the polymerization of fibrin monomers. *Proc Natl Acad Sci U S A 75*, 3085–3089.
(81) Everse, S. J., Spraggon, G., Veerapandian, L., Riley, M., and Doolittle, R. F. (1998) Articles Crystal Structure of Fragment Double-D from Human Fibrin with Two Different. *Biochemistry 2960*, 8637–8642.
(82) Soon, A. S., Lee, C. S., and Barker, T. H. (2011) Modulation of fibrin matrix properties via knob:hole affinity interactions using peptide-PEG conjugates. *Biomaterials 32*, 4406–4414.
(83) Stabenfeldt, S. E., Aboujamous, N. M., Soon, A. S., and Barker, T. H. (2011) A new direction for anticoagulants: Inhibiting fibrin assembly with PEGylated fibrin knob mimics. *Biotechnol Bioeng 108*, 2424–33.
(84) Kolodziej, A. F., Nair, S. A., Graham, P., McMurry, T. J., Ladner, R. C., Wescott, C., Sexton, D. J., and Caravan, P. (2012) Fibrin specific peptides derived by phage display: characterization of peptides and conjugates for imaging. *Bioconjug Chem 23*, 548–556.
(85) Kolodziej, A. F., Zhang, Z., Overoye-Chan, K., Jacques, V., and Caravan, P. (2014) Peptide optimization and conjugation strategies in the development of molecularly targeted magnetic resonance imaging contrast agents. *Methods Mol Biol 1088*, 185–211.
(86) Vymazal, J., Spuentrup, E., Cardenas-Molina, G., Wiethoff, A. J., Hartmann, M. G., Caravan, P., and Parsons Jr., E. C. (2009)

Thrombus imaging with fibrin-specific gadolinium-based MR contrast agent EP-2104R: results of a phase II clinical study of feasibility. *Invest Radiol 44*, 697–704.

(87) Overoye-Chan, K., Koerner, S., Looby, R. J., Kolodziej, A. F., Zech, S. G., Deng, Q., Chasse, J. M., McMurry, T. J., and Caravan, P. (2008) EP-2104R: a fibrin-specific gadolinium-Based MRI contrast agent for detection of thrombus. *J Am Chem Soc 130*, 6025–6039.

(88) Chan, L. W., Wang, X., Wei, H., Pozzo, L. D., White, N. J., and Pun, S. H. (2015) A Synthetic Fibrin-Crosslinking Polymer for Modulating Clot Properties and Inducing Hemostasis. *Sci. Transl. Med. 7*, 277ra29.

(89) Brohi, K., Singh, J., Heron, M., and Coats, T. (2003) Acute traumatic coagulopathy. *J Trauma 54*, 1127–1130.

(90) Raza, I., Davenport, R., Rourke, C., Platton, S., Manson, J., Spoors, C., Khan, S., De'Ath, H. D., Allard, S., Hart, D. P., et al. (2013) The incidence and magnitude of fibrinolytic activation in trauma patients. *J Thromb Haemost 11*, 307–314.

(91) Brown, A. C., Stabenfeldt, S. E., Ahn, B., Hannan, R. T., Dhada, K. S., Herman, E. S., Stefanelli, V., Guzzetta, N., Alexeev, A., Lam, W. A., et al. (2014) Ultrasoft microgels displaying emergent platelet-like behaviours. *Nat Mater 13*, 1108–14.

(92) Osdoit, S., and Rosa, J. P. (2001) Fibrin Clot Retraction by Human Platelets Correlates with α IIbβ3 Integrin-dependent Protein Tyrosine Dephosphorylation. *J. Biol. Chem. 276*, 6703–6710.

(93) Teramura, Y., Okamura, Y., Takeoka, S., Tsuchiyama, H., Narumi, H., Kainoh, M., Handa, M., Ikeda, Y., and Tsuchida, E. (2003) Hemostatic effects of polymerized albumin particles bearing rGPIa/IIa in thrombocytopenic mice. *Biochem Biophys Res Commun 306*, 256–260.

Chapter 2

A SYNTHETIC FIBRIN CROSS-LINKING POLYMER FOR MODULATING CLOT PROPERTIES AND INDUCING HEMOSTASIS

Leslie W. Chan, Xu Wang, Hua Wei, Lilo D. Pozzo,
Nathan J. White, Suzie H. Pun

Abstract

Clotting factor replacement is the standard management of acute bleeding in congenital and acquired bleeding disorders. We present a synthetic approach to hemostasis using an engineered hemostatic polymer (PolySTAT) that circulates innocuously in the blood, identifies sites of vascular injury, and promotes clot formation to stop bleeding. PolySTAT induces hemostasis by crosslinking the fibrin matrix within clots, mimicking the function of the transglutaminase Factor XIII. Furthermore, synthetic PolySTAT binds specifically to fibrin monomers and is uniformly integrated into fibrin fibers during fibrin polymerization, resulting in a fortified, hybrid polymer network with enhanced resistance to enzymatic degradation. *In vivo* hemostatic activity was confirmed in a rat model of trauma and fluid resuscitation in which intravenous administration of PolySTAT improved survival by reducing blood loss and resuscitation fluid requirements. PolySTAT-induced fibrin crosslinking is a novel approach to hemostasis utilizing synthetic polymers for non-invasive modulation of clot architecture with potentially wide-ranging therapeutic applications.

This chapter was published in *Science Translational Medicine*, **7**, 277ra29.

2.1 Introduction

Bleeding is responsible for 30-40% of trauma-associated deaths and is the leading cause of death in the initial hours after injury *(1)*. The formation of stable blood clots, or hemostasis, after severe injury is necessary to prevent major blood loss and death from hemorrhagic shock. Clots are formed initially by a platelet plug that is then reinforced by a fibrin fiber network. However, the depletion and rapid consumption of functional circulating clotting factors after large volume blood loss prevents the formation of robust fibrin networks *(2, 3)*. Furthermore, activation of profibrinolytic pathways causes accelerated breakdown of fibrin matrices, or hyperfibrinolysis *(4)*. The resulting clots are therefore weak and insufficient to stop bleeding. This acquired coagulopathy, known as trauma-induced coagulopathy (TIC), is observed in 25% of trauma patients *(2)* and is associated with increased mortality *(3)*. Therefore, methods to augment or restore hemostatic function are needed to prevent hemorrhage-related deaths.

Although there are several well-established topical hemostatic agents used to resolve bleeding in external injuries (e.g. pressure dressings, gel sealants) *(5)*, there are few examples of systemically administered hemostatic agents to stop bleeding in non-compressible internal injuries. Factor replacement by transfusion of blood components (i.e. fresh frozen plasma, fibrinogen concentrate) or recombinant proteins is the standard approach to restoring hemostatic function *(6)*. However, blood components are costly, have special storage requirements and limited shelf-life, and carry risk of immunogenicity or viral transmission *(7)*. Therefore, there is a critical unmet need for intravenously administered hemostatic agents that can reach distant inaccessible bleeding sites and bolster clot formation after traumic injury, without the aforementioned complications.

In the past decade, several synthetic platelet platforms have been reported to induce faster blood clotting after intravenous injection. Notable examples include poly(lactic-co-glycolic acid)–poly-L-lysine–poly(ethylene

glycol)–[Arg-Gly-Asp] (PLGA-PLL-PEG-RGD) nanoparticles that interact with platelet integrin GPIIb-IIIa to induce platelet aggregation *(8)* and peptide-modified liposomes that mimic platelet adhesion, aggregation, and activation *(9–12)*. However, a challenge with nanoparticle-based approaches is their rapid clearance by the reticuloendothelial system *(13)*. Furthermore, the focus on platelet substitutes leaves the clot's fibrin compartment largely ignored. A fibrin-targeted approach to hemostasis acting downstream of initial platelet plug formation may provide a safer alternative to platelet substitutes to avoid undesired thrombotic events.

Fibrin is a viscoelastic biopolymer produced at the site of vascular injury by the coagulation cascade. Locally activated thrombin enzyme cleaves circulating fibrinogen to form fibrin monomers. Fibrin monomers self-polymerize in a half-staggered, double-stranded manner to form protofibrils, which then associate non-covalently, bundle into fibers, and branch to form a three-dimensional insoluble hydrogel scaffold for platelets, blood cells, and other clot components *(14)*. The transglutaminase Factor XIIIa (FXIIIa) then stabilizes the clot by creating intra- and inter-fiber crosslinks through amide bond formation between lysine and glutamic acid residues. FXIIIa supplementation has been shown to produce fibrin networks with thinner fiber diameters, greater fiber density, and smaller pores for a given fibrinogen concentration than fibrin not supplemented with FXIIIa *(15, 16)*. These architectural changes contribute to increased clot stiffness and resistance to fibrinolysis.

Drawing inspiration from FXIIIa, we engineered a synthetic hemostatic polymer, PolySTAT, that stabilizes blood clots through fibrin crosslinking. Although FXIII crosslinks fibrin via covalent bond formation, we hypothesized that similar clot-stabilizing effects could be achieved using a polymer forming multiple non-covalent bonds to adjacent fibrin monomers. Moreover, the incorporation of synthetic polymers resistant to degradation by the plasmin enzyme would inhibit fibrinolysis. When evaluated *in vitro*

under coagulopathic and hyperfibrinolytic conditions, PolySTAT accelerated clotting kinetics, increased clot strength, and delayed clot breakdown. Intravenous administration of PolySTAT in rats before and after femoral artery injury reduced blood loss, improved tissue perfusion with reduced fluid resuscitation requirements, and significantly improved survival rates, thus demonstrating the hemostatic function of PolySTAT and its potential for clinical translation.

2.2 Materials and methods

2.2.1 Synthesis and characterization of hemostatic polymers (PolySTAT) and scrambled polymer controls (PolySCRAM)

All materials for poly(HEMA) backbone (pHB) synthesis were purchased from Sigma-Aldrich. pHB with a target composition of 80% (hydroxyethyl) methacrylate (HEMA) and 20% *N*-hydroxysuccinimide methacrylate (NHSMA) was synthesized using RAFT polymerization. For a typical synthesis, 310 μL HEMA (2.56 mmol), 117.2 mg NHSMA (0.640 mmol), 1 mL 2,2'-azobis(isobutyronitrile) (AIBN) (0.876 mg/ml in dimethylacetamide, 0.0053 mmol), and 4.47 mg 4-cyanopentanoic acid dithiobenzoate (CPADB) (0.016 mmol) were dissolved in a 5-mL reaction vessel with 3.02 mL dimethylacetamide (DMAc) for a final monomer concentration of 0.6 M. The reaction mixture was purged with argon for 10 minutes and reacted under stirring conditions at 70°C for 24 hr. Fluorescent hemostatic polymer (fPolySTAT) and scrambled polymer control (fPolySCRAM) were synthesized by altering the composition of pHB to 78% HEMA and 2% fluorescein O-methacrylate and maintaining 20% NHSMA. Polymers were precipitated in ether, dissolved in DMAc, and reprecipitated in ether to remove unreacted monomers. Polymers were then dried and stored in a vacuum-sealed oven. Dithiobenzoate groups were removed in a subsequent reaction with a 20:1 molar ratio of AIBN to polymer. Transition of the solution from pink to clear was a positive indicator that the endcapping reaction was near or at

completion. Degree of polymerization and monomer composition were determined using H^1 NMR, and polydispersity and molecular weight were measured using GPC. The absence of CTA peaks on H^1 NMR was used to confirm removal of dithiobenzoate groups. Fibrin-binding peptides with the sequence Ac-Y(DGl)C(HPr)YGLCYIQGK and a scrambled peptide sequence Ac-YICGQ(DGl)AC(HPr)LYGK with the same modifications were purchased from GL Biochem at >95% purity. Fibrin-binding peptides were conjugated to NHS reactive groups on pHB via the ε-amine on the C-terminus lysine under organic basic reaction conditions as reported by Yanjarappa et al. *(38)*. Scrambled peptides were conjugated to NHS groups on pHB for the scrambled polymer control. After 24 h, reaction solutions were transferred to snakeskin dialysis tubing with 10kDa MWCO and dialyzed against PBS for 2 days to remove free peptide. Polymers were then dialyzed against DI water for 2 days to remove salts from the PBS and lyophilized. The number of peptides per polymer was determined by measuring absorption at 280 nm using a Nanodrop 2000 UV-vis spectrophotomer.

2.2.2 Confocal imaging of pure fibrin clots to show co-localization of hemostatic polymers and fibrin

Fibrin clots were prepared in chambered coverslips using 0.5 mL clotting solution with the following final concentrations: 3 mg/ml fibrinogen spiked with 1% Alexa Fluor 546-labeled fibrinogen (Life Technologies F13192), 0.167 IU/mL thrombin, 10 μM $CaCl_2$, and 5 μM fluorescent PolySTAT, 5 μM fluorescent PolySCRAM, or an equal volume of PBS. After 1 hr, clots were imaged with a Zeiss LSM 510 inverted confocal microscope using a 63x objective lens. Lasers with 488 nm and 543 nm wavelength were used to excite polymers and fibrinogen, respectively. BP 505-530 and LP 560 were used to isolate signal from polymers and fibrinogen, respectively. To prevent bleed-through, only one laser was turned on at a time during image acquisition. Image overlays were completed in ImageJ.

2.2.3 Turbidity studies

Clots were formed in a 96-well plate using 100 µl of clotting solution containing 1.5, 2.2, or 3.0 mg/ml plasminogen-depleted fibrinogen ((Enzyme Research Laboratories FIB 1)), 0.167 IU/mL thrombin, and 10 mM $CaCl_2$ with 5 µM PolySTAT, 5 µM PolySCRAM, 10 µg/ml hFXIIIa, or an equal volume of PBS. Turbidity (absorbance at 350 nm) was measured every minute for 40 minutes using a Tecan Infinite M1000 platereader. Turbidity curves were averaged for each treatment ($n = 3$).

2.2.4 Clot permeation studies for determination of pore size

Permeation studies were completed as previously described in literature *(39)*. Fibrin clots were formed in 3-ml syringe barrels using 1 ml solution containing 3 mg/ml FXIII-depleted fibrinogen (Enzyme Research Laboratories P1 FIB), 0.167 IU/ml thrombin, and 10 mM $CaCl_2$ in HEPES-NaCl buffer with PBS, 5 µM PolySCRAM, 5 µM PolySTAT, or 10 µg/ml hFXIIIa (Enzyme Research Laboratories HFXIIIa 1314). Clots were allowed to form for 1 hour after which they were connected via ¾" inner diameter tubing to a 50-mL syringe barrel filled with water and elevated 27 cm from the benchtop. Volumetric flow rate was measured and pore size calculated using Darcy's Law and a model for pore radius by Carr and Hardin *(40)*

$$\text{Darcy's Law, } Da = \frac{V\eta h}{AtP}$$

$$\text{Carr and Hardin, } R_P = \frac{0.5093}{Da^{-1/2}}$$

where V is volumetric flow rate, η is the viscosity of water, h is length of the clot, A is the cross-sectional area, t is time, $P$is pressure, and R_P is the pore radius.

2.2.5 SEM imaging of pure fibrin clots

Fibrin clots were prepared in 24-well plates using 0.5 mL clotting solution with the following final concentrations: 3 mg/ml fibrinogen, 0.167 IU/ml

thrombin, 10 μM $CaCl_2$, and 5 μM PolySTAT, 5 μM PolySCRAM, 10 μg/ml hFXIIIa, or an equal volume of PBS. After 1 hr, clots were fixed in 2.5% glutaraldehyde in DI water for 1 h. Clots were then washed 5 times (5 min per wash) in DI water and dehydrated in increasing percentages of alcohol (25, 50, 75, 100, 100% ethanol, 10 min per ethanol percentage). Samples were chemically dried by immersion in 1:3 volume ratio of hexamethyldisilazane to ethanol for 15 min and subsequently in pure hexamethyldisilazane for 15 min. Finally, samples were placed on filter paper and dried overnight in a chemical hood.

2.2.6 Cone-and-plate rheometry studies

Mechanical stiffness of pure fibrin gels made from clotting solutions containing 1.5, 2.2, and 3.0 mg/mL fibrinogen mixed with PBS, PolySCRAM, or PolySTAT was measured using an Anton Paar MCR 301 rheometer with cone-and-plate configuration (25-mm, 1˚ angle). Storage and loss moduli were measured under 0.1% strain oscillations at 1 Hz for 2000 s. Temperature was maintained at 37˚C using a peltier heat exchanger.

2.2.7 In vitro evaluation of PolySTAT using thromboelastography

In a typical TEG experiment, a 360-μL clotting solution is added to a cup in a TEG 5000 Thromboelastograph Hemostasis Analyzer system. A pin attached to a torsion wire is submerged into the center of the cup. When the device is started, the cup oscillates around the stationary pin and as the clot forms, the movement of the pin becomes coupled with the cup. The amplitude of oscillatory motion of the pin, which is directly proportional to clot strength, is measured over time. Other measures that can be extracted from TEG traces include clot onset time (R), clotting rate (α-angle in degrees), maximum clot strength (maximal amplitude in mm, MA), and the extent of lysis 30 minutes after the time to MA (ly30%). PolySTAT, PolySCRAM, pHB stock solutions were made at 250 μM and free peptide stock solution at 4 mM. 7.2 μL

volumes were added to clotting solutions for final concentrations of 5 μM and equivalent peptide concentration. For purified fibrin systems, the clotting solution had final concentrations of 1.5 mg/ml plasminogen-depleted fibrinogen, 0.5 IU/mL thrombin (Stago Fibri Prest Automate 5) , 2 μg/ml plasmin (Enzyme Research Laboratories) , and 10 mM $CaCl_2$ in pH 7.4 NaCl-HEPES buffer (44 mM HEPES, 2 mM $CaCl_2$, 140 mM NaCl). Fibrinogen was added to the enzymes and $CaCl_2$ immediately before each TEG run. For evaluation in hemodilutions, citrated fresh human blood was diluted at 1:1, 1:2, and 1:3 parts blood to 0.9% saline. 333 μL of Hemodilutions was mixed with 20 μL 0.2M $CaCl_2$ solution and 7.2 μL volumes of PolySTAT or controls.

2.2.8 Movie acquisition for lysing fibrin clots

Clots were formed as described for confocal co-localization studies. Time series of lysing clots were taken using only the fibrin channel. A 10 μg/ml plasmin solution was placed at the edge of fibrin clots, and time-lapsed images were taken every 10 seconds to track clot degradation. ImageJ was used to set movies to 10 fps (100x faster than actual speed).

2.2.9 Study design

Hemostatic polymers were administered intravenously in a rat femoral artery injury model to determine hemostatic efficacy *in vivo*. The protocol was approved by the University of Washington Institutional Animal Care and Use Committee (IACUC). For a power of 0.8 and significance value of 0.5, 5 rats were needed per treatment group. The treatment groups include rats intravenously injected with a volume control (0.9% saline), PolySTAT, PolySCRAM, hFXIIIa, and rat albumin. Rat albumin, which has comparable molecular weight to PolySTAT and PolySCRAM, was used as a control for changes in oncotic pressure due to polymer circulation. The following measurements were taken before and after injury to monitor the condition of the rat and performance of the polymers: blood pressure collected

continuously via a transducer connected to a catheter and BIOPAC unit, lactic acid concentration in sampled blood using a radiometer, blood loss by collection with pre-weighed gauze, and saline infusion volumes recorded from the syringe pump. Surgical procedures, control/polymer injection, radiometer measurements, blood collection, and saline infusion were completed by a researcher blinded to the treatment. Blinding was ensured by a second researcher who prepared controls and hemostatic polymer solutions in randomized order. Measurements were recited by the blinded researcher to the second researcher who would record values under a numerical-alphabetical identification number assigned to each rat. Rats with high baseline lactic acid concentrations (> 1.0 mM) and rats experiencing apnea that could not be revived by chest compressions before the 10 min timepoint were excluded from studies. The endpoint of studies was reached when blood pressure dropped below 20 mmHg, at which point rats were euthanized with an overdose of pentobarbital. Data were compiled and sent to a third researcher for statistical analysis.

2.2.10 Hemostasis in a rat femoral artery injury and fluid resuscitation model

Sprague Dawley rats weighing 310-360g were randomized into one of five treatment groups (volume control, PolySTAT, PolySCRAM, rat albumin, or human Factor XIIIa). Rats were anesthetized using isoflurane and 0.1 mL ketamine-xylazine cocktail (87.5 mg/ml ketamine, 12.5 mg/ml xylazine) injection in the hindlimb. The carotid artery and jugular vein were catheterized for monitoring of blood pressure and for intravenous injection of polymers, respectively. Blood gas and metabolite measurements were completed to confirm that baseline respiration and lactate levels were within acceptable ranges (carbon dioxide, < 55 mmHg; O_2 saturation, > 95%; lactate, <1.0 mM).

Once normal respiration and lactate levels were established, the femoral artery in the left leg was isolated and microsurgical clamps were placed

proximally and distally to prevent bleeding from a 3-mm longitudinal incision made after clamping. Controlled catheter bleeds were then completed via the arterial line to normalize all starting blood pressures to 40-50 mmHg. Immediately following catheter bleeds, clamps were removed from the femoral artery (t = 0 min), and the wound was allowed to bleed freely or clot without interference for 15 min. Immediately after clamp release, PolySTAT, PolySCRAM, or rat albumin in a 10 mg/ml solution was administered over 1.5 minutes at a dose of 15 mg/kg. hFXIIIa was administered at 1.92 mg/ml for an initial circulating concentration of 30 μg/ml, a dose shown to have crosslinking effects *in vitro* in TEG studies. For t > 15 min, fluid resuscitation in the form of saline infusion at 3 mL/min/kg was used to restore and maintain BP above 60 mmHg. Infusion volumes were capped at 60 mL/kg.

Arterial lines for blood pressure monitoring were flushed when waveforms were dampened from clot formation in the line which occurred sporadically when blood pressure was low. Blood gas measurements were taken before femoral artery injury (baseline), right after the free bleeding phase (t = 15 min), during the fluid resuscitation phase (t = 30), and at the protocol endpoint if the animal survived (t = 75 min) to monitor blood pH, gas levels, ion concentrations, and lactate concentration. Blood adjacent to the wound was collected by the blinded researcher using pre-weighed gauze to track blood loss over time. Care was taken to not touch or otherwise disturb the vessel or the forming clot.

2.2.11 Biodistribution studies

Radiolabeled PolySTAT was synthesized by mixing in tritiated glycine (Perkin Elmer) to fibrin-binding peptides for conjugation to p(HEMA-co-NHSMA) copolymers (1 glycine for every 200 PolySTAT). Rats were anesthetized using isoflurane and ketamine-xylazine cocktail injection in the hindlimb. 15 mg/kg radiolabeled PolySTAT was administered via tail-vein injection. At the desired timepoints (5 min, 10 min, 20 min, 1 hr, and 1 day),

the thoracic cavity was opened and blood was collected from the right atrium of the heart using a syringe. Rats were then perfused, and organs were rinsed, weighed, and homogenized. Tissue homogenates were solubilized using Solvable (Perkin Elmer) for 2 hours at 50˚C and decolorized for 4-6 hours by addition of 30% (v/v) hydrogen peroxide and 100 mM EDTA solution to prevent bubbling. 20 µL 10 N HCl and 10 mL Ultima Gold (Perkin Elmer) was then added and samples were shaken vigorously and allowed to sit overnight before reading in a scintillation counter.

2.2.12 Metabolic and hepatic function panels

Rats were injected with 15 mg/kg PolySTAT. 1 h, 1 day, and 1 week, 2 ml blood was collected and added to 200 µL sodium heparin to prevent clotting (n = 3). Plasma was collected after centrifuging heparinized blood for 15 min at 2000 rcf and submitted to the University of Washington Research Testing Services at the UW Medical Center for comprehensive metabolic and hepatic function panels. Creatinine levels were analyzed for kidney toxicity, and albumin, bilirubin, and enzymes (AST, aspartate aminotransferase; alkaline phosphatase; ALT, alanine aminotransferase) were analyzed for liver toxicity. Plasma from untreated rats was submitted to identify normal creatinine and enzyme ranges (n = 5).

2.2.13 Statistical analysis

One-way ANOVAs with Tukey Kramer post hoc tests were completed on data from TEG studies and animal studies (hemorrhage volume, saline infusion rate) using GraphPad Prism 5 and JMP statistical software to determine significance and calculate p-values. Differences between groups were considered statistically significant when $p < 0.05$. Two-way ANOVAs were completed for comparison of MAP and lactate concentrations between volume controls and animals receiving PolySTAT. A log-rank Mantel-Cox test was completed to determine significance of survival data for in vivo studies.

2.3 Results

2.3.1 Design of fibrin-crosslinking hemostatic polymers (PolySTAT)

We designed a synthetic polymer to mimic FXIIIa-mediated fibrin stabilization by displaying multiple fibrin-binding domains on a linear water-soluble (hydroxyethyl)methacrylate (HEMA) and *N*-hydroxysuccinimide methacrylate (NHSMA) polymer backbone [p(HEMA-*co*-NHSMA)] (Fig. 2.1A). This approach allowed for fibrin crosslinking to increase clot stiffness and incorporation of synthetic polymers resistant to plasmin degradation. For safe, *in situ* fibrin crosslinking after intravenous administration, hemostatic polymers must demonstrate high specificity for fibrin to prevent nonspecific binding to soluble fibrinogen or other plasma proteins that may lead to thrombotic events, such as stroke or embolism. A cyclic fibrin-specific peptide ($K_{d,\ human}$ = 121 nM), developed by Kolodziej *et al. (17, 18)*, was selected as the fibrin-binding domain owing to its high binding affinity and specificity for fibrin, cross-species reactivity, extensive characterization and sequence optimization for improved binding affinity and serum stability, and previous use in humans (Fig. 2.1A).

Poly(HEMA) has been used clinically in implants *(19)* and was copolymerized here with the NHSMA monomer via reversible addition-fragmentation chain-transfer (RAFT) to provide sites for peptide grafting. This monomer ratio was chosen to be able to graft several peptides (expected conjugation efficiency of ~50%) to the polymer backbone without experiencing solubility issues from 20% NHSMA content. The degree of polymerization (DP) was 200, with a targeted molecular weight nearing the upper end of the renal threshold after peptide conjugation to prevent rapid clearance after intravenous administration *(20)*.

Peptide conjugation efficiencies were approximately 40%, resulting in 16 peptides per polymer. Multivalency enhances affinity of the polymer to fibrin owing to avidity effects *(21)* and, in this instance, is also expected to facilitate fibrin crosslinking. Fluorescent analogues of PolySTAT and PolySCRAM

(fPolySTAT and fPolySCRAM, respectively) with 2% fluorescein methacrylate (FMA) in the polymer backbone were synthesized for imaging and contained comparable peptide content (35-45% conjugation efficiency) (Fig. 2.1B).

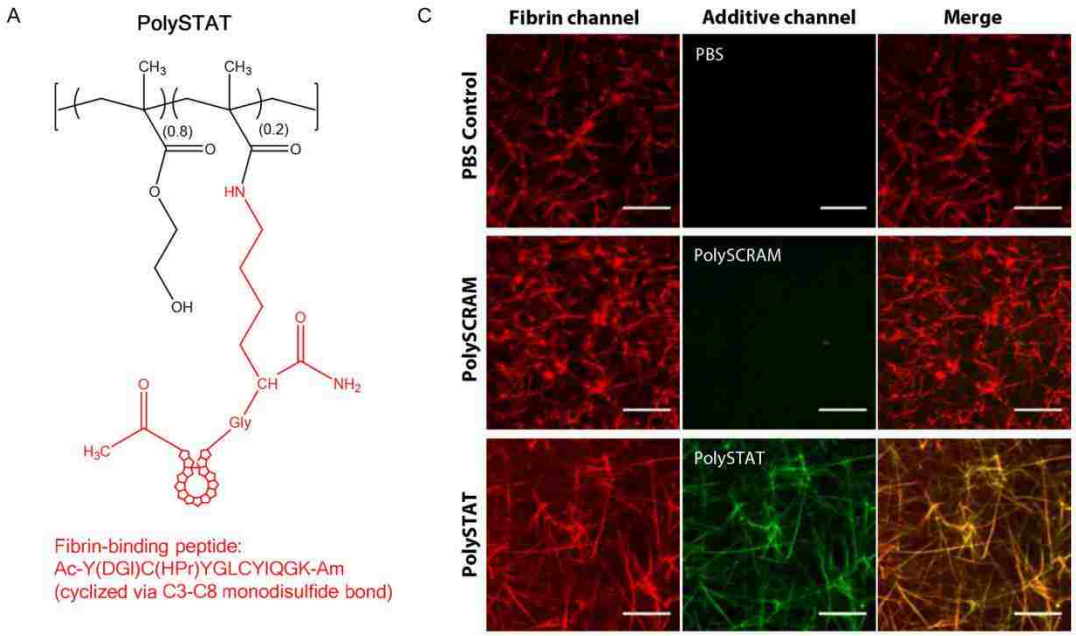

B

Polymer	Theoretical MW	Actual MW	PDI	Peptides per polymer	Conjugation efficiency (%)
$p(HEMA_{160}\text{-}co\text{-}NHSMA_{40})$	2.82×10^4	2.95×10^4	1.43	NA	
HP	NA	**4.45×10^4**	**1.24**	**16**	**40**
SCRP	NA	**4.66×10^4**	**1.42**	**16**	**40**
$p(HEMA_{156}\text{-}co\text{-}NHSMA_{40}\text{-}co\text{-}FMA_4)$	2.92×10^4	2.56×10^4	1.24	NA	
fHP	NA	**6.72×10^4**	**1.22**	**14**	**35**
fSCRP	NA	**5.31×10^4**	**1.35**	**18**	**45**

Fig. 2.1. PolySTAT synthesis and characterization. (**A**) The PolySTAT polymer backbone, a linear statistical copolymer of HEMA and NHSMA synthesized via RAFT polymerization, was grafted with the modified cyclic fibrin-binding peptide Ac-Y(DGl)C(HPr)YGLCYIQGK-Am (*19*) through NHS ester reaction with the lysine ε-amine. DGl, D-glutamic acid; HPr, hydroxyproline; Ac, acetylated N-terminus; Am, amidated C-terminus. (**B**) Two different polymer backbones were used, including a fluorescent fluorescein methacrylate (FMA)-modified p(HEMA-*co*-NSHMA) for confocal studies. Polymer backbones were grafted with the fibrin-binding peptide for PolySTAT or a non-binding scrambled peptide for the PolySCRAM control. Actual molecular weight and polydispersity index (PDI) were determined using GPC. Peptides per polymer were calculated using UV absorbance. (**C**) PolySTAT integration into fibrin was confirmed using confocal imaging. Pure fibrin clots were made using a solution of

Alexa Fluor 546-labeled fibrinogen (red) and thrombin mixed with PBS, fPolySTAT (green), or fPolySCRAM (green). Scale bars, 10 μm.

2.3.2 PolySTAT integration and alteration of fibrin clot structure

To confirm the selective integration of PolySTAT into fibrin fibers, fPolySTAT, fPolySCRAM, and PBS were each mixed with fluorescently labelled fibrinogen, and fibrin was formed by adding thrombin prior to confocal imaging. fPolySTAT fluorescence exhibited fiber morphology which coincided with fluorescence from fibrin fibers whereas fPolySCRAM signal showed no distinct morphology (Fig. 2.1C), demonstrating that incorporation of fibrin-specific peptide sequences in PolySTAT is necessary for polymer integration into fibrin networks. Furthermore, fPolySTAT fluorescence was observed throughout fibrin fibers, suggesting that PolySTAT is actively integrated during the polymerization process.

Precursory analysis of fibrin clot structure was completed using turbidity measurements to determine if PolySTAT integration induced changes in fibrin structure (Fig 2.2A). PolySTAT-integrated clots had significantly greater turbidities compared to control clots formed with PBS or PolySCRAM, indicating structural differences in fiber diameter, density, or homogeneity (22). Turbidities of fibrin crosslinked by human Factor XIIIa (hFXIIIa) had significantly lower turbidities compared to control clots, demonstrating that covalent crosslinking by hFXIIIa versus non-covalent crosslinking by PolySTAT result in two very different fibrin architectures.

Permeation studies and SEM imaging were used to further interrogate fibrin structure. Fluid flow through PolySTAT-integrated fibrin clots was noticeably hindered compared to fibrin formed with PBS or PolySCRAM, reflecting 1.5-fold smaller pore radii in PolySTAT clots (Fig. 2.2B). Interestingly, 250 μg/ml (5 μM) PolySTAT (concentration for a minimum of 2 fibrin-binding sites per PolySTAT) created smaller pore sizes than a physiological concentration of 10 μg/ml (63 nM) hFXIIIa. SEM imaging revealed trends in pore size consistent with the permeation study (Fig. 2.2C).

PolySTAT-modified fibrin had smaller pores interspersed throughout a dense fibrin mesh compared to PBS and PolySCRAM controls and hFXIIIa-crosslinked fibrin, which all had distinct, loosely interwoven fibers and larger pore sizes. The denser fibrin structure of PolySTAT would likely cause greater light scattering and account for the greater turbidity observed (Fig. 2.2A).

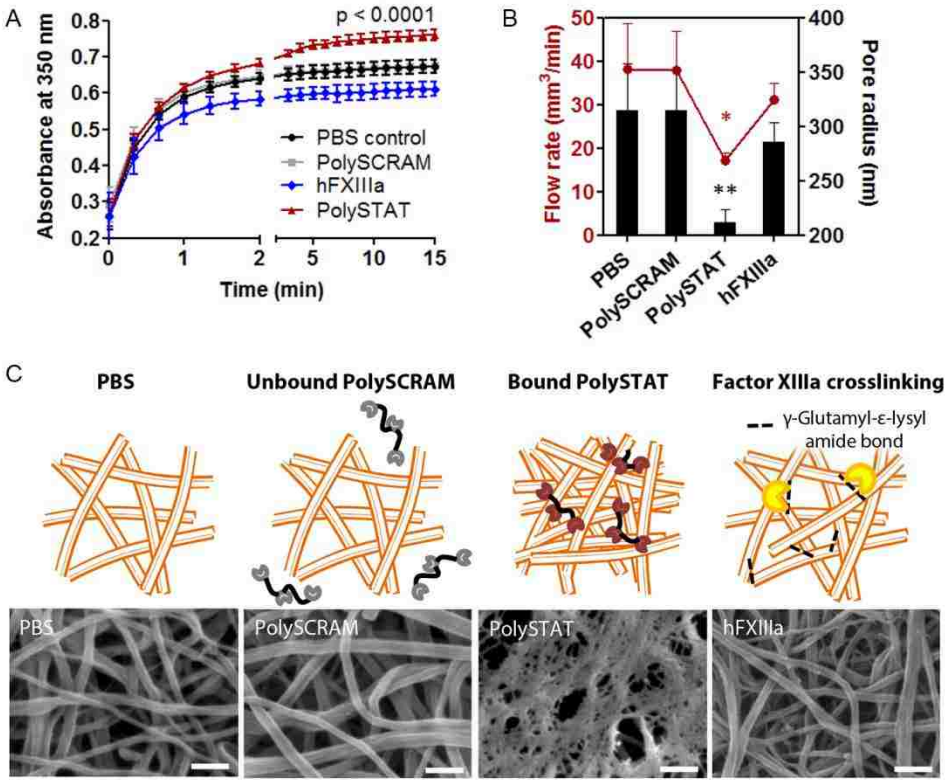

Fig. 2.2. In vitro characterization of PolySTAT-modified fibrin architecture. (**A**) Turbidity of pure fibrin clotting solutions with PBS, PolySCRAM, PolySTAT, and hFXIIIa was measured to determine if there were potential changes in fibrin nanostructure. The *p*-value shown is for comparison between PBS and PolySTAT at t = 15 min. (**B**) Flow rates of water through fully-formed fibrin were measured and used to extrapolate pore size using Darcy's Law and a model by Carr and Hardin (*41*). *P*-values are shown for comparison to PolySCRAM (**p* = 0.03, ***p* = 0.01). Data in (**A** and **B**) are averages ± SD (*n* = 3). Statistical significance was determined using one-way ANOVA with Tukey Kramer post hoc test. (**C**) Fully formed fibrin clots were imaged using scanning electron microscopy to visualize fibrin architecture. hFXIIIa was included for a crosslinking control. Scale bars, 250 nm. Schematics above the SEM images depict the exclusion of non-binding PolySCRAM from fibrin, PolySTAT-induced fibrin

crosslinking via binding of fibrin-binding peptides, and enzymatic crosslinking by hFXIIIa. (Schematics are not drawn to scale.)

2.3.3 PolySTAT modification of fibrin clot strength and fibrinolytic activity

Mortality is dramatically increased in trauma patients when fibrinogen concentrations fall below a critical threshold of 2.29 mg/ml *(23, 24)*. Fibrin clots were formed *in vitro* with fibrinogen concentrations below threshold, at threshold, and at the average physiological concentration above threshold *(25)* (1.5, 2.2, and 3.0 mg/ml fibrinogen, respectively), with and without PolySTAT (5 μM), to determine if clot strength could be rescued through PolySTAT-induced fibrin crosslinking. For each fibrinogen concentration, storage moduli (a measure of clot elasticity) of PolySTAT-modified fibrin clots were 2- to 3-fold greater than those of controls (Fig. 2.3A). At 1.5 mg/ml fibrinogen, PolySTAT-induced crosslinking resulted in storage moduli comparable to those of control clots at the threshold. At 2.2 mg/ml fibrinogen, the storage modulus of PolySTAT-modified fibrin was well above the threshold and greater than storage moduli of controls formed with 3 mg/ml fibrinogen. Thus, reduced clot elasticity owing to fibrinogen depletion was reversed through PolySTAT-induced crosslinking.

Thrombelastography (TEG) is a clinical viscoelastic tool that provides quantitative values for clotting onset time, clotting rate (α-angle), maximum clot strength (maximum amplitude), and, under lysing conditions, percent of clot lysed 30 minutes after time to maximum clot strength (Ly30%). Polymers were tested by TEG in an *in vitro* hyperfibrinolytic system to determine the effects of PolySTAT on clots under the coagulopathic conditions observed in patients after the early stages of severe hemorrhage (Fig. 2.3, B to E, 1.5 mg/ml fibrinogen). In clotting solutions with low fibrinogen concentration, PolySTAT accelerated clot strengthening (earlier clotting onset times and ~20% faster clotting rates), produced a 2-fold increase in clot strength, and reduced Ly30% by 15% compared to PBS and PolySCRAM controls. When

fibrinogen concentration was doubled, clot strength of PolySTAT-integrated clots was 1.5-fold greater than controls, and Ly30% was reduced by 39-57%. Increased clot strength combined with reduced lysis consistently resulted in clots with longer lifetimes.

hFXIIIa was supplemented at three different concentrations previously shown to increase clot strength and inhibit fibrinolysis *(15, 16)* for comparison to PolySTAT activity. hFXIIIa was more effective when there was a greater availability of fibrin (Fig. 2.3, B-E). At 3 mg/ml fibrinogen, a trend of increasing clot strength was observed with increasing hFXIIIa concentration whereas no increased clot strength was observed at 1.5 mg/ml fibrinogen (Fig. 2.3C). Additionally, at the higher fibrinogen concentration hFXIIIa significantly reduced clotting onset time and Ly30% (Fig. 2.3, B and E). PolySTAT reduced lysis to the same extent as 30 μg/ml hFXIIIa and 20 μg/ml hFXIIIa at 1.5 and 3 mg/ml fibrinogen, respectively (Fig 2.3E). In additional TEG studies, PolySTAT-treated clots consistently showed improvement of clot formation and extended clot lifetime over a range of biologically relevant fibrinogen and plasmin concentrations (fig. S2.1). These effects were only induced when the fibrin-binding peptides were conjugated to the HEMA polymer backbone (fig. S2.2). Equivalent concentrations of free peptide, HEMA polymer, and peptide-polymer mixtures did not produce any changes in clot formation.

PolySTAT was further evaluated in diluted whole blood used to mimic dilution effects of fluid resuscitation used to treat hypovolemia after massive blood loss *(26)*. PolySTAT-modified blood clots experienced significantly less lysis than controls (fig. S2.3), suggesting that the PolySTAT would retain its clot-enhancing effects during fluid resuscitation.

Fibrinolysis was next visualized by time-lapsed confocal imaging of polymer-treated fluorescent fibrin clots exposed to plasmin *in vitro*. Images of clots taken at the leading edge at 1-minute intervals are shown in Fig. 2.3F. PolySTAT-integrated fibrin and hFXIII-crosslinked fibrin degraded 3-fold

and 8-fold slower than PBS and PolySCRAM controls (Fig. 2.3F, movies S2.1 to S2.4).

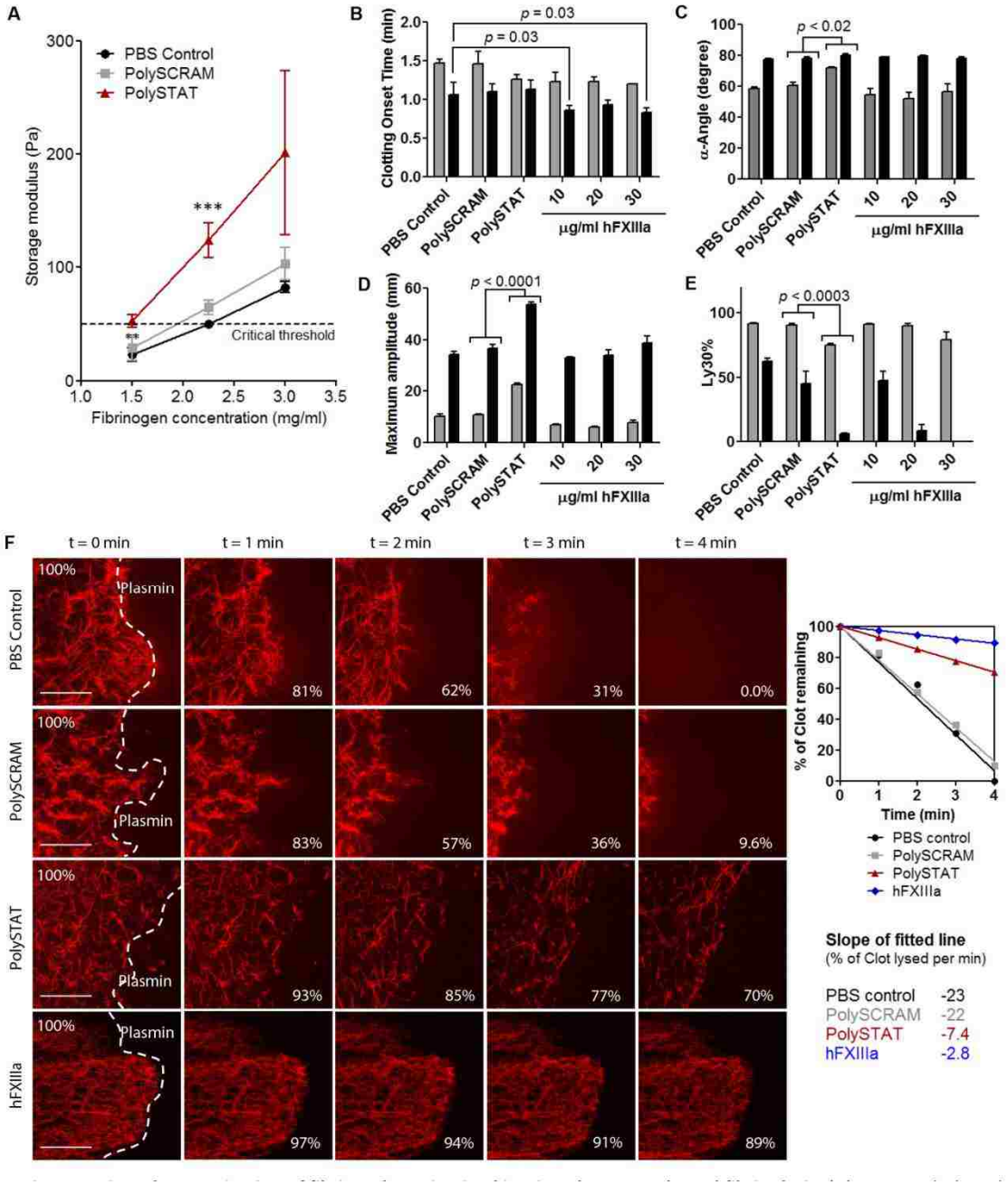

Fig. 2.3. In vitro characterization of fibrin polymerization kinetics, clot strength, and fibrinolysis. (**A**) Cone-and-plate rheometry was used to measure PolySTAT-induced changes in fibrin storage moduli, a measure of elasticity. Measurements were taken for PolySTAT-modfied and control fibrin formed with 1.5, 2.2, and 3.0 mg/ml fibrinogen with intact hFXIIIa (n = 3). The critical threshold indicates the storage moduli below which mortality increases dramatically in trauma patients (*26*). Data are averages ± SD.

***$p < 0.0001$ for both effect of treatment and fibrinogen concentration, $p = 0.07$ for interaction; 2-way ANOVA. The effect of PolySTAT on clotting kinetics, clot strength, and extent of fibrinolysis was evaluated in a hyperfibrinolytic model using TEG. (**B** to **E**) Clotting onset time, clotting rate, maximum clot strength, and extent of clot lysis 30 min after time to maximum clot strength are shown. Three hFXIIIa concentrations were included to compare to PolySTAT activity. Data are averages ± SD ($n = 3$). *P*-values were determined using one-way ANOVA with Tukey Kramer post hoc test. (**F**) Lysis of fibrin was visualized using confocal microscopy. Plasmin (10 μg/ml) was applied to the edge of fully-formed fibrin clots and time-lapsed images were taken. Image processing was used to measure the area of the clot in acquired images and determine rate of clot lysis. Scale bars, 50 μm.

2.3.4 Hemostatic efficacy of PolySTAT in a rat femoral artery injury and fluid resuscitation model

Mechanical strengthening of clots is necessary for more effective fluid resuscitation without further blood loss induced by increasing blood pressure. To evaluate the effect of PolySTAT on clot formation *in vivo*, PolySTAT and controls were administered in a rat model of femoral artery injury and fluid resuscitation (Fig. 2.4A). In this model, polymer solution was injected intravenously in rats immediately following the onset of bleeding from a 3-mm incision in the femoral artery. During the first 15 min, the wound was allowed to bleed or clot without interference (free bleeding). After 15 min, saline was infused at a fixed rate of 3 ml/kg/min, when needed, to recover and maintain BP above 60 mmHg (fluid resuscitation). Blood loss was tracked by collecting blood with pre-weighed gauze. Hemorrhage volumes during fluid resuscitation are indicative of the stability of clots formed during free bleeding. Weaker clots are more susceptible to rebleeding as blood pressure increases and would result in greater blood loss.

Dilutional coagulopathy after fluid resuscitation was confirmed in this model by tracking prothrombin time (PT), plasma fibrinogen concentration, hemorrhage volumes, blood pressure, and blood lactate concentrations in rats injected with a volume control (0.9% saline) to account for effects of bolus fluid administration on bleeding. Prolonged PT, indicating longer clotting

time, is a hallmark of trauma-induced coagulopathy (TIC) in humans and animal models, and rat models of TIC experience precipitous falls in fibrinogen concentration and elevated lactate levels after trauma *(27)*. Lactate, a byproduct of anaerobic respiration, is released into circulation owing to inadequate tissue perfusion and indicates the presence and severity of hemorrhagic shock. Lactate concentration and clearance from the blood are established predictive markers for trauma patient mortality *(28)* and were measured to determine the efficacy of fluid resuscitation. In our model, blood loss from the catheter hemorrhage and free bleeding phase resulted in shortening of PT, a 1.8-fold drop in fibrinogen concentration, and increased lactate levels. All rats required fluid resuscitation after free bleeding. Despite fluid infusion, animals remained hypo-perfused. BPs remained below 60 mmHg and lactate levels continued increasing to 30 min. Saline infusion resulted in prolonged PT compared to baseline values.

Following characterization of the TIC model, rats were injected with PolySTAT, PolySCRAM, rat albumin, or hFXIIIa immediately after bleeding (t=0 min). Polymers and rat albumin were injected at 15 mg/kg, a dose replicating concentrations used *in vitro*. Rat albumin was used to control for changes in intravascular oncotic pressures owing to polymer size. For comparison of *in vivo* efficacy, hFXIIIa was administered at 1.92 mg/kg for an initial circulating concentration of 30 μg/ml, a concentration shown to have comparable or greater lysis-reducing effects as 15 mg/kg PolySTAT in TEG studies. Vital measurements (prothrombin time, fibrinogen, blood pressure, and lactate) for each animal are provided in fig. S2.4-S2.7. All animals (100%, n = 5) treated with PolySTAT following injury survived to the end of protocol whereas 0-40% of animals injected with the volume control, PolySCRAM, albumin, and hFXIIIa survived (Fig. 2.4B). Of the animals surviving the full protocol time (9 of 25), none experienced rebleeding during fluid resuscitation, meaning that clots formed during the free bleeding period were

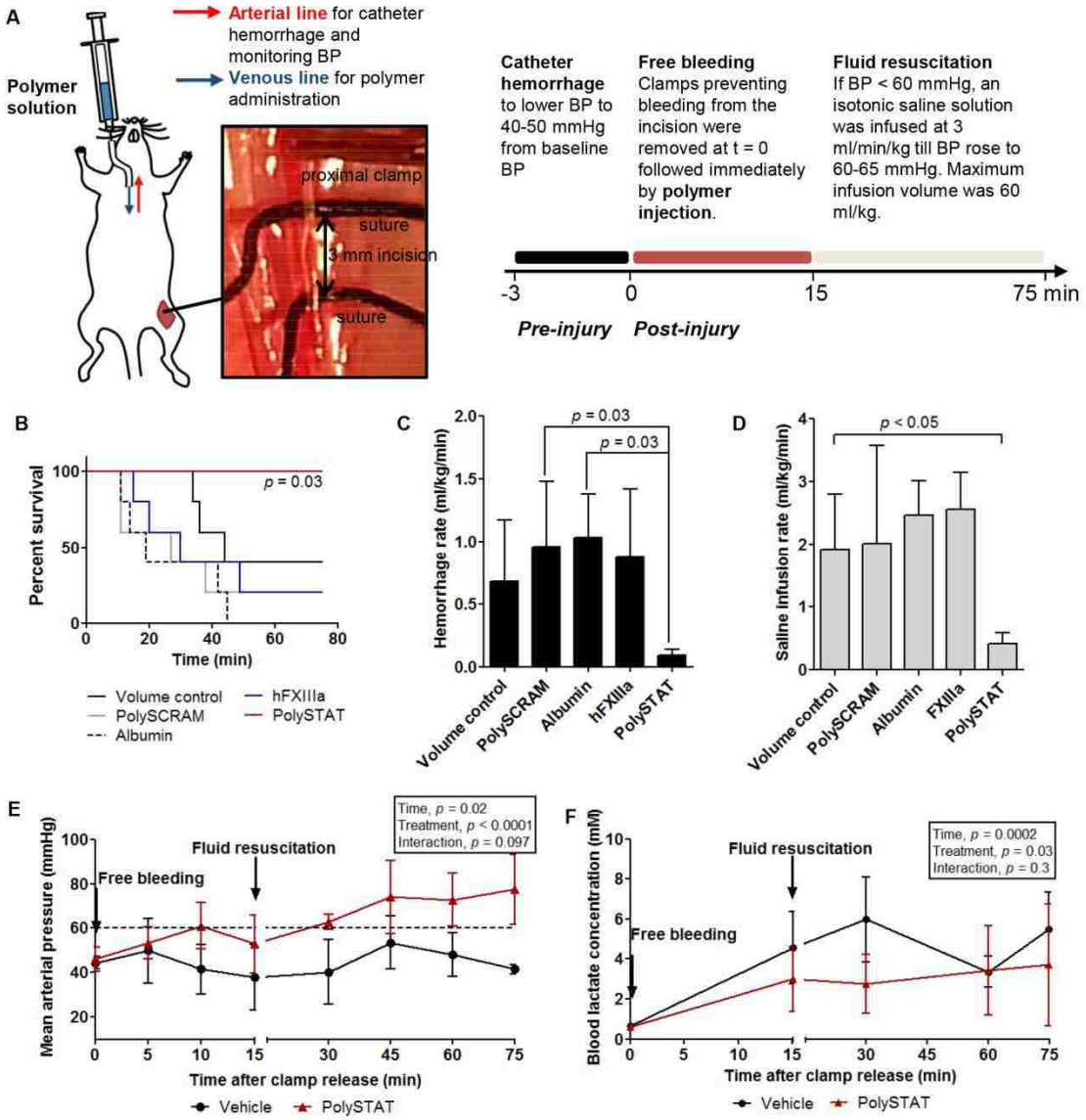

Fig. 2.4. Evaluation of PolySTAT in a rat model of femoral artery injury and fluid resuscitation. (**A**) Workflow schematic. Rats were normalized to the same starting blood pressure, and clamps proximal and distal to the injured femoral artery were removed to allow the wound to bleed freely. Following clamp release, polymer solutions were injected. The wound was allowed to bleed or clot without interference for the first 15 min and subsequent challenge to the clot was presented in the form of 0.9% saline infusion to maintain BP above 60 mmHg for 60 min. (**B**) Survival of animals over the 75-min protocol (n = 5 per treatment). P-value determined using the log-rank Mantel-Cox test. (**C**) Bleeding profiles for volume controls (Vol; 0.9% saline; top) and PolySTAT-treated

animals (bottom) which are representative of clots that experience bleeding during fluid resuscitation and clots that maintain hemostasis during fluid resuscitation, respectively. Data are single measurements per timepoint, per animal (n = 5 per treatment group). (**D**) Cumulative blood loss normalized to survival time, including blood lost during catheter hemorrhage, the free bleeding period, and fluid resuscitation. (**E**) Saline infusion volumes normalized to survival time. Data in (**D** and **E**) are averages ± SD. P-values were determined using a 1-way ANOVA and Tukey Kramer post hoc test. (**F**) Mean arterial pressure was tracked over the protocol time to determine if animals were hypotensive. (**G**) Circulating lactate levels were measured to evaluate tissue perfusion. Data in (**F** and **G**) are averages ± SD with variable n depending on survival times (11-75 min). A two-way ANOVA was used to determine the effect of time and treatment on MAP.

strong enough to withstand increasing blood pressure from saline infusion (Fig. 2.4C).

All PolySTAT-treated animals survived, indicating that PolySTAT is able to assist in forming stronger clots more resistant to rupture. Owing to no incidences of rebleeding (Fig. 2.4C), PolySTAT-treated animals experienced up to 11-fold less blood loss than controls (Fig. 2.4D) and fivefold less saline was needed to maintain BP at 60 mmHg compared with all other treatment groups (Fig. 2.4E). Although volume controls used 97 ± 6% of the maximum allowed infusion volume, PolySTAT-treated animals required only 42 ± 17% of the maximum allowed infusion volume to maintain a BP of 60 mmHg. Lower fluid resuscitation volumes can be attributed to robust clot formation, which prevents the loss of infused volumes from the wound.

Owing to the number of early deaths in PolySCRAM, albumin, and hFXIIIa treatment groups, statistical comparison was completed between PolySTAT and volume controls for comparison of BP and lactate levels. PolySTAT-treated rats had significantly higher blood pressures (mean arterial pressure, MAP) (Fig. 2.4F, fig S2.6) and lower lactate levels (Fig.

S2.7) compared to volume controls , indicating that tissues were better perfused in PolySTAT-treated animals.

2.3.5 Biodistribution of hemostatic polymers

The pharmacokinetics and biodistribution of PolySTAT was determined in healthy rats (Fig. 2.5). Radiolabeled PolySTAT was administered intravenously at the equivalent dose used in femoral artery injury studies (15 mg/kg). Blood was collected at various time points after injection followed by perfusion and organ collection. The initial distribution half-life of PolySTAT was 20 min ($t_{1/2,\alpha}$) and the elimination half-life was 14.4 hr ($t_{1/2,\beta}$) (table S2). Elimination half-life and distribution rate from the central compartment to peripheral compartment (k_{12}, 0.0238 min^{-1}) are similar to reported values for 50-kDa polyethylene glycol (PEG) ($t_{1/2,\alpha}$ of PEG50k = 16.5 h; k_{12} = 0.02 min^{-1}). PEGylation is a technique used to increase circulation times in several FDA-approved biologic drugs.

The majority of PolySTAT (>50%) was cleared from the body within 1 h. The remaining polymer was distributed primarily to the liver (~16% of initial injected dose, I.D.) and kidney (21% of I.D.) (Fig. 2.5A). The amount of PolySTAT accumulation in liver and kidney increased after injection to 1 h but then started to decrease by 24 h, indicating elimination from the body. The slower elimination from kidneys and liver is likely due to low transfer rate from the tissues back into blood (k_{21} ~ 0.003/min; 5.5-fold lower than PEG50k) *(29)*. Normalization of total PolySTAT content to organ mass demonstrated PolySTAT concentrations in the spleen similar to those in the liver (Fig. 2.5B). No PolySTAT accumulated in the heart and lungs at any time. PolySTAT was primarily removed from circulation by renal clearance. Tritium counts for urine collected within the first 30 minutes after injection confirmed elimination by renal filtration (table S2.3).

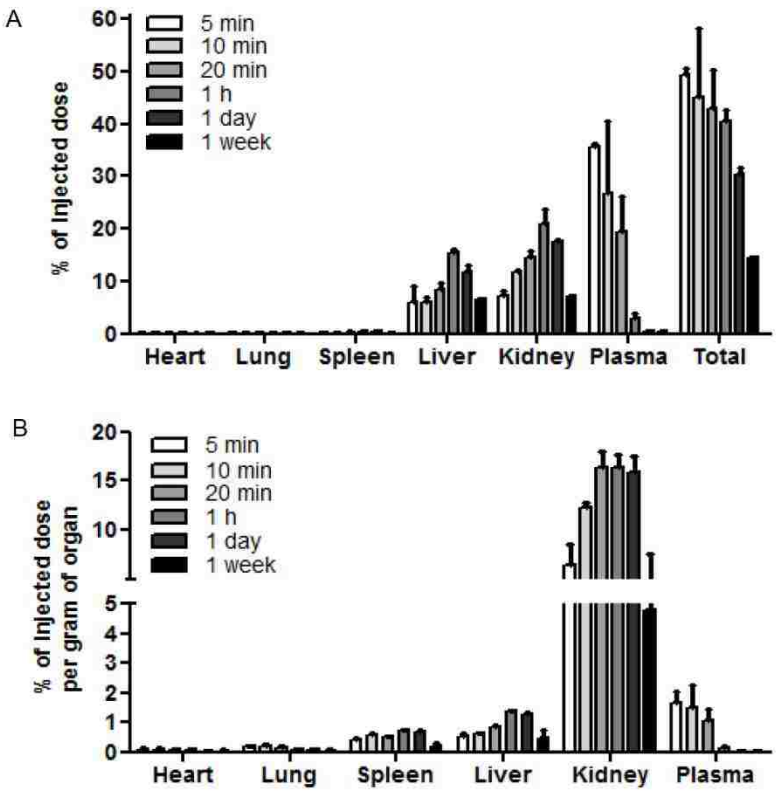

Fig. 5. PolySTAT biodistribution. PolySTAT was administered via tail-vein injection at a dose of 15 mg/kg in rats. Animals were euthanized at various time points to determine polymer biodistribution. (**A**) Percentage of the injected dose in whole organs at various timepoints. (**B**) Percentage of injected dose normalized to organ mass. Data are averages ± SD (n = 3).

Metabolic and hepatic function panels were completed at 1 h, 1 day, and 1 week after PolySTAT injection to assess liver and kidney function (table S2.1). Creatinine levels, used to indicate kidney function, were slightly elevated 1 hour after polymer injection, which is likely due to the monopolization of glomerular filtration by significantly larger PolySTAT. By 1 day after injection, creatinine levels returned to control levels indicating that any effect of the polymer on renal filtration is reversible. Indicators of hepatic function, such as plasma concentrations of albumin and bilirubin, showed no significant changes compared to rats receiving no injection. Liver-associated enzymes alkaline phosphatase and alanine aminotransferase

(ALT) also showed no significant changes in concentration compared to rats receiving no injection. Rats showed no signs of distress post-injection and had healthy weight gain until time of euthanasia. Thus, PolySTAT treatment at clinically relevant doses was well-tolerated in rats.

2.4 Discussion

The goal of this work was to develop a synthetic hemostatic polymer (PolySTAT) that, when administered systemically, would accumulate locally at sites of vascular injury and induce hemostasis. Fibrin-crosslinking occurs naturally *in vivo* by FXIIIa-catalyzed isopeptide bond formation between glutamic acid and lysine residues. Although these crosslinks are covalent in nature, we hypothesized that a synthetic polymer binding non-covalently to adjacent fibrin monomers could recapitulate similar clot-strengthening effects as well as prevent enzymatic breakdown through introduction of plasmin-resistant polymers into fibrin fibers. PolySTAT was synthesized by grafting fibrin-binding peptides onto a linear polymer backbone synthesized by living polymerization. Fibrin fibers contain anywhere from tens to hundreds of double-stranded protofibrils each with up to 25 half-staggered fibrin monomers *(30)*. Therefore, peptide-binding sites are in abundance for PolySTAT activity.

The fibrin-binding peptide used here was previously identified using phage display and was found to have two binding sites per fibrin monomer, which is attributed to the dimeric structure of fibrin *(17, 18)*. Although the binding sites are still unknown, this peptide does not induce fibrinogen self-association and does not inhibit fibrin formation and thus minimizes the possibility of thrombosis or exacerbated bleeding after intravenous injection. Binding of this peptide to fibrin is conserved across multiple species, including humans, pigs, and rats *(31)*, and is therefore opportune for both preclinical development and clinical translation. This peptide has also been shown to selectively accumulate in fibrin-rich thrombi and was well-tolerated

when administered intravenously in humans *(32)*. Given its specificity for fibrin and the extensive optimization and characterization, this fibrin-binding peptide was the ideal targeting ligand for PolySTAT construction.

When mixed into clotting solutions, PolySTAT self-integrated into fibrin fibers and produced dense fibrin meshes with smaller pores. Although this architecture is vastly different from FXIIIa-crosslinked fibrin, similar clot-stabilizing effects were achieved in regard to inhibiting fibrinolysis. TEG studies in which plasmin is present throughout the initial clotting solution suggest the slower rate of fibrinolysis in PolySTAT-integrated fibrin is due to the resistance of the altered fibrin itself to enzymatic breakdown rather than a sole function of limited plasmin diffusion. Inhibition of fibrinolysis allowed PolySTAT-modified fibrin to maintain greater clot strength than PBS and PolySCRAM controls over longer periods of time which is desirable for preventing rebleeding. Futhermore, the ability of PolySTAT to restore clot strength to fibrin formed at fibrinogen concentrations below the critical thresholdsuggests that PolySTAT can be an alternative to fibrinogen concentrates which are currently used in European trauma centers *(33)*. When administered intravenously, PolySTAT improved survival by reducing blood loss and preventing rebleeding during fluid resuscitation in injured rats, thereby maintaining higher BP and minimizing the need for saline infusion. Reduced fluid resuscitation requirements are beneficial as fluid resuscitation is known to exacerbate bleeding due to increased blood pressures as well as dilution of circulating clotting factors *(34)*.

Prior to this work, efforts to develop intravenous hemostats were predominantly focused on synthetic platelet substitutes. Nanoparticles functionalized with peptide ligands for binding subendothelial matrix proteins and surface glycoproteins on platelets have been used to mimic platelet adhesion and aggregation *(8–12)*. Initial platelet plug formation is important for blood clotting. However, as shown here, mechanical and degradative properties of the clot's fibrin compartment can be tuned using

synthetic polymers to prolong clot lifetime and, thus, presents an alternative strategy for inducing hemostasis. Because PolySTAT's mechanism of action targets a different step in the clotting process from synthetic platelets, there are opportunities for these technologies to work synergistically.

In addition, although nanoparticles have been reported to be rapidly sequestered by the reticuloendothelial system (RES) *(35)*, water-soluble polymers show molecular weight-dependent circulation half-lives and reduced RES accumulation compared to nanoparticles *(29)*. As much as 70% of injected doses of systemically administered nanoparticle hemostats accumulate in the liver within the first 10 minutes of circulation and is retained for up to 1 day *(8)*, whereas liver accumulation of PolySTAT was not detected above 23% of the injected dose. Thus, relative to particle systems, higher PolySTAT concentrations are maintained circulating in the blood at earlier timepoints. Longer circulation times combined with rapid activity during fibrin polymerization is advantageous for resolving bleeding during transport of trauma patients to a Level 1 trauma center, which is generally within the hour after injury *(36)*. Pharmacokinetic studies revealed that 7% of PolySTAT remains in kidneys one week after administration, which is likely accumulation of polymer from the larger end of the molecular weight distribution. Future generations of PolySTAT may be synthesized at lower DP to ensure more complete renal clearance.

One of the largest concerns when administering intravenous hemostats is off-target clot formation leading to thrombotic events such as stroke or heart attack. Binding specificity of PolySTAT to fibrin minimizes risk of thrombosis by ensuring that PolySTAT does not bind and crosslink the circulating fibrin precursor (fibrinogen). Thus, the clot is localized at the site of injury. Furthermore, the eventual elimination from circulation as we see with PolySTAT is favorable for preventing thrombosis. PolySTAT-crosslinked clots are expected to be removed during surgical repair of the injury once the patient has been transported to the hospital. However, should PolySTAT-

integrated clots remain in the body, fibrinolysis is simply delayed, not completely eliminated.

For trauma patients surviving the initial 24 hours after injury, the greatest concerns are renal injury, lung injury, and multiple organ failure *(37)*. Therefore, further evaluation is needed to determine if PolySTAT treatment will reduce the extent of organ injury in surviving animals. In addition, pharmacokinetics and evaluation of hemostatic effects in larger animal models such as pig models are necessary before clinical translation.

Acute bleeding caused by traumatic injury requires quick resolution to prevent exsanguination, and PolySTAT shows great promise as a fast-acting systemic hemostat to enhance clotting in bleeding patients. However, the hemostatic mechanism of PolySTAT is dependent on fibrin formation. If thrombin activation or activity is inhibited owing to severe depletion of coagulation factors or use of anticoagulant drugs (e.g. warfarin), fibrin will be unavailable for PolySTAT crosslinking. In this case, co-administration of blood products may be the fastest way to restore fibrin formation for PolySTAT crosslinking. Another instance in which PolySTAT efficacy may be reduced is in the presence of high concentrations of fibrin degradation products. Depending on the PolySTAT-fibrin binding site, it is possible that circulating D-dimers in hyperfibrinolytic patients may compete with clots for PolySTAT binding, thus reducing efficacy.

Collectively, we have demonstrated that polymers can be engineered to recover or augment natural processes in clot formation to treat acute bleeding. More specifically, preparation of polymers by RAFT polymerization enables reproducible and scalable material synthesis and, thus, offers production, storage, and safety advantages over current biologic-based treatments for bleeding. Furthermore, polymers are versatile drug delivery platforms and can be engineered to include other (macro)molecules, such as antifibrinolytic drugs or inhibitors of anticoagulant proteins, for added functionality. Although PolySTAT was evaluated in this work for inducing

hemostasis in acquired coagulopathy, it can also potentially be used to treat acute bleeding episodes in congenital clotting disorders such as FXIII deficiency and used in combination with recombinant clotting factor therapies for hemophilia.

2.5 Acknowledgements

We thank E.B. Lim and R.J. Lamm for assistance with animal studies, J.C. Phan and C.S. Ball for their technical expertise with SEM imaging, and P.D. Iglesia for his technical expertise in rheometry. This work was supported by NIH 1R21EB018637, the Institute of Translational Health Sciences (ITHS), the Washington Research Foundation (SHP), grant KL2 TR000421 from the NIH National Center for Advancing Translational Sciences (NJW), and the Bioengineering Cardiovascular Training Grant NIH 2T32EB001650-06A2 (LWC).

2.6 Supplementary Data

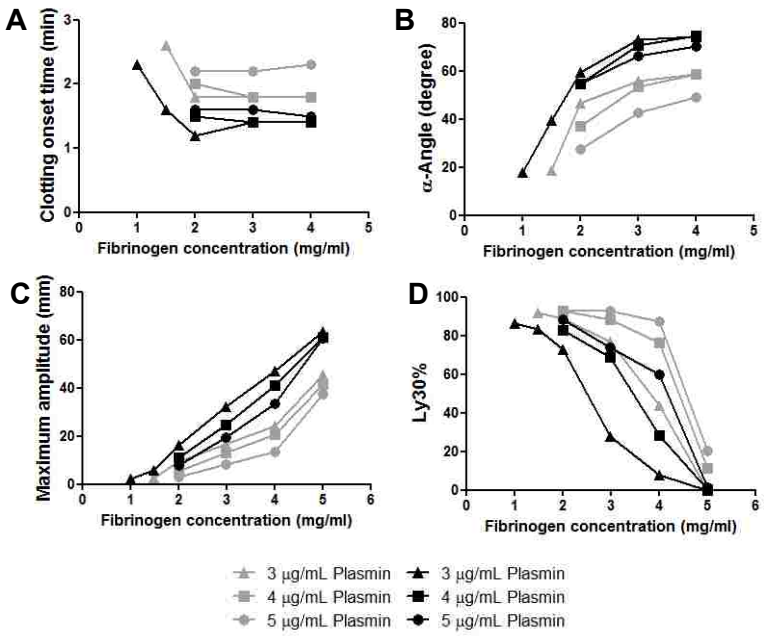

Fig. S2.1. TEG measurements for fibrinogen and plasmin titration study. TEG was used to measure the clotting onset time (**A**), clotting rate (**B**), clot strength (maximum amplitude, MA) (**C**), and percent clot lysis 30 minutes after time to MA (**D**) of purified

fibrin clots formed with solutions containing a range of fibrinogen concentrations (1-5 mg/ml) and plasmin concentrations (3-5 µg/ml plasmin) with 5 µM PolySTAT (black) or PBS (grey). Data are single measurements per fibrinogen and plasmin concentration.

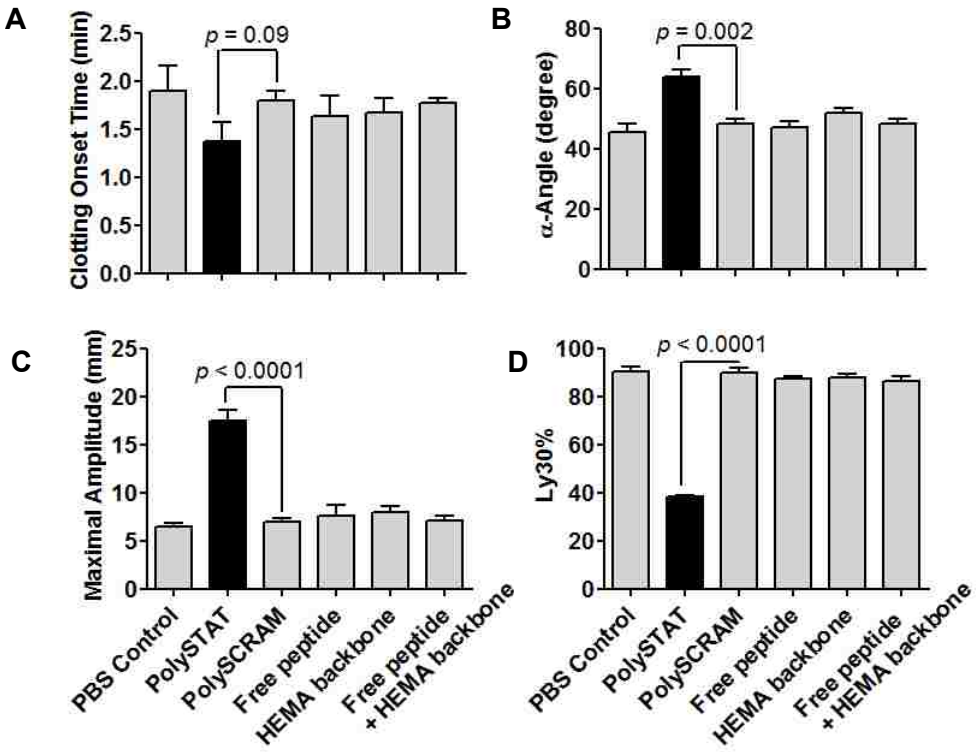

Fig. S2.2. In vitro comparison of PolySTAT to PolySCRAM and component controls. TEG was used to track the formation and breakdown of pure fibrin clots formed from a solution of 1.5 mg/ml fibrinogen, 0.5 IU/ml thrombin, and 2 µg/ml plasmin with 5 µM PolySTAT or controls. Clotting onset time (**A**), clotting rate (**B**), maximum clot strength (**C**), and extent of clot lysis 30 min after time to maximum clot strength (**D**) are shown. Data are averages ± SD (n = 3). Statistical significance was determined using a one-way ANOVA with Tukey post hoc test.

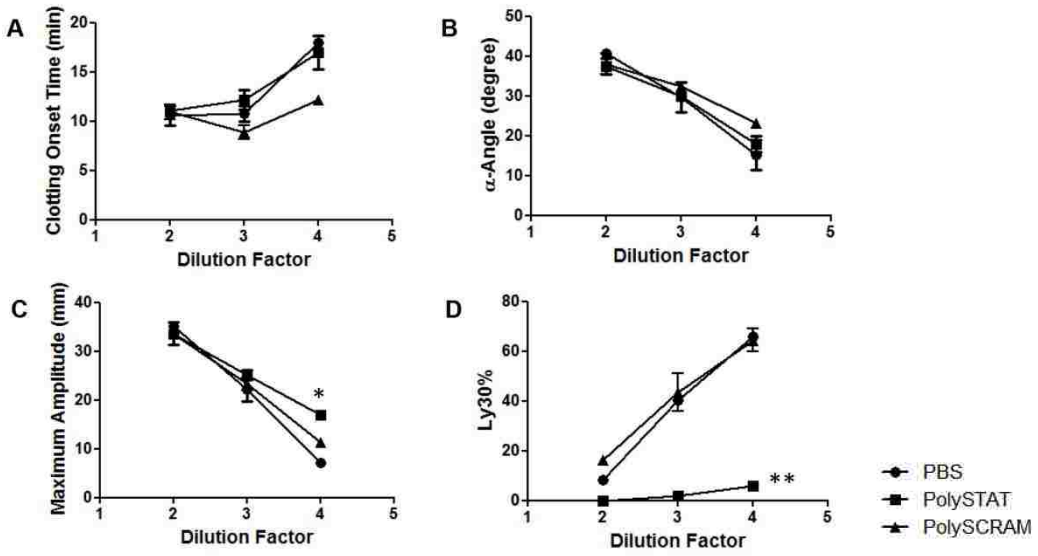

Fig. S2.3. TEG measurements for hemodilutions. TEG was used to measure the clotting onset time (**A**), clotting rate (**B**), clot strength (**C**), and percent clot lysis 30 minutes after time to MA (**D**) of re-calcified diluted whole blood treated with PBS, PolySTAT, or PolySCRAM. Data are averages ± SD (n = 2). Statistical significance was determined using one-way ANOVA with Tukey post hoc test: *$P \leq 0.05$ for comparison between PolySTAT and controls at dilution factor 4, **$P \leq 0.05$ at all dilutions for comparison between PolySTAT and controls.

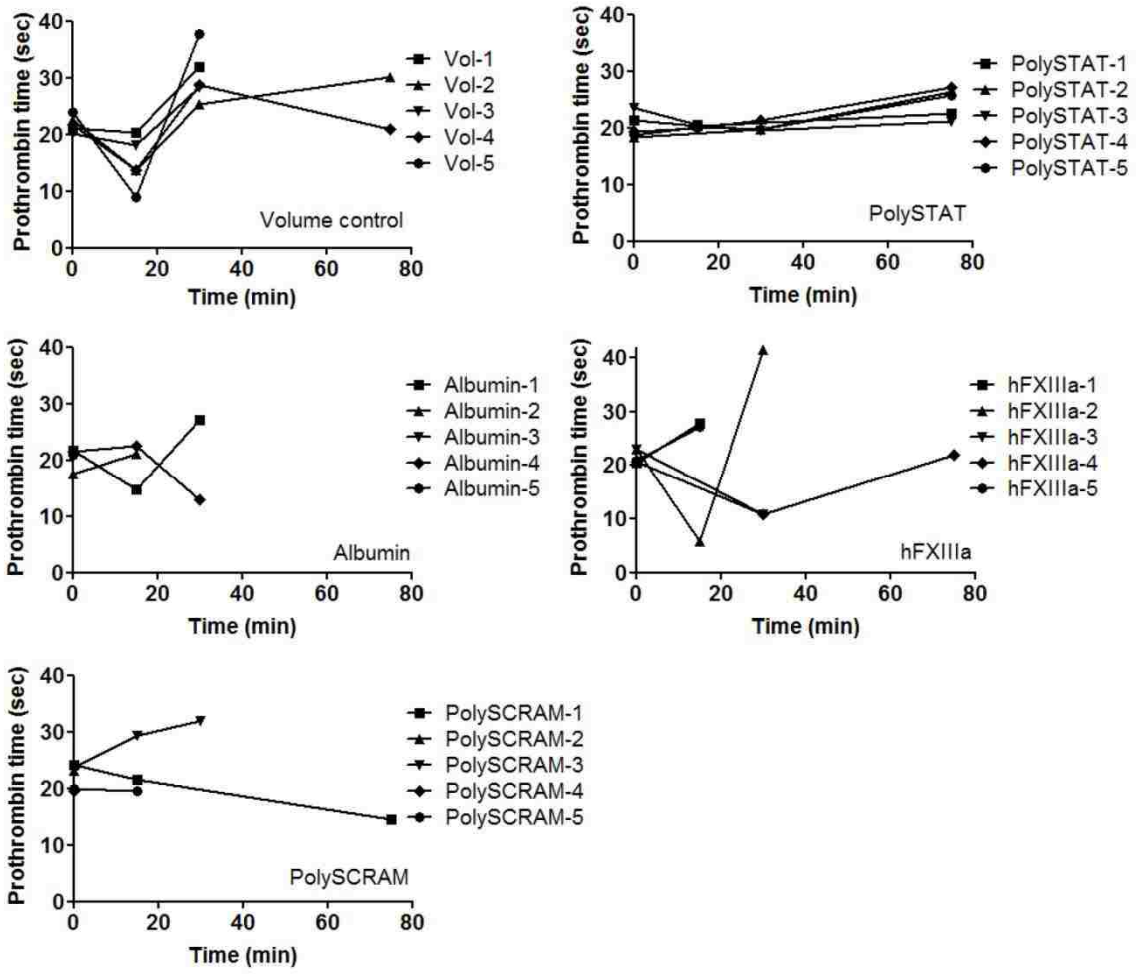

Fig. S2.4. Prothrombin time in rat femoral artery injury models. Prothrombin time was measured at baseline, after free bleeding (15 min), during fluid resuscitation (30 min), and at the end of the protocol (75 min). Controls were volume controls (Vol; 0.9% saline), PolySCRAM, and albumin Data are single measurements per timepoint, per animal (n = 5 per treatment group).

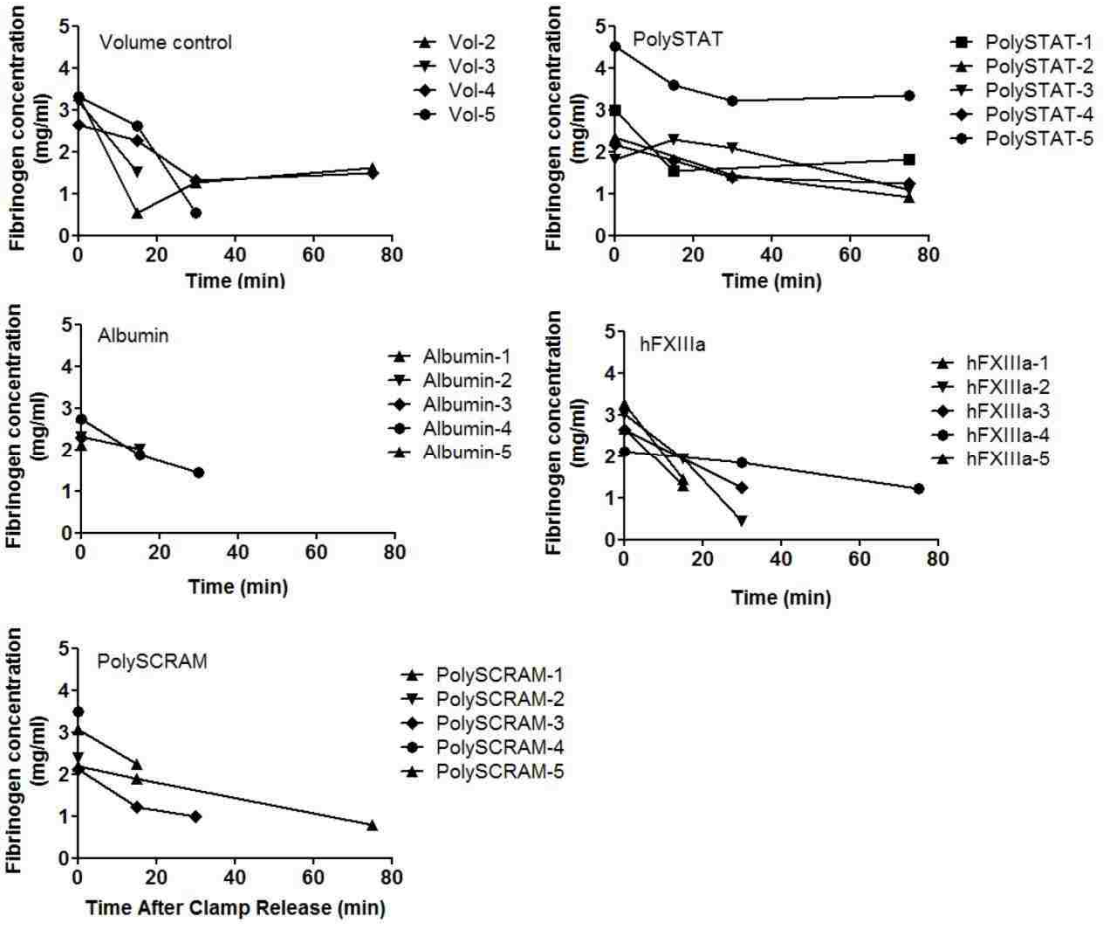

Fig. S2.5. Fibrinogen concentration in rat femoral artery injury models. Fibrinogen concentration was measured at baseline, after free bleeding (15 min), during fluid resuscitation (30 min), and at the end of the protocol (75 min). Data are single measurements per timepoint, per animal (n = 5 per treatment group).

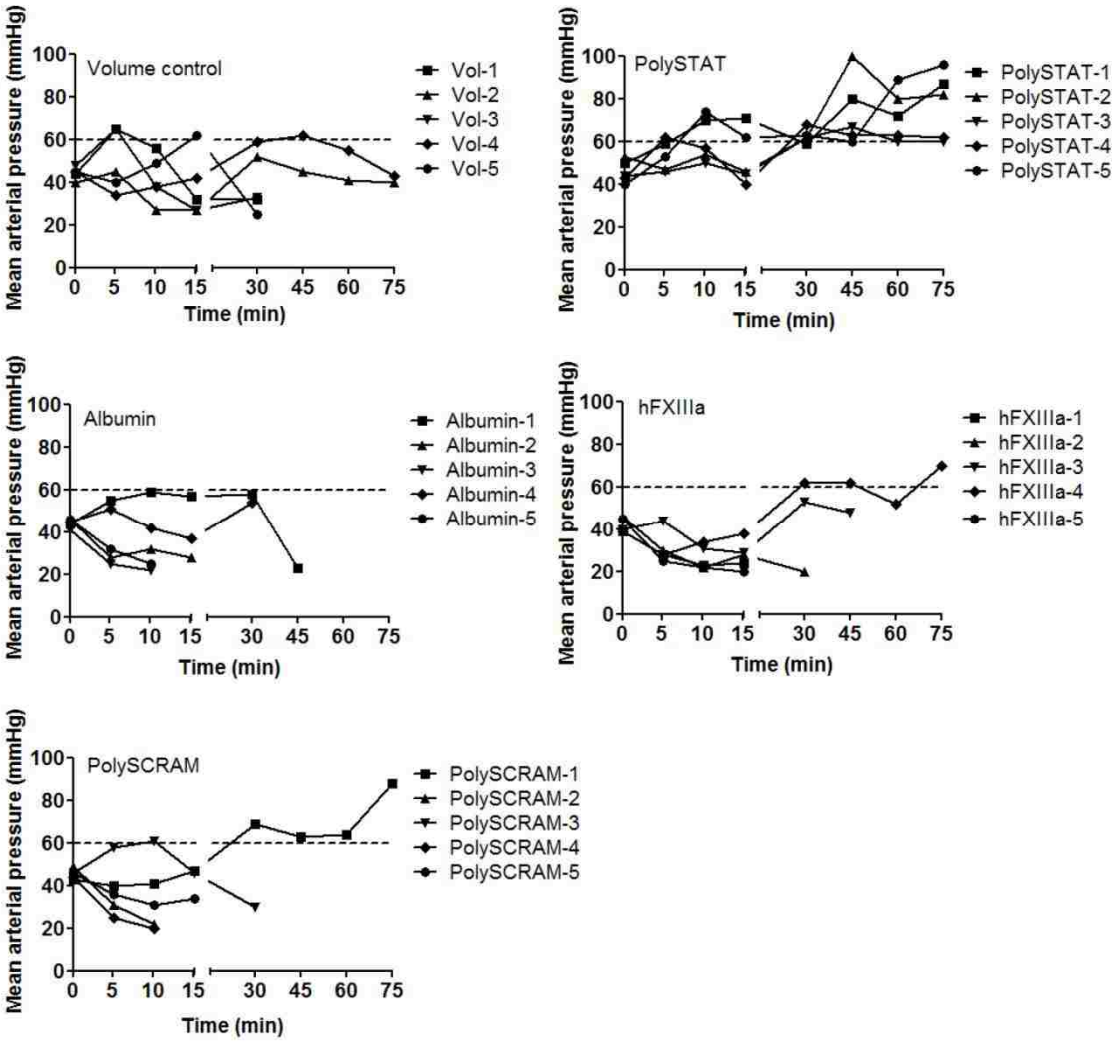

Fig. S2.6. Mean arterial pressure (MAP) in rat femoral artery injury models. MAP was recorded throughout the duration of the protocol time to guide controlled catheter bleeds for initial BP normalization and fluid resuscitation. Saline infusion began at 15 min to raise to and maintain a target BP of 60 mmHg. Data are single measurements per timepoint, per animal (n = 5 per treatment group).

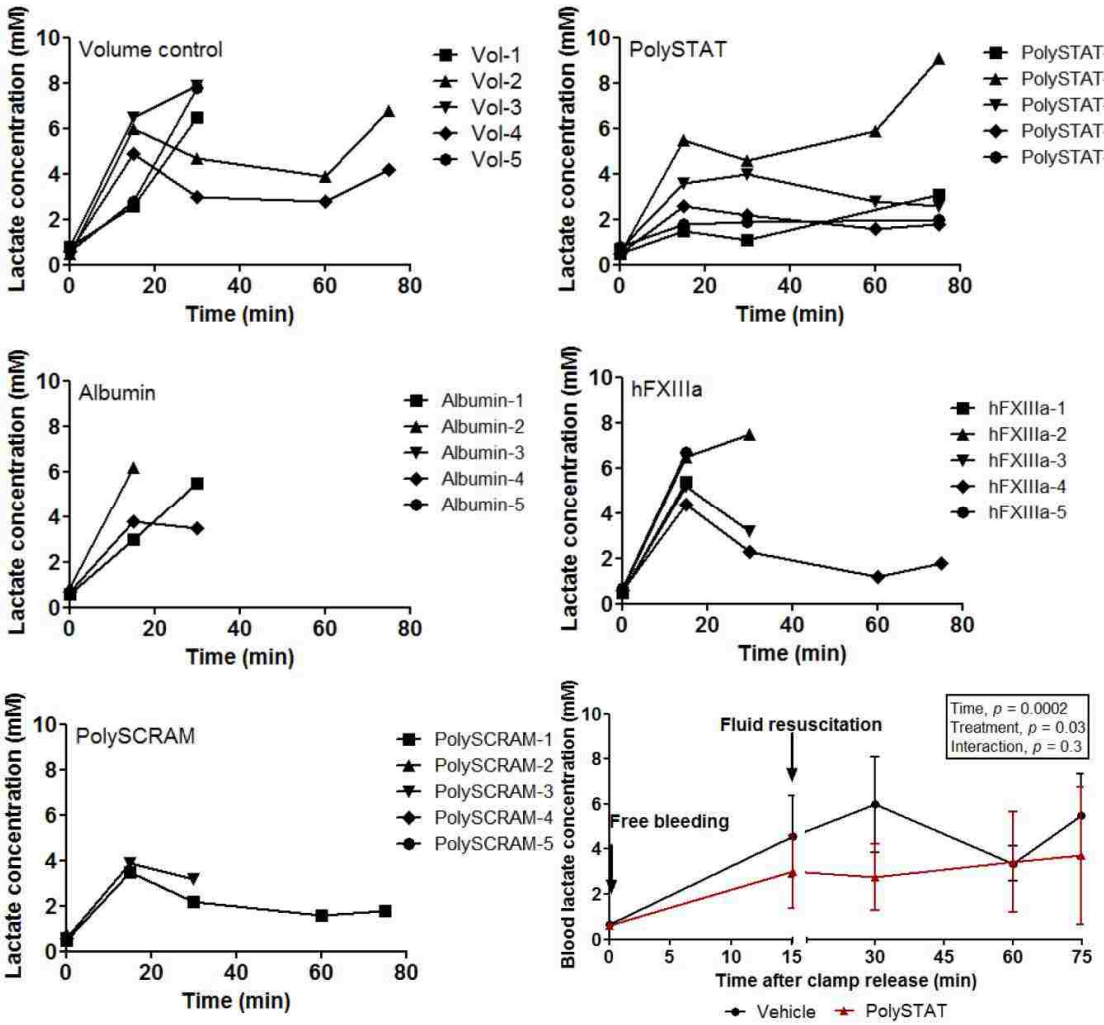

Fig. S2.7. Lactate concentration of rat femoral artery injury models. Lactate concentrations were measured at baseline, after free bleeding (t = 15 min), during fluid resuscitation (t = 30 min, 60 min), and at the end of the protocol time (t = 75 min) to determine the efficacy of fluid resuscitation. Data are single measurements per timepoint, per animal (n = 5 per treatment group) except for the last graph showing averages ± SD of volume controls and PolySTAT. Statistical significance was determined in the last graph using a two-way ANOVA to show the effect of time and treatment on lactate levels.

Table S21. Comprehensive metabolic and hepatic function panel results for 1 h, 1 day, and 1 week after PolySTAT injection in rats. AST, aspartate aminotransferase; ALP, alkaline phosphatase; ALT, alanine transaminase. Direct bilirubin is bilirubin in its conjugated form with glucuronic acid. Subtraction of direct bilirubin from total bilirubin will give the plasma level of unconjugated bilirubin. Higher than normal of either form indicates potential liver toxicity.

Animal	Creatinine (mg/dl)	Albumin (g/dl)	Bilirubin, total (mg/dl)	Bilirubin, direct (mg/dl)	AST (U/l)	ALP (U/l)	ALT (U/l)	Original weight (g)	Weight at timepoint (g)
UNTREATED									
Control-1	0.30	1.2	0.3	<0.1	72	275	40	277	NA
Control-2	0.17	1.1	0.2	<0.1	60	315	39	295	NA
Control-3	0.24	1.4	0.1	<0.1	93	463	46	300	NA
Control-4	0.19	1.4	<0.1	<0.1	48	251	29	306	NA
Control-5	0.17	1.3	…	<0.1	61	181	39	287	NA
AVG	0.21	1.28		<0.1	66.80	297.00	38.60	293.00	
STDEV	0.06	0.13		0.00	16.93	104.80	6.11	11.34	
60 MIN POST-INJECTION									
60min-1	0.37	1.3	0.3	<0.1	84	370	44	308	NA
60min-2	0.38	1.4	0.2	<0.1	74	307	52	300	NA
60min-3	0.37	1.4	0.2	<0.1	115	276	46	303	NA
AVG	0.37	1.37	0.23	<0.1	91.00	317.67	47.33	303.67	
STDEV	0.01	0.06	0.06	0.00	21.38	47.90	4.16	4.04	
1 DAY POST-INJECTION									
1d-1	0.22	1.2	0.3	0.1	194	135	64	304	297
1d-2	0.23	1.2	0.2	<0.1	137	203	49	305	297
1d-3	0.19	1.2	0.4	0.1	236	194	59	292	286
AVG	0.21	1.20	0.30		189.00	177.33	57.33	300.33	293.33
STDEV	0.02	0.00	0.10		49.69	36.94	7.64	7.23	6.35
1 WEEK POST-INJECTION									
1wk-1	0.13	1.4	0.3	0.1	43	307	34	314	398
1wk-2	0.15	1.3	0.3	<0.1	41	225	29	315	375
1wk-3	0.18	1.3	0.4	0.1	44	179	32	313	362
AVG	0.15	1.33	0.33		42.67	237.00	31.67	314.00	378.33
STDEV	0.03	0.06	0.06		1.53	64.84	2.52	1.00	18.23

Table S2.2. Pharmacokinetic constants for PolySTAT. Data were calculated using the method of residuals assuming a two-compartment model.

Pharmacokinetic constant	*Value*
k_{el} (min^{-1})	0.0091
k_{12} (min^{-1})	0.0238
k_{21} (min^{-1})	0.0031
$t_{1/2,\ \alpha}$ (min)	20
$t_{1/2,\ \beta}$ (h)	14.4

Table S2.3. PolySTAT content in urine after tail-vein injection. Data are for 2 rats being treated with PolySTAT for different timepoints: 2d-1 is animal 1 of 3 for the 2-day timepoint and 20min-3 is animal 3 of 3 for the 20 min timepoint. Polymer content in the urine was measured at three different timepoints: 15, 20, and 30 min after injection. *CPM, counts per minute from radiolabeled PolySTAT per 100 µl urine.

Time (min)	Animal	CPM* per 100 µl	Percent of injected dose per 100 µl (%)
0-15	2d-1	36,296	1.95
15-20	2d-1	26,591	1.43
20-30	2d-1	16,586	0.89
5-10	20min-3	35,560	2.05
10-15	20min-3	32,878	1.89
15-20	20min-3	25,714	1.48

Movie S1. Lysis of control fibrin formed with PBS. Time-lapsed confocal imaging of fluorescent fibrin clots treated with PBS buffer and exposed to 10 µg/ml plasmin. Video is accelerated to 100x the actual speed.

Movie S2. Lysis of control fibrin formed with PolySCRAM. Time-lapsed confocal imaging of fluorescent fibrin clots formed with 5 µM PolySCRAM and exposed to 10 µg/ml plasmin. Video is accelerated to 100x the actual speed.

Movie S3. Lysis of PolySTAT-modified fibrin. Time-lapsed confocal imaging of fluorescent PolySTAT-modified fibrin exposed to 10 µg/ml plasmin. Video is accelerated to 100x the actual speed.

Movie S4. Lysis of hFXIIIa-crosslinked fibrin. Time-lapsed confocal imaging of fluorescent fibrin crosslinked with 20 µg/ml hFXIIIa and exposed to 10 µg/ml plasmin. Video is accelerated to 100x the actual speed.

References

1. A. Sauaia, F. A. Moore, E. E. Moore, K. S. Moser, R. Brennan, R. A. Read, P. T. Pons, Epidemiology of trauma deaths: a reassessment, *J Trauma* **38**, 185–193 (1995).
2. R. Davenport, J. Manson, H. De'Ath, S. Platton, A. Coates, S. Allard, D. Hart, R. Pearse, K. J. Pasi, P. MacCallum, S. Stanworth, K. Brohi, Functional definition and characterization of acute traumatic coagulopathy, *Crit Care Med* **39**, 2652–2658 (2011).
3. K. Brohi, J. Singh, M. Heron, T. Coats, Acute traumatic coagulopathy, *J Trauma* **54**, 1127–1130 (2003).
4. I. Raza, R. Davenport, C. Rourke, S. Platton, J. Manson, C. Spoors, S. Khan, H. D. De'Ath, S. Allard, D. P. Hart, K. J. Pasi, B. J. Hunt, S. Stanworth, P. K. MacCallum, K. Brohi, The incidence and magnitude of fibrinolytic activation in trauma patients, *J Thromb Haemost* **11**, 307–314 (2013).
5. H. E. Achneck, B. Sileshi, R. M. Jamiolkowski, D. M. Albala, M. L. Shapiro, J. H. Lawson, A comprehensive review of topical hemostatic agents: efficacy and recommendations for use, *Ann Surg* **251**, 217–228 (2010).
6. B. J. Hunt, Bleeding and coagulopathies in critical care, *N Engl J Med* **370**, 847–859 (2014).
7. F. A. Moore, E. E. Moore, A. Sauaia, Blood transfusion. An independent risk factor for postinjury multiple organ failure, *Arch Surg* **132**, 620–625 (1997).
8. J. P. Bertram, C. A. Williams, R. Robinson, S. S. Segal, N. T. Flynn, E. B. Lavik, Intravenous hemostat: nanotechnology to halt bleeding, *Sci Transl Med* **1**, 11ra22 (2009).
9. T. Nishiya, M. Murata, M. Handa, Y. Ikeda, Targeting of liposomes carrying recombinant fragments of platelet membrane glycoprotein Ibalpha to immobilized von Willebrand factor under flow conditions, *Biochem Biophys Res Commun* **270**, 755–760 (2000).
10. C. L. Modery, M. Ravikumar, T. L. Wong, M. J. Dzuricky, N. Durongkaveroj, A. Sen Gupta, Heteromultivalent liposomal nanoconstructs for enhanced targeting and shear-stable binding to active platelets for site-selective vascular drug delivery, *Biomaterials* **32**, 9504–9514 (2011).
11. M. Ravikumar, C. L. Modery, T. L. Wong, M. Dzuricky, A. P. D. Sen Gupta, Mimicking Adhesive Functionalities of Blood Platelets using Ligand-Decorated Liposomes, *Bioconjug Chem* **23**, 1266–1275 (2012).
12. Y. Okamura, S. Takeoka, K. Eto, I. Maekawa, T. Fujie, H. Maruyama, Y. Ikeda, M. Handa, Development of fibrinogen gamma-chain peptide-coated, adenosine diphosphate-encapsulated liposomes as a synthetic platelet substitute, *J Thromb Haemost* **7**, 470–477 (2009).

13. S. W. Jones, R. A. Roberts, G. R. Robbins, J. L. Perry, M. P. Kai, K. Chen, T. Bo, M. E. Napier, J. P. Ting, J. M. Desimone, J. E. Bear, Nanoparticle clearance is governed by Th1/Th2 immunity and strain background, *J Clin Invest* **123**, 3061–3073 (2013).
14. I. N. Chernysh, C. Nagaswami, P. K. Purohit, J. W. Weisel, Fibrin clots are equilibrium polymers that can be remodeled without proteolytic digestion, *Sci Rep* **2**, 879 (2012).
15. O. M. Theusinger, W. Baulig, L. M. Asmis, B. Seifert, D. R. Spahn, In vitro factor XIII supplementation increases clot firmness in Rotation Thromboelastometry (ROTEM), *Thromb Haemost* **104**, 385–391 (2010).
16. E. L. Hethershaw, A. L. Cilia La Corte, C. Duval, M. Ali, P. J. Grant, R. A. Ariens, H. Philippou, The effect of blood coagulation factor XIII on fibrin clot structure and fibrinolysis, *J Thromb Haemost* **12**, 197–205 (2014).
17. A. F. Kolodziej, S. A. Nair, P. Graham, T. J. McMurry, R. C. Ladner, C. Wescott, D. J. Sexton, P. Caravan, Fibrin specific peptides derived by phage display: characterization of peptides and conjugates for imaging, *Bioconjug Chem* **23**, 548–556 (2012).
18. A. F. Kolodziej, Z. Zhang, K. Overoye-Chan, V. Jacques, P. Caravan, Peptide optimization and conjugation strategies in the development of molecularly targeted magnetic resonance imaging contrast agents, *Methods Mol Biol* **1088**, 185–211 (2014).
19. G. D. Barrett, I. J. Constable, A. D. Stewart, Clinical results of hydrogel lens implantation, *J Cataract Refract Surg* **12**, 623–631 (1986).
20. R. Duncan, The dawning era of polymer therapeutics, *Nat Rev Drug Discov* **2**, 347–360 (2003).
21. M. Mammen, S.-K. Choi, G. M. Whitesides, Polyvalent Interactions in Biological Systems: Implications for Design and Use of Multivalent Ligands and Inhibitors, *Angew. Chemie* **37** (1998).
22. M. E. Carr Jr., J. Hermans, Size and density of fibrin fibers from turbidity, *Macromolecules* **11**, 46–50 (1978).
23. J. S. Hagemo, J. J. Jorgensen, S. R. Ostrowski, A. Holtan, Y. Gundersen, P. I. Johansson, P. A. Naess, C. Gaarder, Changes in fibrinogen availability and utilization in an animal model of traumatic coagulopathy, *Scand J Trauma Resusc Emerg Med* **21**, 56.
24. D. Fries, W. Z. Martini, Role of fibrinogen in trauma-induced coagulopathy, *Br J Anaesth* **105**, 116–121 (2010).
25. G. F. Grannis, Plasma fibrinogen: determination, normal values, physiopathologic shifts, and fluctuations, *Clin Chem* **16**, 486–494 (1970).
26. S. Finfer, R. Bellomo, N. Boyce, J. French, J. Myburgh, R. Norton, A comparison of albumin and saline for fluid resuscitation in the intensive care unit, *N Engl J Med* **350**, 2247–2256 (2004).

27. D. N. Darlington, T. Craig, M. D. Gonzales, M. G. Schwacha, A. P. Cap, M. A. Dubick, Acute coagulopathy of trauma in the rat, *Shock* **39**, 440–446 (2013).
28. S. R. Odom, M. D. Howell, G. S. Silva, V. M. Nielsen, A. Gupta, N. I. Shapiro, D. Talmor, Lactate clearance as a predictor of mortality in trauma patients, *J Trauma Acute Care Surg* **74**, 999–1004 (2013).
29. T. Yamaoka, Y. Tabata, Y. Ikada, Distribution and tissue uptake of poly(ethylene glycol) with different molecular weights after intravenous administration to mice, *J Pharm Sci* **83**, 601–606 (1994).
30. J. W. Weisel, R. I. Litvinov, Mechanisms of fibrin polymerization and clinical implications, *Blood* **121**, 1712–1719 (2013).
31. K. Overoye-Chan, S. Koerner, R. J. Looby, A. F. Kolodziej, S. G. Zech, Q. Deng, J. M. Chasse, T. J. McMurry, P. Caravan, EP-2104R: a fibrin-specific gadolinium-Based MRI contrast agent for detection of thrombus, *J Am Chem Soc* **130**, 6025–6039 (2008).
32. J. Vymazal, E. Spuentrup, G. Cardenas-Molina, A. J. Wiethoff, M. G. Hartmann, P. Caravan, E. C. Parsons Jr., Thrombus imaging with fibrin-specific gadolinium-based MR contrast agent EP-2104R: results of a phase II clinical study of feasibility, *Invest Radiol* **44**, 697–704 (2009).
33. H. Schöchl, C. J. Schlimp, Trauma bleeding management: the concept of goal-directed primary care., *Anesth. Analg.* **119**, 1064–73 (2014).
34. M. A. Schreiber, Coagulopathy in the trauma patient, *Curr Opin Crit Care* **11**, 590–597 (2005).
35. M. A. Dobrovolskaia, P. Aggarwal, J. B. Hall, S. E. McNeil, Preclinical studies to understand nanoparticle interaction with the immune system and its potential effects on nanoparticle biodistribution, *Mol Pharm* **5**, 487–495 (2008).
36. M. Swaroop, D. C. Straus, O. Agubuzu, T. J. Esposito, C. R. Schermer, M. L. Crandall, Pre-hospital transport times and survival for Hypotensive patients with penetrating thoracic trauma, *J Emerg Trauma Shock* **6**, 16–20 (2013).
37. K. Brohi, M. J. Cohen, R. A. Davenport, Acute coagulopathy of trauma: mechanism, identification and effect, *Curr Opin Crit Care* **13**, 680–685 (2007).
38. M. J. Yanjarappa, K. V Gujraty, A. Joshi, A. Saraph, R. S. Kane, Synthesis of copolymers containing an active ester of methacrylic acid by RAFT: controlled molecular weight scaffolds for biofunctionalization, *Biomacromolecules* **7**, 1665–1670 (2006).

Chapter 3

FUNCTIONAL COMPARISON OF FIBRIN CROSS-LINKING POLYMERS TO CLOTTING FACTORS AND ANTIFIBRINOLYTICS USED IN TRAUMA

Leslie W. Chan, Suzie H. Pun, Nathan J. White

Abstract

Clotting factors, including recombinant factor VIIa (rFVIIa) and fibrinogen, and the antifibrinolytic drug, tranexamic acid (TXA), are used to treat coagulopathy and enhance hemostasis after severe injury. We recently reported a new synthetic polymer hemostat, PolySTAT, which strengthens blood clots by cross-linking fibrin fibers. Intravenous administration of PolySTAT in animal models of femoral artery injury showed reduced blood loss and significantly greater survival compared to controls. The purpose of the current study is to compare PolySTAT to rFVIIa, TXA, and fibrinogen concentrate to determine the potential clinical relevance of PolySTAT for controlling bleeding after trauma. Rotational thromboelastometry (ROTEM) was used to measure the clotting time, clotting rate, maximum clot firmness (MCF), and fibrinolytic activity of plasma with PolySTAT, rFVIIa, TXA, or fibrinogen added at therapeutic concentrations. Fibrinolysis was induced by tissue plasminogen activator (tPa). PolySTAT was subsequently tested in combination with these agents. rFVIIa shortened clotting time and increased clotting rate in a dose-dependent manner, restoring clotting rates to values observed in the absence of lysis. TXA completely eliminated tPa-induced lysis and restored MCF to values observed in the absence of lysis. Fibrinogen improved clotting kinetics and MCF in a dose-dependent manner, but had limited impact on lysis. In contrast to rFVIIa, TXA, and fibrinogen, PolySTAT improved all ROTEM parameters. In addition, PolySTAT worked synergistically with TXA or fibrinogen to produce even larger improvements in MCF. Given that PolySTAT produces comparable improvements in clotting kinetics and clot stability as currently-used hemostatic agents, PolySTAT should be considered for treatment of coagulopathy after trauma.

This chapter was submitted for publication to *Journal of Thrombosis and Hemostasis*.

3.1 Introduction

Hemorrhage is responsible for ~40% of deaths 24 h after traumatic injury [1]. Formation of stable blood clots is essential to stop bleeding. However, ~25% of admitted trauma patients have trauma-induced coagulopathy (TIC) [2], a condition in which clotting function is impaired due to tissue injury and shock [3], clotting factor depletion [4], and activation of profibrinolytic pathways leading to accelerated clot breakdown, or hyperfibrinolysis [5–8]. A major goal of trauma resuscitation is to restore blood coagulation, which is currently addressed by transfusion of blood products (i.e. platelets; fresh frozen plasma, FFP; cryoprecipitates, factor concentrates).

As more data becomes available through prospective studies and retrospective analysis of clinical practices, guidelines for managing bleeding after traumatic injury continue to be adapted [9–11]. In the past two decades, drugs such as recombinant factor VIIa (rFVIIa; NovoSeven® RT, Novo Nordisk), tranexamic acid (TXA; Cyclokapron®, Pfizer), and fibrinogen concentrate (FgC; Riastap®, CSL Behring) have been investigated for use to resolve bleeding after traumatic injury. These drugs promote quick and stable fibrin formation by accelerating thrombin generation, inhibiting plasmin activity, and restoring fibrinogen levels, respectively.

rFVIIa, currently approved for use in hemophilia A patients with FVIII inhibitors, initiates coagulation through complexation with tissue factor (TF) at sites of tissue injury and is responsible for a thrombin burst at platelet surfaces [12]. Case reports have shown instances in which rFVIIa was able to stop bleeding and correct coagulopathy when all standard measures were exhausted [13–16]. However, two clinical trials showed no improvement in survival despite reduced RBC transfusion requirements [17,18]. Given the evidence, rFVIIa is currently recommended as a last resort [10,11].

In contrast, antifibrinolytic drugs, such as TXA, are recommended for early administration to inhibit hyperfibrinolysis, which is associated with increased mortality rate [7,10]. TXA binds to plasminogen to prevent its

conversion into active plasmin. It is currently approved to treat menorrhagia and for prevention of peri- and post-operative bleeding in patients with established coagulopathies [19]. In 2010, a large multicenter trial (CRASH-2) showed reduced risk of hemorrhage-related mortalites when TXA was administered within 3 h after traumatic injury, thus, establishingTXA as a viable hemostatic agent for use in trauma [20].

After severe blood loss, fibrinogen reaches critically-low levels earlier than other clotting factors, and concentrations <2.29 mg/mL are associated with increased mortality rate [4,21]. Fibrinogen is the fibrin-precursor and promotes platelet aggregation through binding of GPIIb-IIIa integrin receptors and is thus integral to stable clot formation. European guidelines recommend fibrinogen replacement forlevels <1.5-2.0 mg/mL [10] while American guidelines have a lower threshold set at 1.0 mg/mL [11]. Fibrinogen is available in FFP, cryoprecipitate, and FgC. FgC is becoming increasingly common in Europe and has the benefits of easy and quick reconstitution, defined concentrations, and smaller administered volumes compared to FFP [22].

We recently reported the synthesis of PolySTAT, a fibrin cross-linking hemostatic polymer (Fig. 3.1A; ~MW 45 kDa) and demonstrated its efficacy in reducing blood loss in a rat femoral artery injury model [23]. PolySTAT consists of a synthetic linear polymer backbone to which multiple fibrin-binding peptides [24] are grafted. Multivalent display of fibrin-binding domains along the polymer enables a single PolySTAT to non-covalently bind to multiple fibrin monomers during fibrin polymerization to create a stable, cross-linked fibrin network [25]. In the following work, we compare the functional performance of PolySTAT to clinically-used hemostatic agents - rFVIIa, TXA, and FgC - under intermediate hyperfibrinolytic conditions using rotational thromboelastometry (ROTEM) to evaluate its potential clinical relevance for trauma. Furthermore, we study the effects on

coagulation when PolySTAT is added to plasma in combination with the aforementioned drugs.

3.2 Materials and methods

3.2.1 Materials

Frozen plasma and NovoSeven® RT were purchased from the Bloodworks Northwest (Seattle, WA). Tissue factor (TF; BT-pro-312) was purchased from Biotang Inc. Tissue plasminogen activator (tPa; T0831) and TXA (1672745) were purchased from Sigma-Aldrich. Plasminogen-depleted fibrinogen (FIB 1) was purchased from Enzyme Research Laboratories. Fibri-Prest® Automate 2 , Unicalibrator , and Owren-Koller buffer were purchased from Diagnostica Stago. PolySTAT was synthesized as previously described [23].

3.2.2 Fibrinogen quantification

Plasma fibrinogen concentration was measured using a standard Fibri-Prest® Automate 2 assay in a Diagnostica Stago Start 4 hemostasis analyzer.

3.2.3 ROTEM assays

ROTEM was used to measure clotting time (CT), clotting rate (α-angle), maximum clot firmness (MCF), and maximum lysis at t = 1 h (ML).. Plasma was thawed at 37˚C and maintained at room temperature during ROTEM studies. For comparison of PolySTAT to rFVIIa and TXA, 286 µL plasma was mixed with 24 µL activation solution (19 µL 0.2 M $CaCl_2$, 4.5 µL 227 pM TF, 0.48 µL 2.9 µM tPa), and 30 µL solution containing PolySTAT, NovoSeven® RT, or TXA. Final concentrations were 3 pM TF for initiation of clotting and 4 nM tPa for clot lysis. Studies were repeated with diluted plasma (60 v/v % plasma diluted with 0.9% saline) to mimic hemodilution from fluid resuscitation. For comparison of PolySTAT to FgC, 7.8, 16, 23, and 31 µL fibrinogen solution (22 mg/mL) was added to diluted plasma containing 1.5 mg/mL fibrinogen to raise fibrinogen concentration by 0.5, 1.0, 1.5, and 2.0

mg/mL, respectively. Clotting was initiated using the same volume and composition activation solution. To evaluate PolySTAT in combination with current clinically-used hemostatic agents, activation solution and 4.4 μM PolySTAT was added to plasma with 4 nM NovoSeven, 6.4 μM TXA, and 0.5 mg/mL supplemented fibrinogen.

3.2.4 Statistical analysis

Data was analyzed using GraphPad Prism 5. One-way ANOVAs with Tukey post hoc tests were completed to identify significant differences between treatments.

3.3 Results and discussion

3.3.1 Comparison of PolySTAT to rVIIa

The effect of PolySTAT on coagulation was compared to clinically-relevant plasma concentrations of rFVIIa using ROTEM (Fig. 3.1). 10 nM (0.5 μg/mL) and 20 nM (1 μg/mL) rFVIIa represent plasma concentrations in the first hour after intravenous injection of 90 μg/kg rFVIIa [26,27], a dose reversing TIC in specific case studies [13,16]. PolySTAT at concentrations corresponding to polymer to fibrinogen molar ratios of 1:5, 1:2, and 1:0.5 (1.8, 4.4, and 18 μM) and rFVIIa were evaluated under conditions simulating intermediate hyperfibrinolysis, previously defined as complete clot lysis between 30-60 min [7] (Fig. 3.1A, top). Under these conditions, rFVIIa primarily accelerated clotting kinetics while PolySTAT both accelerated clotting kinetics and improved clot stability (Fig. 3.1A, middle and bottom). Increasing rFVIIa concentrations led to progressively shorter clotting times, or time to clot initiation (Fig. 3.1B), and accelerated clotting rate 1.2-1.3-fold in undiluted plasma at 4.0 and 20 nM (Fig. 3.1C). The dotted lines in Fig. 1 represent the average ROTEM measurements for plasma in the absence of dilution and tPa-induced fibrinolysis, serving as non-coagulopathic reference points. Under hyperfibrinolytic conditions, rFVIIa restored clotting times to

non-coagulopathic values in diluted plasma and produced even shorter clotting times in undiluted plasma. PolySTAT shortened average clotting times to a similar degree as 10 nM rFVIIa in diluted plasma. PolySTAT accelerated clotting rates to the same degree as rFVIIa in undiluted plasma, restoring clotting rates to non-coagulopathic values. rFVIIa did not significantly alter maximum clot firmness (MCF)(Fig. 3.1D) and only showed significantly reduced maximum lysis (ML; % of MCF lost after 1 h) at the highest concentration (Fig. 3.1E). In contrast, PolySTAT increased MCF 1.2-1.3-fold and increasingly reduced ML at greater concentration in undiluted plasma while eliminating lysis in diluted plasma. When rFVIIa and PolySTAT were added in combination to plasma, no negating effects were observed (Fig. 3.4) and significant changes to MCF and ML were attributed to PolySTAT alone (Fig. 3.4C-D), suggesting that PolySTAT may be used in combination with rFVIIa to compensate for the minimal effect rFVIIa has on clot stability.

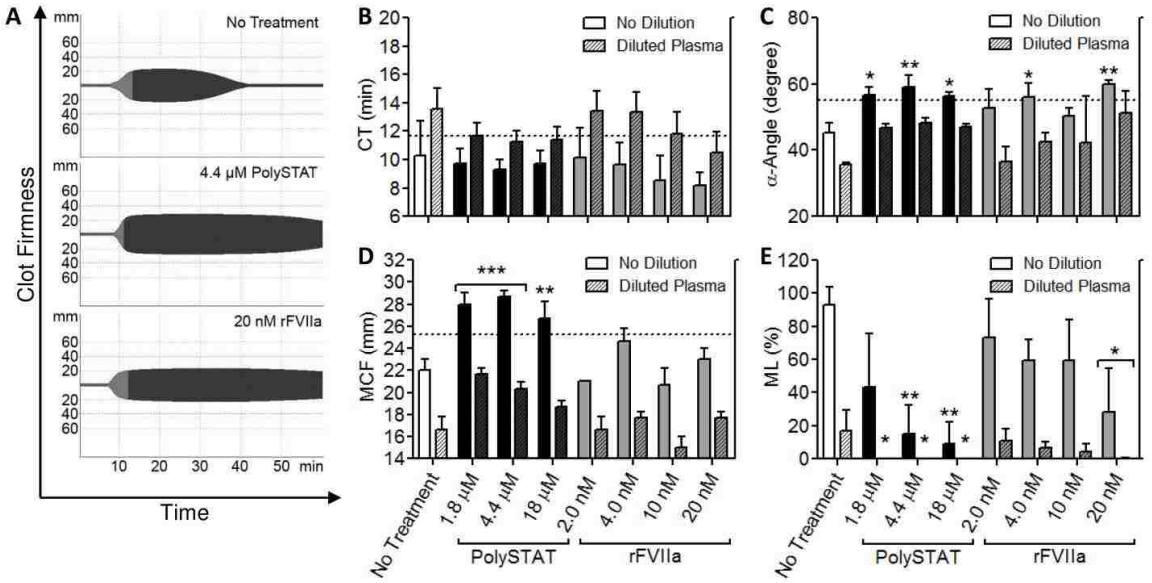

Figure 3.1. Comparison of PolySTAT and rFVIIa in fibrin clots formed with plasma and 40% diluted plasma under hyperfibrinolytic conditions. (A) Representative ROTEM traces from undiluted plasma are shown. (B) Clotting time, (C) α-Angle, (D) MCF, and (E) ML were measured. Data are averages ± SD of experiment completed in triplicate. *P*-values were determined using one-way ANOVA and Tukey post hoc test. **P* < 0.05,

$^{**}P < 0.01$, $^{***}P < 0.001$ versus no treatment. Dotted lines indicate values in the absence of dilution and tPa-induced lysis.

3.3.2 Comparison of PolySTAT to TXA

In a subsequent experiment comparing PolySTAT to TXA, both showed comparable increases in clot firmness and reduction in lysis (Fig. 3.2A). However, unlike PolySTAT, TXA had no effect on clotting time and clotting rate (Fig. 3.2B-C). TXA (6.4 μM and 640 μM) increased MCF 1.2-fold in undiluted plasma(Fig. 2D) and completely eliminated lysis at all concentrations (Fig. 3.2E). TXA is cleared renally, and over the course of an hour after a 1 g injection, the initial dose given in the CRASH-2 clinical trial [20], plasma concentrations drop from 570±35 μM (90±5.4 μg/mL) to 180±3.1 μM (28±0.49 μg/mL) [28]. Our results show that fibrinolytic activity is completely inhibited by 6.4 μM (1 μg/mL) TXA during the 1 h measurement time. Therefore, it is not surprising that plasma concentrations 1-2 orders of magnitude greater would demonstrate hemostatic efficacy in humans. This experiment further demonstrated that inhibiting lysis facilitates stiffer clot formation under hyperfibrinolytic conditions. This is likely due to protective antifibrinolytic effects during the clotting process which gives fibrin more opportunity to polymerize before it is susceptible to cleavage by plasmin. When PolySTAT and TXA were added in combination to plasma, the resulting clots were stiffer than clots formed with either PolySTAT or TXA alone (Fig. 3.4C), suggesting possible drug synergism.

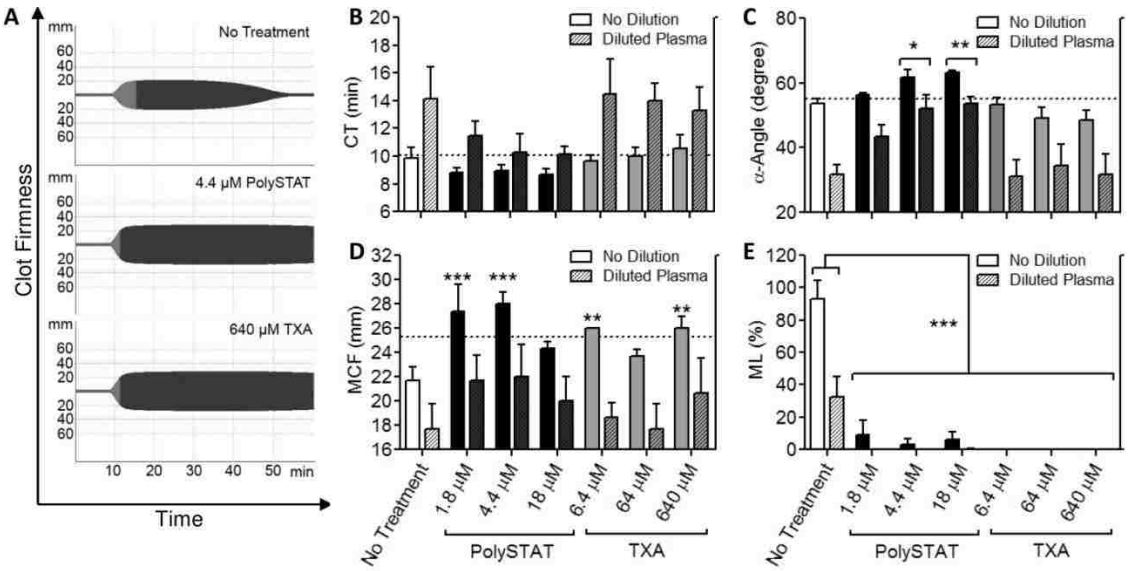

Figure 3.2. Comparison of PolySTAT and TXA in fibrin clots formed with plasma and 40% diluted plasma under hyperfibrinolytic conditions. (A) Representative ROTEM traces from undiluted plasma are shown. (B) Clotting time, (C) α-Angle, (D) MCF, and (E) ML were measured. Data are averages ± SD of experiment completed in triplicate. *P*-values were determined using one-way ANOVA and Tukey post hoc test. **P* < 0.05, ***P* < 0.01, ****P* < 0.001 versus no treatment. Dotted line indicates values in the absence of dilution and tPa-induced lysis.

3.3.3 Comparison of PolySTAT to fibrinogen

In a final comparison, plasma was diluted to lower fibrinogen concentration to 1.5 mg/mL, the threshold at which fibrinogen administration is recommended [10]. Depending on blood loss, every 3 grams of fibrinogen should raise plasma concentrations by ~1 mg/mL in a 70 kg adult patient [29]. Previously, average fibrinogen levels in patients with diffuse bleeding after cardiovascular surgery rose from 1.9 mg/mL to 3.6 mg/mL after a 6.5 g dose of FgC [30]. In the present study, fibrinogen concentration was raised by 0.5, 1.0, 1.5, and 2.0 mg/mL by addition of a concentrated fibrinogen solution to mimic fibrinogen replacement therapy (Fig. 3.3A). Clotting time was reduced by 2.2 min with each additional mg/mL fibrinogen up to an additional 1.5 mg/mL (3.0 mg/mL total), beyond which, no further reduction in clotting time was observed (Fig. 3.3B). Likewise, clotting rate (Fig 3.3C),

MCF (Fig. 3.3D), and ML (Fig. 3.3E) improved in a linear fashion with each additional mg/mL fibrinogen. Plasma with 1.8 and 4.4 μM PolySTAT clotted faster than untreated controls but slower than plasma with 0.5 mg/mL supplemented fibrinogen. The corresponding MCF were comparable to MCF of plasma with 0.5 mg/mL supplemented fibrinogen. Large amounts of supplemented fibrinogen (2.0 mg/mL) was needed to reduce lysis to the same extent as PolySTAT.Overall, PolySTAT performed modestly compared to supplemented fibrinogen. However, when combined with fibrinogen replacement, PolySTAT significantly reduced clotting time while neither PolySTAT alone nor fibrinogen alone had any significant effect (Fig. 3.4A). Furthermore, PolySTAT and fibrinogen significantly improved MCF more so than when PolySTAT was combined with TXA (Fig. 3.4C). Synergism between PolySTAT and supplemented fibrinogen is expected because PolySTAT acts on fibrin which is more abundant at greater fibrinogen concentration.

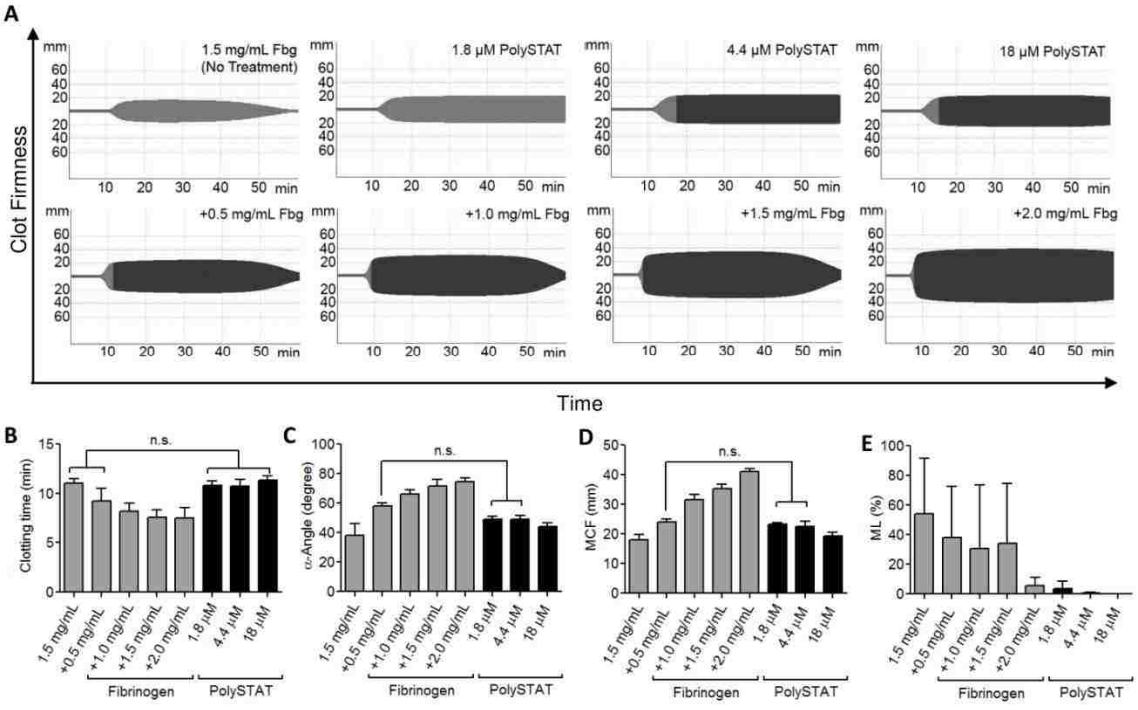

Figure 3.3. Comparison of PolySTAT and fibrinogen replacement. Fibrinogen concentration of diluted plasma containing 1.5 mg/mL fibrinogen was raised by 0.5, 1.0,

1.5, and 2.0 mg/mL for functional comparison to PolySTAT. (A) Representative ROTEM traces are shown. (B) Clotting time, (C) α-Angle, (D) MCF, and (E) ML were measured. Data are averages ± SD of experiment completed in triplicate. *P*-values were determined using one-way ANOVA and Tukey post hoc test. n.s. = no significance.

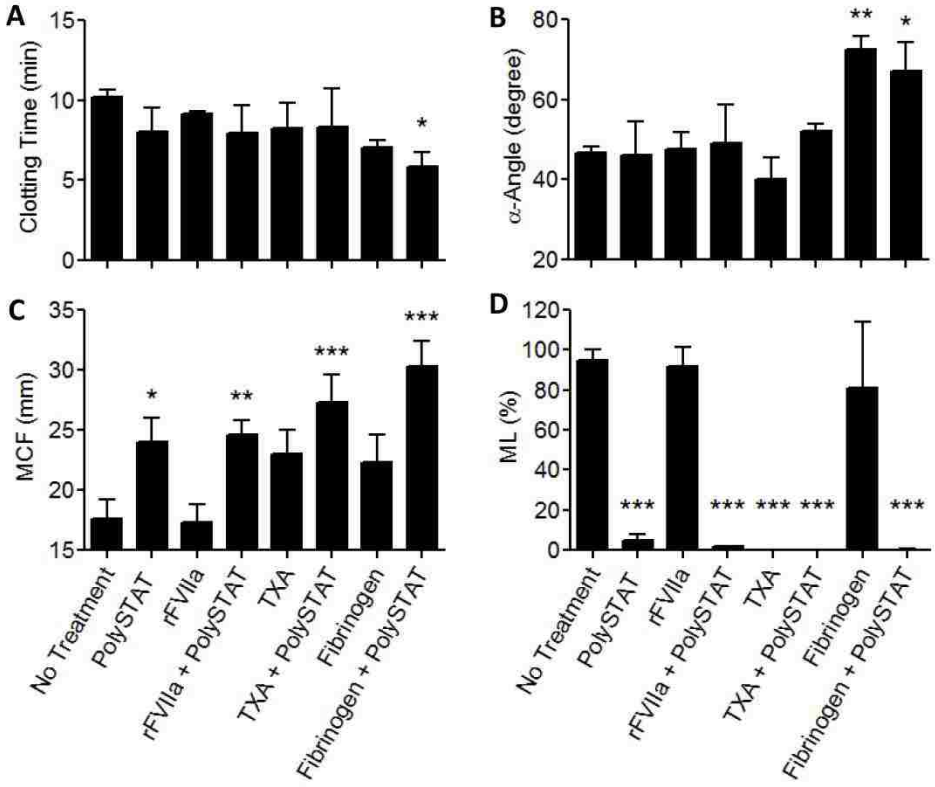

Figure 3.4. Effects of combining PolySTAT with rFVIIa, TXA, and fibrinogen in plasma coagulation under intermediate hyperfibrinolytic conditions. (A) Clotting time, (B) α-angle, (C) MCF, and (D) ML were measured. Data are averages ± SD of experiment completed in triplicate. *P*-values were determined using one-way ANOVA and Tukey post hoc test. **P* < 0.05, ***P* < 0.01, ****P* < 0.001 versus no treatment.

3.4 Conclusions

PolySTAT encompasses the functional properties of both TXA and rFVIIa. Moreover, PolySTAT did not interfere with the activity of rFVIIa, TXA, or fibrinogen and showed even greater improvement of clot strength when given in combination with TXA and fibrinogen. Therefore, PolySTAT may be considered for adjunctive therapy to control bleeding after traumatic injury.

3.5 Acknowledgements

This work was supported by NIH 1R21EB018637, the Washington Research Foundation, grant KL2 TR000421 from the NIH National Center for Advancing Translational Sciences (N.J.W.), and the Bioengineering Cardiovascular Training grant (NIH 2T32EB001650-06A2) (L.W.C.).

References

1 Kauvar DS, Lefering R, Wade CE. Impact of hemorrhage on trauma outcome: an overview of epidemiology, clinical presentations, and therapeutic considerations. *J Trauma* 2006; **60**: S3–11.

2 Brohi K, Singh J, Heron M, Coats T. Acute traumatic coagulopathy. *J Trauma* 2003; **54**: 1127–30.

3 Frith D, Davenport R, Brohi K. Acute traumatic coagulopathy. *Curr Opin Anaesthesiol* 2012; **25**: 229–34.

4 Fries D, Martini WZ. Role of fibrinogen in trauma-induced coagulopathy. *Br J Anaesth* **105**: 116–21.

5 Brohi K, Cohen MJ, Ganter MT, Schultz MJ, Levi M, Mackersie RC, Pittet J-F. Acute coagulopathy of trauma: hypoperfusion induces systemic anticoagulation and hyperfibrinolysis. *J Trauma* 2008; **64**: 1211–7.

6 Raza I, Davenport R, Rourke C, Platton S, Manson J, Spoors C, Khan S, De'Ath HD, Allard S, Hart DP, Pasi KJ, Hunt BJ, Stanworth S, MacCallum PK, Brohi K. The incidence and magnitude of fibrinolytic activation in trauma patients. *J Thromb Haemost* 2013; **11**: 307–14.

7 Schöchl H, Frietsch T, Pavelka M, Jambor C. Hyperfibrinolysis after major trauma: differential diagnosis of lysis patterns and prognostic value of thrombelastometry. *J Trauma* 2009; **67**: 125–31.

8 Schöchl H, Voelckel W, Maegele M, Solomon C. Trauma-associated hyperfibrinolysis. *Hamostaseologie* 2012; **32**: 22–7.

9 Rossaint R, Bouillon B, Cerny V, Coats TJ, Duranteau J, Fernández-Mondéjar E, Hunt BJ, Komadina R, Nardi G, Neugebauer E, Ozier Y, Riddez L, Schultz A, Stahel PF, Vincent J-L, Spahn DR. Management of bleeding following major trauma: an updated European guideline. *Crit Care* 2010; **14**: R52.

10 Spahn DR, Bouillon B, Cerny V, Coats TJ, Duranteau J, Fernandez-Mondejar E, Filipescu D, Hunt BJ, Komadina R, Nardi G, Neugebauer E, Ozier Y, Riddez L, Schultz A, Vincent JL, Rossaint R. Management

of bleeding and coagulopathy following major trauma: an updated European guideline. *Crit Care* 2013; **17**: R76.

11 Nuttall GA, Brost BC, Connis RT, Gessner JS, Harrison CR, Miller RD, Nickinovich DG, Nussmeier NA, Rosenbergy AD, Spense R. Practice Guidelines for Perioperative Blood Transfusion and Adjuvant Therapies. *Anesthesiology* 2006; **105**: 198–208.

12 Monroe DM, Hoffman M, Roberts HR. Platelets and Thrombin Generation. *Arterioscler Thromb Vasc Biol* 2002; **22**: 1381–9.

13 O'Neill PA, Bluth M, Gloster ES, Wali D, Priovolos S, Dimaio TM, Essex DW, Catanese CA, Strauss RA. Successful Use of Recombinant Activated Factor VII for Trauma-Associated Hemorrhage in a Patient without Preexisting Coagulopathy CASE REPORT. *J Trauma Inj Infect Crit Care* 2002; **52**: 400–5.

14 Dutton RP, Parr M, Tortella BJ, Champion HR, Bernard GR, Boffard K, Bouillon B, Croce MA, Dimsits J, Holcomb JB, Leppaniemi A, Vincent JL, Hauser CJ. Recombinant activated factor VII safety in trauma patients: results from the CONTROL trial. *J Trauma* 2011; **71**: 12–9.

15 Martinowitz U, Kenet G, Segal E, Luboshitz J, Lubetsky A, Ingerslev J, Lynn M. Recombinant Activated Factor VII for Adjunctive Hemorrhage Control in Trauma. *J Trauma Inj Infect Crit Care* 2001; **51**: 431–9.

16 Kenet G, Walden R, Eldad a, Martinowitz U. Treatment of traumatic bleeding with recombinant factor VIIa. *Lancet* 1999; **354**: 1879.

17 Boffard KD, Riou B, Warren B, Choong PI, Rizoli S, Rossaint R, Axelsen M, Kluger Y. Recombinant factor VIIa as adjunctive therapy for bleeding control in severely injured trauma patients: two parallel randomized, placebo-controlled, double-blind clinical trials. *J Trauma* 2005; **59**: 8.

18 Hauser CJ, Boffard K, Dutton R, Bernard GR, Croce M a, Holcomb JB, Leppaniemi A, Parr M, Vincent J-L, Tortella BJ, Dimsits J, Bouillon B. Results of the CONTROL trial: efficacy and safety of recombinant activated Factor VII in the management of refractory traumatic hemorrhage. *J Trauma* 2010; **69**: 489–500.

19 Napolitano LM, Cohen MJ, Cotton B a., Schreiber M a., Moore EE. Tranexamic acid in trauma: How should we use it? *J Trauma Acute Care Surg* 2013; **74**: 1575–86.

20 Shakur H, Roberts I, Bautista R, Caballero J, Coats T, Dewan Y, El-Sayed H, Gogichaishvili T, Gupta S, Herrera J, Hunt B, Iribhogbe P, Izurieta M, Khamis H, Komolafe E, Marrero MA, Mejia-Mantilla J, Miranda J, Morales C, Olaomi O, et al. Effects of tranexamic acid on death, vascular occlusive events, and blood transfusion in trauma patients with significant haemorrhage (CRASH-2): a randomised, placebo-controlled trial. *Lancet* 2010; **376**: 23–32.

21 Hagemo JS, Stanworth S, Juffermans NP, Brohi K, Cohen MJ, Johansson PI, Roislien J, Eken T, Naess PA, Gaarder C. Prevalence, predictors and outcome of hypofibrinogenaemia in trauma: a multicentre observational study. *Crit Care* 2014; **18**: R52.

22 Schöchl H, Schlimp CJ, Voelckel W. Potential value of pharmacological protocols in trauma. *Curr Opin Anaesthesiol* 2013; **26**: 221–9.

23 Chan LW, Wang X, Wei H, Pozzo LD, White NJ, Pun SH. A Synthetic Fibrin-Crosslinking Polymer for Modulating Clot Properties and Inducing Hemostasis. *Sci Transl Med* 2015; **7**: 277ra29.

24 Kolodziej AF, Nair SA, Graham P, McMurry TJ, Ladner RC, Wescott C, Sexton DJ, Caravan P. Fibrin specific peptides derived by phage display: characterization of peptides and conjugates for imaging. *Bioconjug Chem* 2012; **23**: 548–56.

25 Chan LW, White NJ, Pun SH. Synthetic Strategies for Engineering Intravenous Hemostats. *Bioconjug Chem* 2015; [Epub ahead of print].

26 Villar A, Aronis S, Morfini M, Santagostino E, Auerswald G, Thomsen HF, Erhardtsen E, Giangrande PLF. Pharmacokinetics of activated recombinant coagulation factor VII (NovoSeven) in children vs. adults with haemophilia A. *Haemophilia* 2004; **10**: 352–9.

27 Klitgaard T, Tabanera y Palacios R, Boffard KD, Iau PTC, Warren B, Rizoli S, Rossaint R, Kluger Y, Riou B. Pharmacokinetics of recombinant activated factor VII in trauma patients with severe bleeding. *Crit care* 2006; **10**: R104.

28 Eriksson O, Kjellman H, Pilbrant A, Schannong M. Pharmacokinetics of Tranexamic Acid after Intravenous Administration to Normal Volunteers. *Eur J Clin Pharmacol* 1974; **7**: 375–80.

29 Schlimp CJ, Schochl H. The role of fibrinogen in trauma-induced coagulopathy. *Hamostaseologie* 2014; **34**: 29–39.

30 Solomon C, Pichlmaier U, Schoechl H, Hagl C, Raymondos K, Scheinichen D, Koppert W, Rahe-Meyer N. Recovery of fibrinogen after administration of fibrinogen concentrate to patients with severe bleeding after cardiopulmonary bypass surgery. *Br J Anaesth* 2010; **104**: 555–62.

Chapter 4

POLYSTAT: A SYNTHETIC POLYMER HEMOSTAT FOR USE IN COMBINATION WITH RECOMBINANT FVIIA FOR HEMOPHILIA A

Leslie W. Chan, Meghan Lyle, Nathan J. White, Carol H. Miao, Suzie H. Pun

Abstract

Delayed thrombin generation in Hemophilia A results in unstable clots. Standard treatments include factor replacement therapies with factor VIII (FVIII) and recombinant factor VIIa (rFVIIa) to recover thrombin levels and, more recently, FXIIIa has been investigated for use as a clot-stabilizing adjuvant. Similar to FXIIIa, PolySTAT, a newly-reported hemostatic agent, stabilizes blood clots by cross-linking fibrin. In the following work, we evaluate the effects of PolySTAT in combination with rFVIIa on coagulation in hemophilic blood and mice. Together, PolySTAT and rFVIIa accelerated clotting rate and increased maximum clot firmness in hemophilic plasma significantly more so than rFVIIa alone. Furthermore, clotting was initiated earlier in hemophilic blood when combination treatment was used. Tail-bleeding assays, due to high variability within treatment groups and non-optimal rFVIIa doses, have been inconclusive in determining whether PolySTAT can improve the hemostatic effects of rFVIIa.

4.1 Introduction

In hemophilia A, Factor VIII (FVIII) deficiency prevents the timely activation of thrombin for fibrin formation. Therefore, individuals with hemophilia A generally have delayed clotting onset times, inhibiting their ability to minimize blood loss after injury [1]. Furthermore, clots that form are unstable and spontaneous bleeding is a common occurrence. Currently, factor replacement therapies with plasma-derived or recombinant FVIII (pdFVIII and rFVIII, respectively) are used for prophylaxis or on-demand treatment of bleeding [2]. A complication in approximately 30% of hemophilia A patients undergoing FVIII replacement therapy is the development of inhibitory antibodies against FVIII [3]. FVIII treatment in patients with high inhibitor titers >5 BU/mL blood, where a BU (Bethesda unit) is the quantity of inhibitors that inactivates FVIII activity by 50%, is generally ineffective. Therefore, bypassing agents, such as recombinant FVIIa (rFVIIa; NovoSeven®, Novo Nordisk) or activated prothrombin complex concentrates (aPCC; FEIBA®, Baxter), are used to drive thrombin activation [4].

Thrombin plays multiple roles in forming and stabilizing the fibrin network. In addition to generating fibrin monomers for fibrin polymerization, thrombin is also responsible for activating the fibrin cross-linking transglutaminase, Factor XIII (FXIII), and thrombin activatable fibrinolysis inhibitor (TAFI). Limited activation of FXIII and TAFI in hemophilia results in unstable fibrin networks which are more susceptible to lysis [5,6]. Previous studies have explored the possibility of using FXIIIa as an adjuvant with FVIII or rFVIIa [7–9]. Supraphysiological levels of FXIIIa in combination with low FVIII concentration have been shown to normalize clot stability in FVIII-deficient, platelet-poor plasma [7]. Therefore, FXIIIa, which has a considerably longer half-life than FVIII (9 days [10] versus a median of 11.8 h [11], respectively) could potentially be used to reduce frequency of FVIII dosing by stabilizing clots between FVIII doses, the point at which FVIII concentrations are lowest. Additionally, a previous case report showed that

FXIIIa administration 1 h following rFVIIa dosing was a able to stop bleeding in a patient with refractory hemorrhage [9]. Thus, there are a number of potential therapeutic and financial benefits associated with the use of clot stabilizing adjuvants in hemophilia.

More recently, our group reported a new polymer hemostat, PolySTAT, which stabilizes blood clots via fibrin cross-linking [12,13]. The presence of several fibrin-binding peptides on each PolySTAT molecule enables PolySTAT to bind to multiple fibrin monomers during blood clotting, resulting in a dense fibrin nanostructure with increased mechanical stiffness and reduced susceptibility to enzymatic breakdown. Intravenous administration of PolySTAT in an animal model of femoral artery injury significantly reduced hemorrhage volumes and improved survival rate. Furthermore, prior work demonstrates synergism between PolySTAT and other hemostatic agents (i.e. rFVIIa, tranexamic acid, fibrinogen concentrate) to improve clot strength for treatment of bleeding after traumatic injury (Chapter 3). In the present study, the effects of combination treatment with PolySTAT and rFVIIa will be evaluated in FVIII-inhibited plasma and blood and hemophilic mice.

4.2 Materials and methods

4.2.1. Animals

Hemophilia A (HemA) mice of 129/SV x C57BL/6 mixed background with targeted disruption of exon 16 of the FVIII gene were bred and maintained in a specific pathogen-free facility at the Seattle Children's Research Institute in accordance with the National Institutes of Health (NIH) guidelines for animal care.

4.2.2. Rotational thromboelastometry (ROTEM) analysis

ROTEM analysis was used to determine clotting time (CT), clotting rate (α-angle), and maximum clot firmness (MCF) during clot formation for FVIII-

depleted human plasma and FVIII-inhibited human whole blood. Frozen factor VIII-depleted human plasma (FVIII0CD-50) was purchased from Haematologic Technologies, Inc and thawed at 37˚C before use. Whole blood was collected from human donors at the University of Washington Medical Center with the approval from the University of Washington institutional review board (IRB). Human donors had no history of genetic blood clotting conditions and were not taking anti-coagulation medications. Polyclonal sheep anti-human FVIII antibody (PAHFVIII-S, Haematologic Technologies, Inc) was added to citrated whole blood for a final titer of 10 BU/mL and 100 BU/mL to mimic high titers in hemophilia (> 5 BU/mL) [14]. After antibody addition, the blood was allowed to sit for 1 h before being used in ROTEM studies. For each ROTEM run, an activation solution was added to the cup for final concentrations of 3pM tissue factor (TF;BT-PRO-312, Biotang Inc.), 10 mM $CaCl_2$, and low, medium, or high NovoSeven® RT doses (45, 90, 180, 270 μg/kg or 1.2, 2.5, 3.6 μg/mL; Bloodworks Northwest). PolySTAT, synthesized as previously discussed [12], was added alone and in combination with NovoSeven to plasma and whole blood for a final concentration of 5 μM (250 μg/mL).

4.2.3 Tail-bleeding studies

Correction of bleeding volumes in HemA mice was determined using a modified tail clip assay [15]. Tails of anesthetized HemA mice were submerged for 2 min in a 15-mL conical of warmed 0.9% saline (37˚C). Mice were then administered PBS (volume control), 20 mg/kg PolySTAT, 1 mg/kg NovoSeven® RT with and without 20 mg/kg PolySTAT, and 3 mg/mg NovoSeven® RT at a fixed 225-μL injection volume via the tail vein. 10 min after injection, the distal part of the tail at 2-mm diameter was cut and the tail was placed back into the warmed saline, where it was allowed to bleed without disturbance for 10 min. The tail was then cauterized to stop the bleeding. Blood loss was quantified by lysing the collected blood cells with

ACK buffer, centrifuging the lysed blood, and measuring the hemoglobin content in the supernatant using a Victor spectrophotometer (PerkinElmer) at 560 nm.

4.3 Results and Discussion

4.3.1. ROTEM analysis

Combination treatment with rFVIIa and PolySTAT was first evaluated in FVIII-depleted plasma to determine the effects on fibrin polymerization in the absence of platelets. FVIII depletion resulted in slower thrombin generation as evidenced by prolonged CT, or time to clot initiation (42±3.4 min; Fig. 4.1A) and severely-reduced α-angle, or clotting rate (5.0±0.0˚; Fig 4.2B). For reference, previously-frozen plasma with intact FVIII activity generally has CT ~10 min, α-angle ~55˚, and maximum clot firmness (MCF) ~25 mm (Ch. 3, Fig. 1-2). In the absence of FVIII, rFVIIa accelerated fibrin formation (Fig. 4.1A-B) and slightly improved clot firmness (Fig. 1C) in a dose-dependent manner consistent with prior studies [8,1]. At the highest concentration, rFVIIa reduced CT to 7.0±0.33 min and accelerated clotting rate 5.7-fold. As expected, PolySTAT alone had modest effects, reducing CT to 34±3.3 min (Fig. 4.1A) and doubling clotting rate (Fig. 4.1B). PolySTAT stabilizes blood clots through fibrin cross-linking and is, therefore, less effective when there is limited fibrin generation as observed in hemophilia. When PolySTAT was added in combination with rFVIIa, clotting rates and clot firmness were improved to a significantly greater extent than when plasma was treated with rFVIIa alone. Clots formed 28-60% faster in combination treatment groups and were 1.1-1.5-times firmer, demonstrating that rFVIIa restoration of thrombin generation leads to adequate fibrin formation for PolySTAT activity.

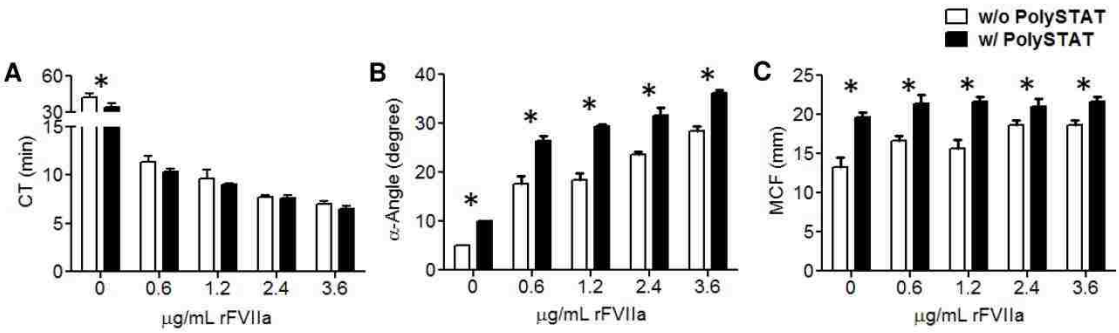

Figure 4.1. ROTEM analysis of FVIII-depleted plasma treated with rFVIIa alone or rFVIIa with PolySTAT. (A) CT , (B) α-angle, and (C) MCF was measured to determine the effect of rFVIIa at four different therapeutic plasma concentrations with and without PolySTAT. **P*<0.05 indicates statistical significance between rFVIIa with and without PolySTAT.

Similarly, neutralization of FVIII activity in whole blood with an inhibitor concentration of 100 BU/mL delayed thrombin activation, thus, extending clotting time (50±2.1 min; Fig. 4.2A) and slowing clotting rate (11±0.0°; Fig. 2B). rFVIIa demonstrated stronger effects on clotting rate (Fig. 4.2B) and MCF (Fig. 4.2C) in whole blood than in plasma (Fig. 4.1B-C), with saturating effects at concentrations as low as 0.6 µg/mL rFVIIa in whole blood. Faster clotting rates can be attributed to the presence of platelets which potentiate rFVIIa activity by providing surfaces for large bursts of thrombin generation [16]. Furthermore, platelets contribute considerably to clot firmness by binding fibrinogen molecules via GPIIbIIIa integrin receptors during platelet aggregation and subsequently contracting [17]. Due to procoagulant effects of platelets, there is diminished opportunity at the current rFVIIa concentration range for substantial PolySTAT-driven improvement of coagulation rate and clot firmness. Clotting time (Fig. 4.2A), however, is one parameter that is improved to a greater extent by combination treatment than rFVIIa alone. Differences caused by addition of PolySTAT were more exaggerated at lower rFVIIa concentration, supporting the conjecture that PolySTAT effects are greatest when there is moderate recovery of thrombin

generation. These results suggest that suboptimal rFVIIa doses can be combined with PolySTAT to normalize blood coagulation.

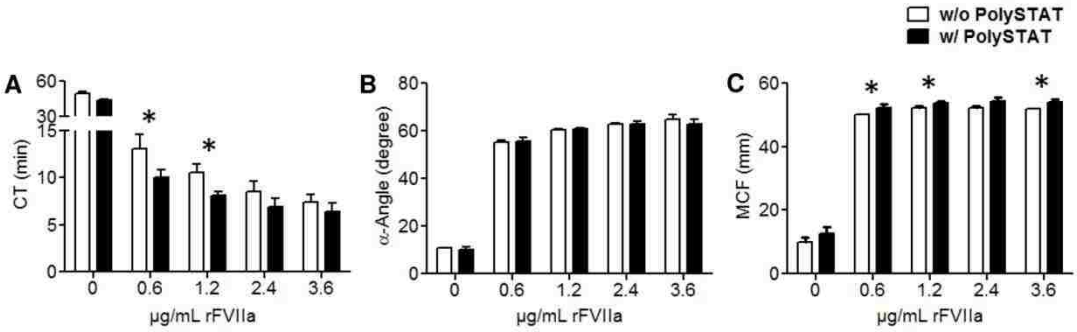

Figure 4.2. ROTEM analysis of whole blood with 100 BU/mL FVIII inhibitors treated with rFVIIa alone or rFVIIa + PolySTAT. (A) CT, (B) α-angle, and (C) MCF was measured to determine the effect of rFVIIa at four different therapeutic plasma concentrations with and without PolySTAT. **P*<0.05 indicates statistical significance between rFVIIa with and without PolySTAT.

Inhibitor concentration was reduced to 10 BU/mL in whole blood to replicate conditions used by Rea et al. to evaluate FXIIIa in combination with rFVIIa for treating severe hemophilia A [8] (Fig. 4.3). FXIIIa is a transglutaminase which cross-links fibrin by forming covalent bonds between lysine and glutamic acid residues and, at supraphysiological concentrations, has been shown to increase clot strength and reduce fibrinolysis [18,19]. Likewise, PolySTAT increases clot strength and stability by cross-linking fibrin. However, it does so by binding multiple fibrin monomers through peptide-protein interactions. Although PolySTAT alters fibrin nanostructure quite differently than FXIIIa [12], incremental improvements in CT (Fig. 4.3A) and MCF (Fig. 4.3C) made by PolySTAT when added in combination with rFVIIa are strikingly similar to improvements seen when FXIIIa is combined with rFVIIa (Fig. 4.3D-E) [8]. Rea et al. discussed the potential use of FXIIIa as an adjuvant to rFVIIa for hemophilia patients responding poorly to standard treatment of rFVIIa alone especially in light of recent evidence suggesting delayed FXIII activation in hemophilia [6]. Given the modest

improvement, however, PolySTAT may be more helpful under conditions in which platelets are depleted or platelet function is compromised.

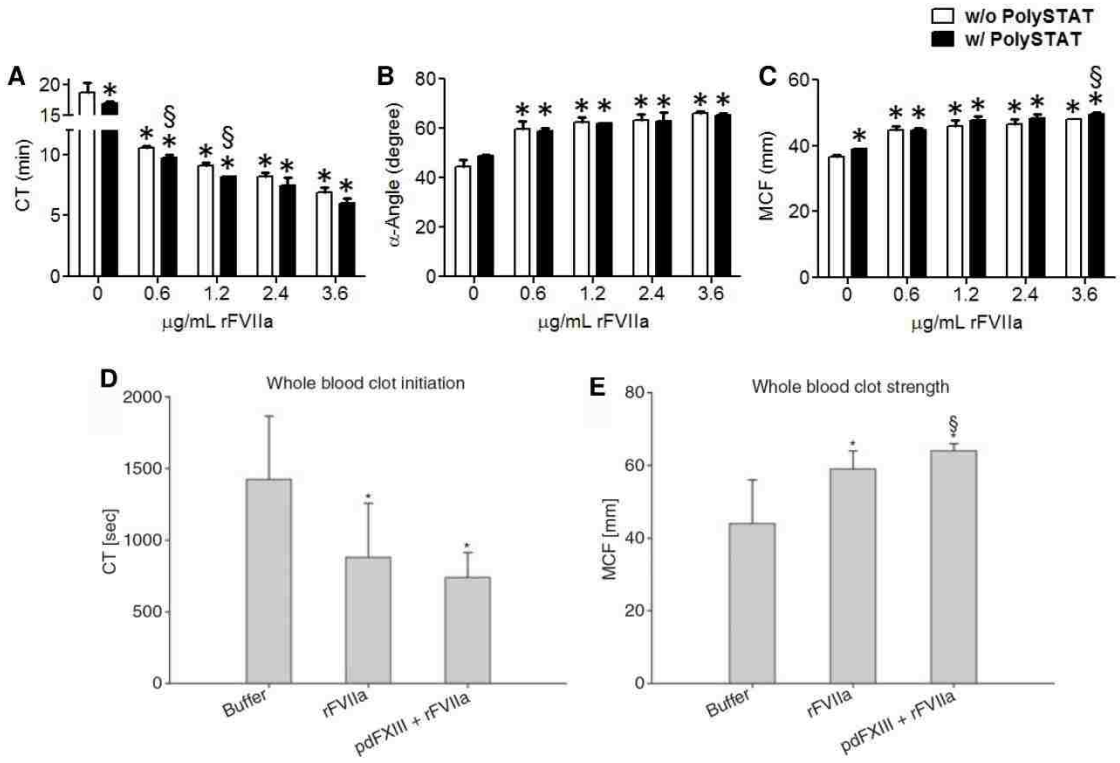

Figure 4.3. ROTEM analysis of whole blood with 10 BU/mL FVIII inhibitors treated with rFVIIa alone or rFVIIa + PolySTAT. (A) CT, (B) α-angle, and (C) MCF was measured to determine the effect of rFVIIa at four different therapeutic plasma concentrations with and without PolySTAT. (D) CT and (E) MCF from a previous study comparing pdFXIIIa + rFVIIa to rFVIIa alone. Final concentrations were 2 µg/mL rFVIIa and 10 µg/mL pdFXIIIa. Reproduced with permission from [8]. (A-C) $^{*}P<0.05$ and $^{\S}P<0.05$ indicates statistical significance versus untreated control and rFVIIa + PolySTAT, respectively. (D-E) $^{*}P<0.05$ and $^{\S}P<0.05$ indicates statistical significance versus buffer control and pdFXIII + rFVIIa, respectively.

4.3.2 Tail-bleeding studies

Tail-bleeding studies were completed to determine if PolySTAT could be combined with suboptimal rFVIIa doses to recover a normal bleeding phenotype. Previously, 3 mg/kg rFVIIa significantly reduced average blood loss in an induced hemophilia mouse model while 1 mg/kg rFVIIa slightly reduced average blood loss (without statistical significance) [20]. In the

present study, 3 mg/kg rFVIIa was used as a positive control for recovery of blood coagulation while 1 mg/kg was used as the suboptimal dose. Human FVIIa association to murine TF is ~3 orders of magnitude weaker than association to human TF [21]. Therefore, rFVIIa doses required to stop bleeding in hemophilic mice are significantly higher compared to the clinical doses recommended for humans [22]. The arms in the study included non-hemophilic controls and HemA mice with the following treatments: (1) volume control (PBS), (2) 20 mg/kg PolySTAT, (3) 1 mg/kg rFVIIa, (4) 1 mg/kg rFVIIa + 20 mg/kg PolySTAT, (5) 3 mg/kg rFVIIa, and (3) 3 mg/kg + 20 mg/kg PolySTAT. 10 min following injection, tails were clipped and submerged in warm saline. Hemoglobin in the collected saline directly correlates to total blood loss (Table 4.1). HemA mice treated with 3 mg/kg rFVIIa had lower average blood loss compared to HemA controls. However, there were no statistically significant reductions in blood loss due to large standard deviations within each group. Furthermore, 1 mg/kg rFVIIa did not reduce average blood loss. For future studies, 3 and 6 mg/kg rFVIIa should be used as the suboptimal dose and positive control, respectively, for increased likelihood of improved bleeding phenotype. Larger number of mice per group should also be considered.

Table 4.1. Hemoglobin content of hemorrhage volume from tail bleed study.

		Hemoglobin (g/dL)		
	n	Average	SD	*p*-value
Normal mice (BALB/c)	3	0.099	0.025	
HemA, volume control	5	0.465	0.292	0.081 vs A*
HemA, 1 mg/kg rFVIIa	5	0.579	0.206	0.266 vs B*
HemA, 3 mg/kg rFVIIa	5	0.246	0.286	0.496 vs B*
HemA, 20 mg/kg PolySTAT	5	0.693	0.262	0.229 vs B*
HemA, 1 mg/kg rFVIIa + 20 mg/kg PolySTAT	5	0.684	0.249	0.237 vs B*
HemA, 3 mg/kg rFVIIa + 20 mg/kg PolySTAT	5	0.192	0.151	0.101 vs B*

*A indicates normal mice; B, HemA volume control.

4.4 Conclusions

Together, rFVIIa and PolySTAT are able to improve clotting kinetics and clot firmness and, in some instances, more so than rFVIIa alone. Therefore, PolySTAT may be investigated further for adjunctive use in treating bleeding in hemophilia.

4.5 Acknowledgements

This work was supported by the Washington Research Foundation (S.H.P), grant KL2 TR000421 from the NIH National Center for Advancing Translational Sciences (N.J.W.), and the Bioengineering Cardiovascular Training grant (NIH 2T32EB001650-06A2) (L.W.C.).

References

1. Rea CJ, Foley JH, Bevan DH, Sorensen B. An in-vitro assessment of tranexamic acid as an adjunct to rFVIII or rFVIIa treatment in haemophilia A. Ann Hematol 2014; 93: 683–92.
2. Kempton CL, Meeks SL. Review Article Toward optimal therapy for inhibitors in hemophilia. Blood 2014; 124: 3365–73.
3. Wight J, Paisley S. The epidemiology of inhibitors in haemophilia A: a systematic review. Haemophilia 2003; 9: 418–35.
4. Kempton CL, Ii GCW. How we treat a hemophilia A patient with a factor VIII inhibitor. Blood 2009; 113: 11–8.
5. Mosnier LO, Lisman T, Berg HM Van Den, Nieuwenhuis HK, Meijers JCM, Bouma BN. The Defective Down Regulation of Fibrinolysis in Haemophilia A Can Be Restored by Increasing the TAFI Plasma Concentration. Thromb Haemost 2001; 86: 1035–9.
6. Brummel-Ziedins KE, Branda RF, Butenas S, Mann KG. Discordant fibrin formation in hemophilia. J Thromb Haemost 2009; 7: 825–32.
7. Rea CJ, Foley JH, Sorensen B. Factor XIII in the Treatment of Hemophilia A. N Engl J Med 2012; 366: 282–3.
8. Rea CJ, Foley JH, Ingerslev J, Sorensen B. Factor XIII combined with recombinant factor VIIa: a new means of treating severe hemophilia A. J Thromb Haemost 2011; **9**: 510–6.
9. Ng C, Silliman CC, Pearl G, Ascp MLS, Smith W, Sh MTA, Manco-johnson M, Wang M. Treatment of Refractory Hemorrhage with Factor XIII in a Patient with Hemophilia A with Inhibitor. Pediatr Blood Cancer 2013; **60**: 23–5.
10. Visich JE, Zuckerman LA, Butine MD, Gunewardena KA, Wild R, Morton KM, Reynolds TC. Safety and pharmacokinetics of

recombinant factor XIII in healthy volunteers: a randomized, placebo-controlled, double-blind, multi-dose study. Thromb Haemost 2005; **94**: 802–7.
11. Van Dijk K, van der Bom JG, Lenting PJ, Groot PG De, Mauser-bunschoten EP, Roosendaal G, Grobbee DE, van den Berg HM. Factor VIII half-life and clinical phenotype of severe hemophilia A. Haematologica 2005; **90**: 494–8.
12. Chan LW, Wang X, Wei H, Pozzo LD, White NJ, Pun SH. A Synthetic Fibrin-Crosslinking Polymer for Modulating Clot Properties and Inducing Hemostasis. Sci Transl Med 2015; **7**: 277ra29.
13. Chan LW, White NJ, Pun SH. Synthetic Strategies for Engineering Intravenous Hemostats. Bioconjug Chem 2015; : epub.
14. Rea CJ, Foley JH, Okaisabor O, Sørensen B. FXIII: mechanisms of action in the treatment of hemophilia A. J Thromb Haemost 2014; **12**: 159–68.
15. Wang X, Shin SC, Chiang AFJ, Khan I, Pan D, Rawlings DJ, Miao CH. Intraosseous Delivery of Lentiviral Vectors Targeting Factor VIII Expression in Platelets Corrects Murine Hemophilia A. Mol Ther 2015; **23**: 617–26.
16. Monroe DM, Hoffman M, Roberts HR. Platelets and Thrombin Generation. Arterioscler Thromb Vasc Biol 2002; **22**: 1381–9.
17. Khurana S, Matrson JC, Westley S, Neill WWO, Timmis GC, Safian RD, Oak R. Monitoring platelet glycoprotein lib / Ilia-fibrin interaction with tissue factor-activated thromboelastography. J Lab Clin Med 1997; **130**: 401–11.
18. Theusinger OM, Baulig W, Asmis LM, Seifert B, Spahn DR. In vitro factor XIII supplementation increases clot firmness in Rotation Thromboelastometry (ROTEM). Thromb Haemost 2010; **104**: 385–91.
19. Hethershaw EL, Cilia La Corte AL, Duval C, Ali M, Grant PJ, Ariens RA, Philippou H. The effect of blood coagulation factor XIII on fibrin clot structure and fibrinolysis. J Thromb Haemost 2014; **12**: 197–205.
20. Tranholm M, Kristensen K, Kristensen AT, Pyke C, Røjkjaer R, Persson E. Improved hemostasis with superactive analogs of factor VIIa in a mouse model of hemophilia A. Blood 2003; **102**: 3615–20.
21. Petersen LC, Nørby PL, Branner S, Sørensen BB, Elm T, Stennicke HR, Persson E, Bjørn SE. Characterization of recombinant murine factor VIIa and recombinant murine tissue factor: a human-murine species compatibility study. Thromb Res 2005; **116**: 75–85.
22. Holmberg HL, Lauritzen B, Tranholm M, Ezban M. Faster onset of effect and greater efficacy of NN1731 compared with rFVIIa, aPCC and FVIII in tail bleeding in hemophilic mice. J Thromb Haemost 2009; **7**: 1517–22.

Chapter 5

FUTURE DIRECTIONS FOR POLYMER HEMOSTATS (POLYSTATS)

Leslie W. Chan

5.1 Summary of PolySTAT hemostatic effects

PolySTAT has shown promise *in vitro* and *in vivo* for enhancing coagulation after injury. As it is the first generation of polymer hemostats, there are many opportunities to improve and optimize this technology. PolySTAT performance is summarized in **Figure 5.1**.

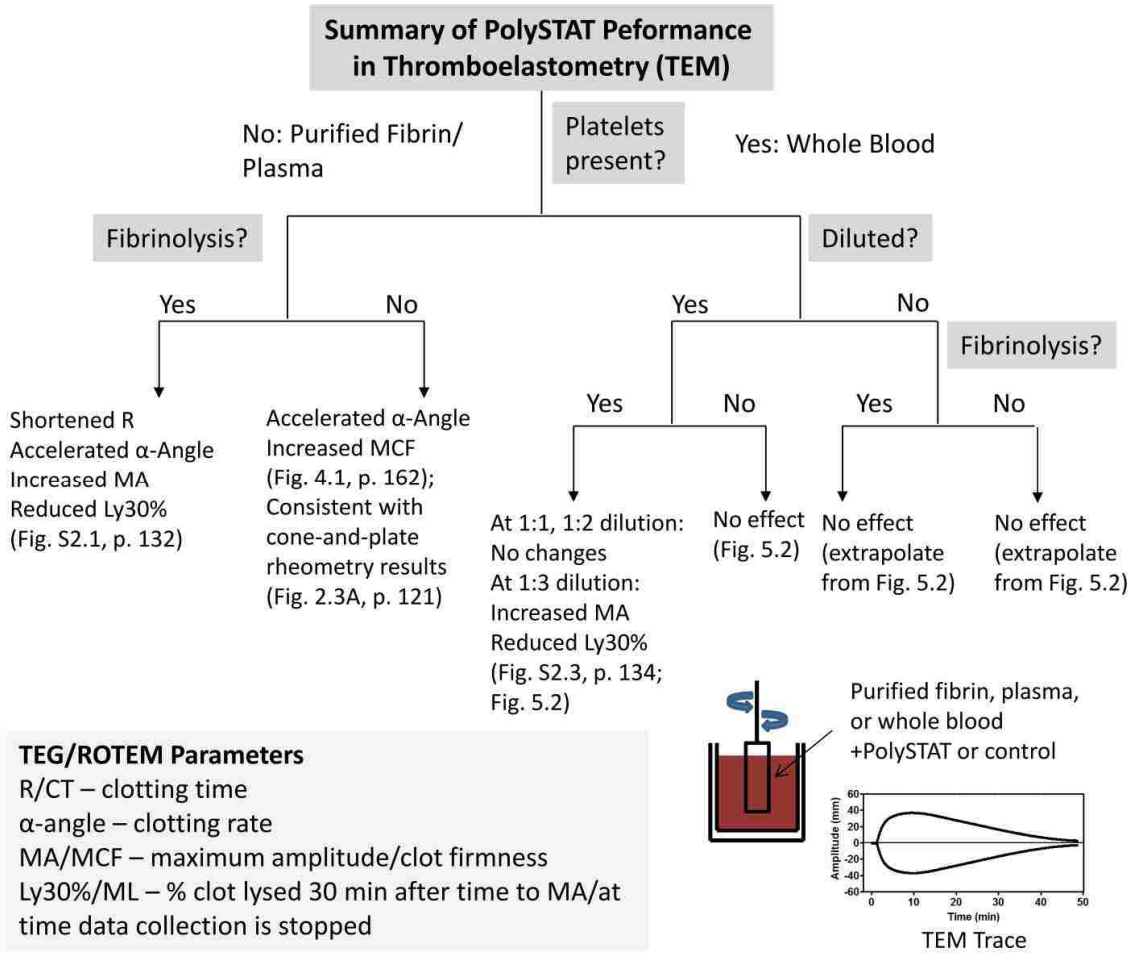

Figure 5.1. Summary of PolySTAT performance under various assay conditions.

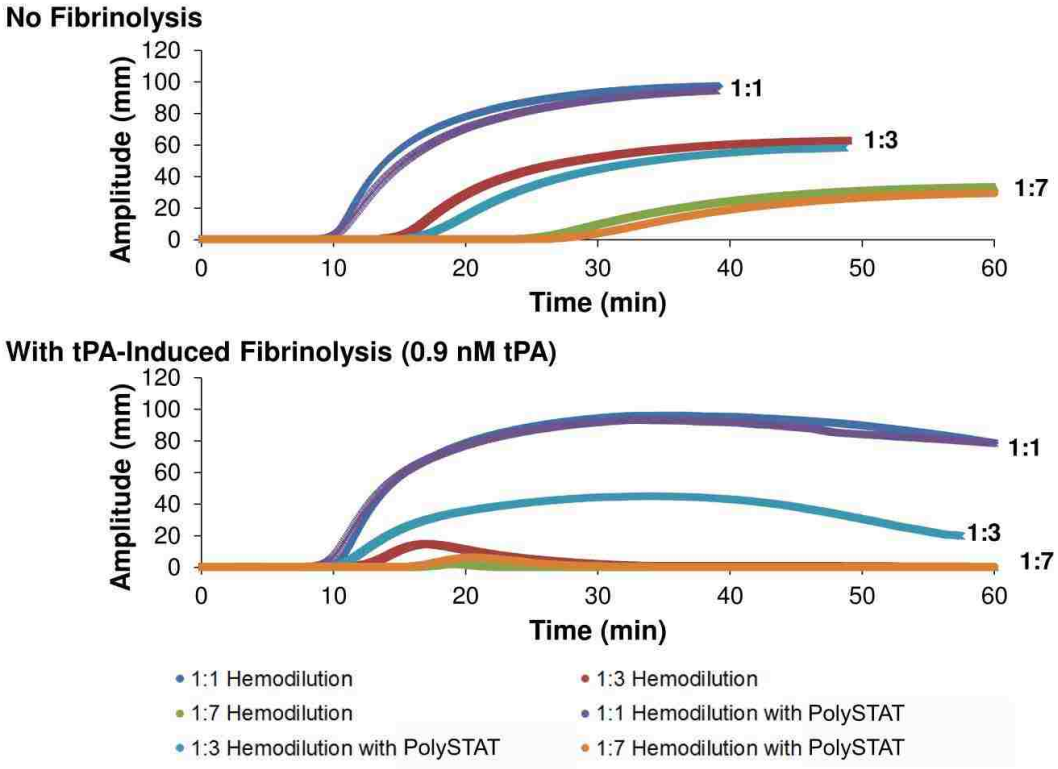

Figure 5.2. PolySTAT performance in diluted blood (hemodilutions) with and without fibrinolytic activity.

Figure 5.1 shows two noticeable trends in PolySTAT effect on coagulation:

1) PolySTAT effects are greater in the absence of platelets (i.e. in pure fibrin and plasma). Platelets contribute considerably to clot strength by providing a membrane surface for a burst of thrombin generation, by aggregating through fibrinogen-facilitated crosslinking, and by subsequent platelet contraction. Previously, activated platelets were shown to enhance clot strength 8-fold compared to platelet-free fibrin clots [1]. Therefore, PolySTAT effects may be masked by the greater clot-strengthening effect of platelets. Furthermore, fibrin monomers may not be as freely accessible to PolySTAT due to fibrinogen binding to platelet surfaces. **Figure 5.2** further supports these conjectures since

TEG traces for hemodilutions with and without PolySTAT diverge with increasing dilution factor under fibrinolytic conditions.

2) PolySTAT is more effective under fibrinolytic conditions. This statement should be explained carefully especially when discussing PolySTAT effect on clot strength. Relative to untreated, lysing controls, PolySTAT-incorporated clots under fibrinolytic conditions have greater clot strength (**Figure 5.2**, bottom, 1:3 and 1:7 hemodilution). However, that clot strength is generally on paar or less than clot strength observed in non-lysing controls (**Figure 5.2**, top). These observations suggest that PolySTAT is *preserving* clot strength rather than *increasing* clot strength and, like tranexamic acid (TXA), is doing so by impeding plasmin breakdown of the fibrin network.

5.2 Engineering PolySTATs with strain stiffening

The trends discussed above present a limitation of PolySTAT which is its modest clot-strengthening abilities under dilutional coagulopathy when clotting factor levels are below normal physiological levels. One possible method to address this limitation is to modify PolySTAT to mimic the structure and mechanical properties of fibrin so that it can act as a fibrin substitute. As previously mentioned, platelet contraction contributes to clot stiffness. Binding of platelets to fibrin causes platelet contractile forces to be exerted onto the fibrin network, and the resulting strain stiffening of fibrin fibers increases the elasticity of the clot [2]. Strain stiffening refers to non-linear elastic behavior in which a material's elastic modulus increases with applied strain [3]. Strain stiffening is found in naturally-occurring biopolymers such as fibrin, collagen, and actin filaments and, in fibrin, is thought to be caused by unfolding of coiled coil connectors and globular nodules in fibrin monomers [4]. Synthetic materials generally deform linearly. However, single α-helices outside the context of coiled coil complexes

possess strain stiffening properties as well [5], and introduction of α-helical (poly)peptides into PolySTAT structure is one possible approach to confer strain stiffening properties into PolySTAT-integrated clots. Polymerization of fibrin monomers end-to-end during clot formation suggests α-helices in series may be optimal [4]. Therefore, α-helical (poly)peptide content as well as configuration are interesting aspects to explore for future generations of PolySTATs with targeted strain stiffening properties. Ring-opening polymerization (ROP) methods have been previously developed to synthesize α-helical cationic polypeptides (up to 40 residues) with increased solubility [6]. Helical polyisocyanopeptide polymers (up to 1100 monomer units) may also be synthesized using nickel(II)-catalysed polymerization of di-, tri- and tetraethylene glycol functionalized isocyano-(D)-alanyl-(L)-alanines [7]. However, temperature triggers polymer bundling and subsequent gelation. Therefore, safety triggers must be put in place to prevent thrombosis after intravenous injection.

Currently, PolySTAT is comprised of a linear, synthetic poly(HEMA) backbone. Preliminary small-angle neutron scattering (SANS) data indicates that poly(HEMA) is a stiff polymer (data not shown). Interestingly, PolySTAT-incorporated fibrin fibers appear stiffer than controls in confocal images (**Figure 2.1C**), thus demonstrating a potential transference of mechanical property from PolySTAT to fibrin fiber and potential for strain stiffening synthetic polymers to generate more elastic fibrin networks.

5.3 Altering hemostatic polymers for intramuscular injection

In addition to modifying polymer mechanics, we may also consider alternative PolySTAT administration routes. Intramuscular (IM) administration is more feasible than intravenous (IV) injection in a prehospital setting, especially on the battlefield where trained medical personnel is not readily accessible. It is unclear whether PolySTAT, as is, is readily absorbed into the bloodstream after IM injection. However, simple

biodistribution studies can be conducted using radiolabeled PolySTAT to verify whether or not first generation PolySTATs are suitable for IM injection. For IM delivery, drugs may be injected into muscle in the arm, thigh, or buttocks. However, absorption of drugs from the arm into the bloodstream is generally quickest due to greater vascularity, one limitation being smaller injection volumes. To stop bleeding after injury, polymers should be released rapidly into the bloodstream instead of forming a sustained-released depot in muscle. Highly water soluble drugs dissolved in an aqueous vehicle is able to rapidly enter the bloodstream through paracellular transport after IM injection [8]. Therefore, PolySTAT may be limited by its solubility (~10 mg/mL) for IM administration. Hydrophobic materials are generally released more slowly into the blood through transcellular transport. Poly(HEMA) and fibrin binding peptides used in PolySTAT are not especially hydrophilic. Therefore, formulating PolySTAT for IM administration may require replacement of the polymer backbone with a more hydrophilic polymer.

Interestingly, acute inflammatory responses after severe traumatic injury lead to increased permeability of the vascular endothelium separating the interstitium from the intravascular space. Increased permeability is attributed to breakdown of the glycocalyx, a 1-3 µm-thick layer of cell-bound proteoglycans, glycosaminoglycan (GAG) side chains, and sialoproteins on the apical side of the endothelium [9]. The glycocalyx maintains the oncotic pressure between the intravascular and interstitial spaces. Therefore, accumulation of fluid in tissues (i.e. edema), is not uncommon during fluid resuscitation. Increased vascular permeability could either facilitate faster IM delivery of hemostatic polymers into the bloodstream or cause polymers to draw water from the intravascular space into the interstitium, resulting in edema. The latter is not ideal and would further reduce circulating volumes (i.e. lower blood pressure). These are additional factors that should be considered when designing IM PolySTAT formulations.

5.4 Assembling hemostatic agents *in vivo* for prophylaxis

In hemophilia A, FVIII is used prophylactically to reduce spontaneous bleeding in joints and blood loss after injury. Perhaps on the more futuristic side, prophylactic hemostatic agents may also one day be administered before high-risk activity on the battlefield. Ideally, these drugs should have long circulation times in the blood and should be inactive in the absence of injury to prevent thrombosis. PolySTAT at 15 mg/kg had a very good safety profile with no evidence of kidney or liver toxicity, cardiopulmonary complications, or death after injection during biodistribution studies. However, PolySTAT was cleared from circulation by 1 h after injection and is, therefore, limited to on-demand treatment of bleeding. Hitchhiking of drugs on albumin, the most abundant protein circulating in plasma, is a common strategy used to prolong drug circulation time [10]. In addition to its abundance, albumin is a highly advantageous drug carrier because it is endogenous to the body (i.e. it is non-toxic and non-immunogenic), it is a very stable protein, and it has a long circulation half-life of 19 days [10]. Instead of using albumin as a drug carrier, in this instance, albumin can be used as part of the hemostatic agent itself. Peptides/proteins that bind activated platelets can be functionalized with lipophilic albumin binding domains [11] and intravenously administered for subsequent assembly on endogenous albumin to create platelet-crosslinking complexes reminiscent of fibrinogen. Fibrin-binding peptides can likewise be used to generate fibrin-crosslinking complexes. Multiple binders would need to assemble on each albumin to facilitate crosslinking. Therefore, identification and use of multiple albumin-targeting groups may be necessary to generate this long-circulating, non-immunogenic hemostatic agent.

In this final chapter, I have proposed three potential directions for future generations of PolySTAT. I wish current and future graduate students/post-docs working on this project the best of luck in furthering this technology.

References

1 Khurana S, Matrson JC, Westley S, Neill WWO, Timmis GC, Safian RD, Oak R. Monitoring platelet glycoprotein lib / Ilia-fibrin interaction with tissue factor-activated thromboelastography. *J Lab Clin Med.* 1997; 130(4): 401–11.

2 Lam WA, Chaudhuri O, Crow A, Webster KD, Li T, Huang J, Fletcher DA. Mechanics and contraction dynamics of single platelets and implications for clot stiffening. *Nat Mater.* 2011; 10(1): 61–6.

3 Erk K a, Henderson KJ, Shull KR. Strain stiffening in synthetic and biopolymer networks. *Biomacromolecules.* 2010; 11(5): 1358–63.

4 Falvo MR, Gorkun O V, Lord ST. The molecular origins of the mechanical properties of fibrin. *Biophys Chem.* 2010; 152(1-3): 15–20.

5 Ackbarow T, Buehler MJ. Superelasticity, energy dissipation and strain hardening of vimentin coiled-coil intermediate filaments: atomistic and continuum studies. *J Mater Sci.* 2007; 42(21): 8771–87.

6 Zhang R, Song Z, Yin L, Zheng N, Tang H, Lu H, Gabrielson NP, Lin Y, Kim K, Cheng J. Ionic α-helical polypeptides toward nonviral gene delivery. *Wiley Interdiscip Rev Nanomed Nanobiotechnol.* 2015; 7(1): 98–110.

7 Kouwer PHJ, Koepf M, Le Sage V a a, Jaspers M, van Buul AM, Eksteen-Akeroyd ZH, Woltinge T, Schwartz E, Kitto HJ, Hoogenboom R, Picken SJ, Nolte RJM, Mendes E, Rowan AE. Responsive biomimetic networks from polyisocyanopeptide hydrogels. *Nature.* 2013; 493(7434): 651–5.

8 Bhalla S. Parenteral Drug Delivery. *Gibaldi's Drug Deliv Syst Pharm Care.* **2007.** p. 103–19.

9 Chelazzi C, Villa G, Mancinelli P, De Gaudio a R, Adembri C. Glycocalyx and sepsis-induced alterations in vascular permeability. *Crit Care.* 2015; 19(1): 26.

10 Dusad A. Albumin as a Delivery Carrier for Rheumatoid Arthritis. *J Nanomed Nanotechnol.* 2013; 04(04).

11 Liu H, Moynihan KD, Zheng Y, Szeto GL, Li A V, Huang B, Egeren DS Van, Park C, Irvine DJ. Structure-based Programming of Lymph Node Targeting in Molecular Vaccines. *Nature.* 2014; 507(7493): 519–22.